（千葉大学審査学位論文）

Formation of Galactic Prominence in the Galactic Central Region

February 2018

Chiba University

Graduate School of Science

Division of Fundamental Sciences

Department of Physics

Chih-Han PENG

ABSTRACT

We conduct resistive magnetohydrodynamic (MHD) simulations to investigate the formation mechanism of the molecular loops observed in the Galactic central region using the NANTEN telescope. Since it is difficult to from molecular loops by lifting up dense molecular gas, we investigate a formation mechanism in which the molecular gas is formed in rising magnetic arcades. This model is based on the in-situ formation model of solar prominences, in which prominences are formed by the cooling instability in the helical magnetic flux ropes created by footpoint motions of a magnetic arch anchored to the solar surface. We extend this model to the Galactic Center by considering the heating/cooling of the interstellar medium along with the rotation of the Galactic disk. The numerical results of our study indicate that magnetic reconnection occurs in a current sheet formed inside the rising magnetic arcade, which creates dense blobs that are confined by the rising helical magnetic flux ropes. Thermal instabilities taking place in the flux ropes form dense filaments that float at 100-200 pc above the Galactic plane. The mass of the filament increases with time, and exceeds 10^5 $M_\odot$. We have additionally conducted three-dimensional simulations and have demonstrated the formation of dense loop-like filaments along which dense matter slides down. The maximum line of sight speed along the loop is in the order of the free-fall speed from the loop top. The position-velocity diagrams that were obtained from these simulations are consistent with those that were derived from the CO observations.

ACKNOWLEDGEMENTS

I am very grateful to Prof. Ryoji Matsumoto for the tender guidance and discussion. I appreciate helpful discussion by Prof. T. Hanawa, Prof. Y. Matsumoto, Prof. H. Hotta and Prof. S. Miyaji. I also would like to express my appreciation to Prof. H. Kurasawa, Prof. T. Suzuki, Prof. T. Yokoyama, Prof. M. Machida, Dr. Y. Asahina and Dr. T. Kaneko for their useful comments. I am thankful to Secretary E. Kawashima and all students of Astrophysical Lab. at Chiba university, especially Dr. Y. Kudoh for lively and academic discussion. Numerical computations were carried out on Cray XC30 at the Center for Computational Astrophysics, National Astronomical Observatory of Japan. I appreciate the scholarship from the Interchange Association, Japan. I also would like to thank my friends of Chiba University Taiwanese Student Association and A Cappella club of Chiba University.

Finally, I appreciate my family. I couldn't have finished my PhD study without their supports.

Contents

Chapter 1

Introduction

1.1 The Galactic Center Region

The Galactic Center (GC) is located approximately 8.5 kpc from the Earth in the direction of the constellation Sagittarius. This region is unique and is more active than the Galactic disk. Figure 1.1 (a) shows a radio map at 330 MHz of a $4^\circ \times 2.5^\circ$ region in the GC, whereas figure 1.1 (b) illustrates the various structures that can be identified in figure 1.1 (a) (Kassim et al. 1999; LaRosa et al. 2000). The most prominent feature is a radio arc, which indicates the presence of a vertical magnetic field threading the disk. A number of thin vertical filaments called "nonthermal threads" are also observed. Circular blobs are the supernova remnants (SNRs). The radio source at the GC that is named Sgr A* is located at the rotational center of the Milky Way Galaxy. Infrared observations of stellar motions near the GC indicates that 3.7×10^6 $M_\odot$ black hole exists (Schödel et al. 2002).

A large amount of molecular gas exists within 300 pc from the GC. This region is called the central molecular zone (CMZ). The total mass of the molecular gas in the CMZ is estimated to be $5{\times}10^7$ $M_\odot$ (Morris & Serabyn 1996). Figure 1.2 shows the far infrared image of the GC region ($R < 125$ pc) inside the CMZ that were obtained using the *Herschel* satellite (Molinari et al. 2011). Rings, loops, and helical filaments can be identified from this figure. These structures and the radio arc indicate that magnetic fields play key roles in the activities and dynamics of the GC region.

The GC region has been surveyed by the NANTEN telescope using the molecular lines of CO. Figure 1.3 (top) depicts a map of the GC region, which was observed by NANTEN (Torii et al. 2010b). The color scale illustrates the integrated intensity distribution of

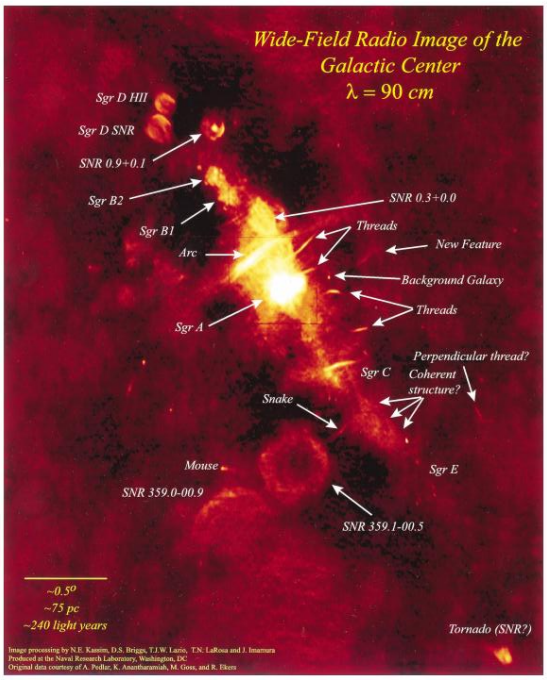

(a)

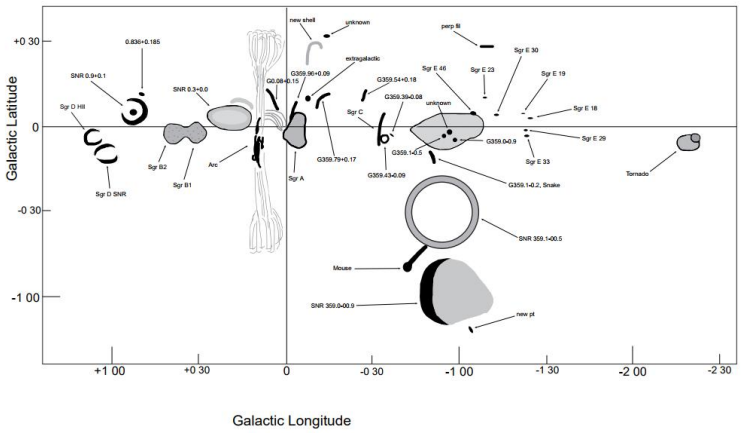

(b)

Figure 1.1: (a) 90-cm radio observation of the Galactic Center. (b) Schematic diagram of (a). (Credit: LaRosa, T. N., Kassim, N. E., Lazio, T. J. W., Hyman, S. D., A Wide-Field 90 Centimeter VLA Image of the Galactic Center Region, AJ, Vol. 119, Issue 1, p. 207-240, 2000 Jan. https://doi.org/10.1086/301168 © AAS. Reproduced with permission. Produced at the U.S. Naval Research Laboratory by Dr. N. E. Kassim and collaborators from data obtained with the National Radio Astronomy's Very Large Array Telescope, a facility of the National Science Foundation operated under cooperative agreement with Associated Universities, Inc. Basic research in radio astronomy at the NRL is supported by the U.S. Office of Naval Research.)

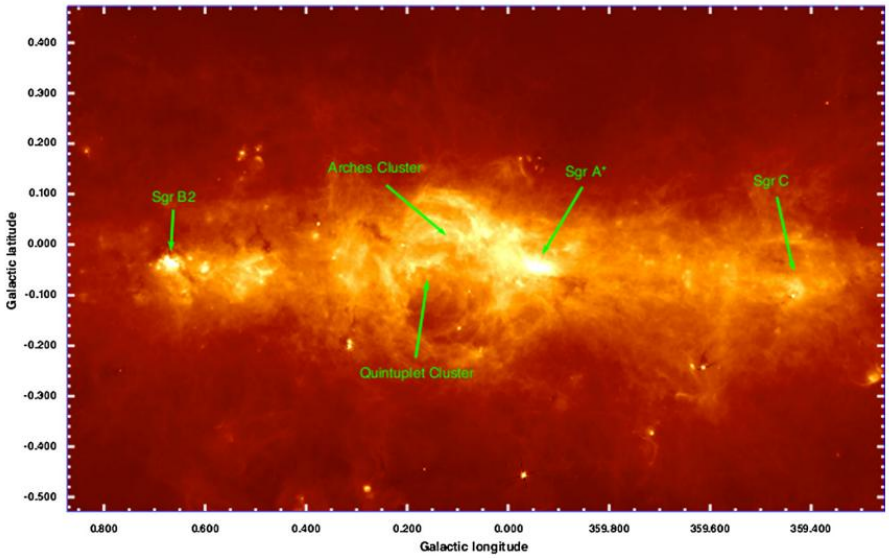

Figure 1.2: Infrared image of the Galactic Center region at 70 μm by the *Herschel* satellite. (Credit: Molonari, S. et al., A 100 pc Elliptical and Twisted Ring of Cold and Dense Molecular Clouds Revealed by Herschel Around the Galactic Center, ApJL, Vol. 735, Issue 2, article id. L33, 7 pp., 2011 Jul 10. https://doi.org/10.1088/2041-8205/735/2/L33 © AAS. Reproduced with permission.)

CO(J=1-0). The most prominent feature is a parallelogram extending from -2° - +3° in position-velocity diagram, which corresponds to the CMZ. The solid boxes in the figure show narrow regions where large velocity dispersions are observed. The dotted regions contain loop-like structures, which will be discussed in the succeeding section.

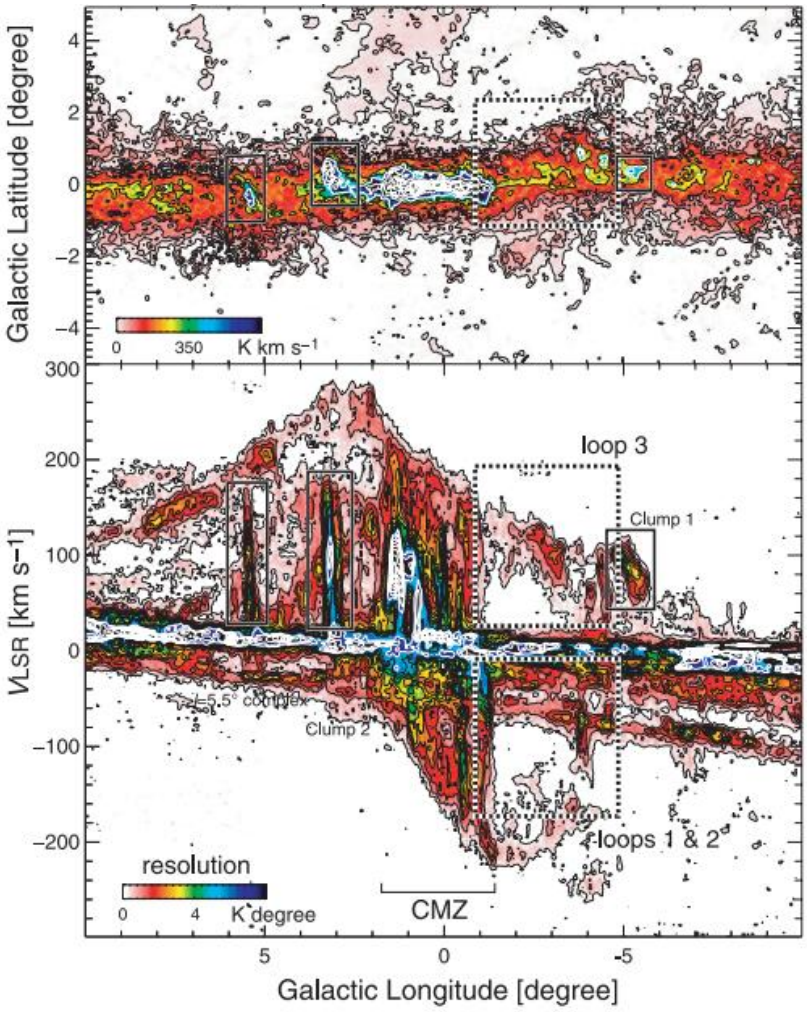

Figure 1.3: (top) Distribution of integrated intensity of CO(J=1-0) obtained by NANTEN radio observations of the GC region. (bottom) Position-velocity diagram. (Credit: Torii, K, et al., A Detailed Observational Study of Molecular Loops 1 and 2 in the Galactic Center, PASJ, 2010, Vol. 62, Issue 5, p. 1307-1332, by permission of Oxford University Press.)

1.2 Molecular Loops

1.2.1 Observations of Molecular Loops

Molecular loops were found around the GC region by CO observations using NANTEN telescope (Fukui et al. 2006; Fujishita et al. 2009). The left-hand panels of figure 1.4 show the distribution of CO intensities integrated over the line of sight velocity -180 km s^{-1} < V_{LSR} < -90 km s^{-1} (top) and -90 km s^{-1} < V_{LSR} < -40 km s^{-1} (middle). The bottom panel illustrates the two molecular loops. The numbers along each loop denote the line of sight velocities. The systematic change in velocity along the loops indicates that the CO gas is falling along the loops. These molecular loops have lengths that range from a few hundred pc to 1 kpc and total masses exceed 10^5 $M_\odot$. The right-hand panel of figure 1.4 illustrates the position-velocity diagram for loops 1 and 2. The molecular loops show large velocity dispersions ($\sim$ 40 km/s) around their footpoints. The line of sight velocity changes with an approximately constant velocity gradient along the loop.

Detailed observations of these molecular loops using NANTEN2 and ASTE (Torii et al. 2010a and Kudo et al. 2011) have revealed that the footpoints of the molecular loops are either U- or L-shaped (or mirrored-L- shapes) in the Galactic latitude-velocity diagram (Figure 1.5) and that temperatures and densities are relatively high around the footpoints. Since there is no radiative heating source in these regions, the authors have proposed that the footpoints of molecular loops are heated by shocks or by magnetic reconnection. Torii et al. (2010b) analyzed the observations of CO, HI, and dust to estimate the total masses of loops 1 and 2; they are 1.6 $\times$ 10^6 $M_\odot$ and 1.9 $\times$ 10^6 $M_\odot$, respectively. The geometrical structures and kinematics of loops 1, 2, and 3 are illustrated in figure 1.6 (Fujishita et al. 2009; Torii et al. 2010b)

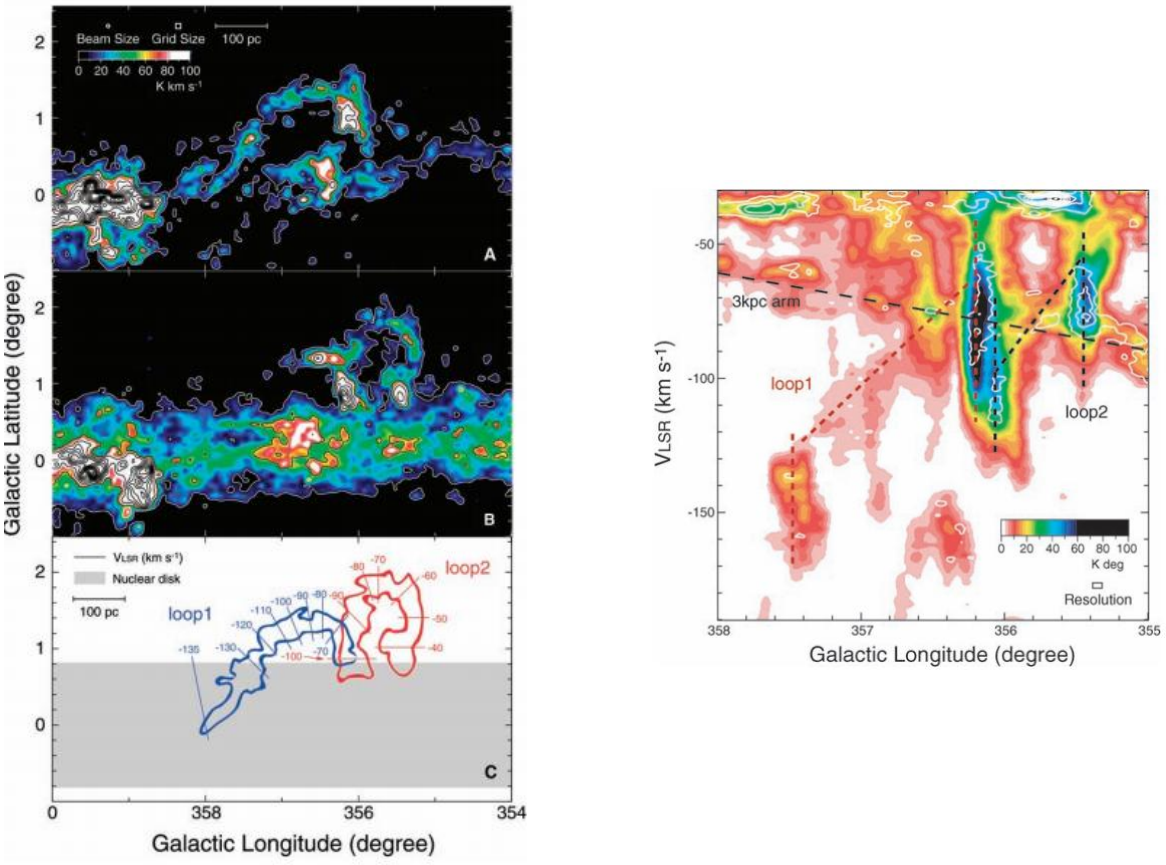

Figure 1.4: (left) Integrated intensity distribution of CO(J=1-0) in the line of sight velocity range (A) -180 to -90 km/s, (B) -90 to -40 km/s and (C) Schematic drawing of loop 1 (blue) and loops 2 (red). Numbers indicate the line of sight velocities along the molecular loops. (right) Galactic longitude-velocity diagram for loops 1 and 2. (Credit: Fukui, Y., et al., Molecular Loops in the Galactic Center: Evidence for Magnetic Flotation, Science, 2006, Vol. 314, Issue 5796, p. 106-109. https://doi.org/10.1126/science.1130425 Reprinted with permission from AAAS.)

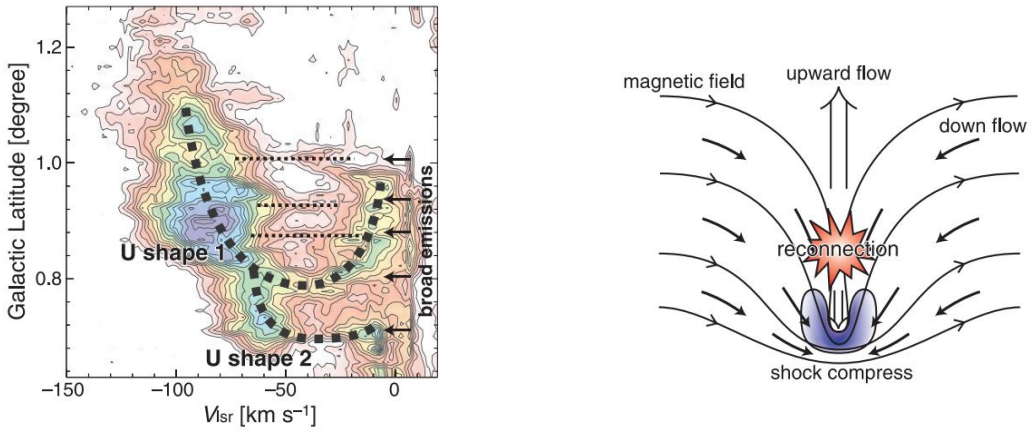

Figure 1.5: (left) Position-velocity diagram around the footpoint of loops 1 and 2. (right) A schematic image of the possible magnetic topology that is expected at a footpoint. Magnetic reconnection can be the origin of the large velocity dispersion. (Credit: Torii, K, et al., Temperature and Density in the Foot Points of the Molecular Loops in the Galactic Center; Analysis of Multi-J Transitions of ^{12}CO (J = 1–0, 3–2, 4–3, 7–6), ^{13}CO (J = 1–0), and C^{18}O (J = 1–0), PASJ, 2010, Vol. 62, Issue 3, p. 675-695, by permission of Oxford University Press.)

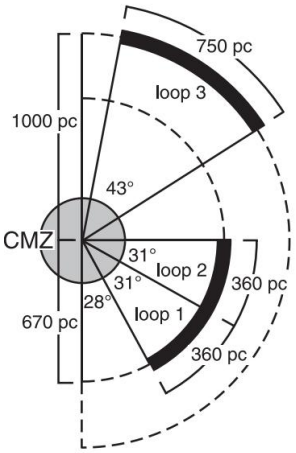

Figure 1.6: A schematic image of the locations of loops 1, 2, and 3 in the GC region. In this plane, the Sun is located at 8 kpc below the GC. (Credit: Torii, K, et al., A Detailed Observational Study of Molecular Loops 1 and 2 in the Galactic Center, PASJ, 2010, Vol. 62, Issue 5, p. 1307-1332, by permission of Oxford University Press.)

1.2.2 Theoretical Study of the Molecular Loops

Fukui et al. (2006) proposed the Parker instability (Parker 1966) as a possible mechanism for creating the molecular loops. Figure 1.7 schematically depicts how magnetic loops are formed by Parker instability. The condition for Parker instability can be derived as follows. We assume a magnetohydrostatic layer stratified by vertical gravity g. The magnetic field is assumed to be horizontal in the unperturbed state, and the stratified gas is assumed to be in the magnetohydrostatic equilibrium.

$$\frac{d(P_{\rm g}+P_{\rm m})}{dz} = -\rho g \tag{1.1}$$

where $P_{\rm g}$, $P_{\rm m}$ and ρ are the gas pressure, magnetic pressure and gas density, respectively. We assume that the plasma β (the ratio of gas pressure to magnetic pressure, $\beta = P_{\rm g}/P_{\rm m}$), the temperature T, and gravity g are constant. The density distribution is further given by

$$\rho(z) = \rho_0 \exp\left(\frac{-z}{H_{\rm m}}\right), \qquad H_{\rm m} = (1+\beta^{-1})\frac{k_{\rm B}T}{m_{\rm a}g} = (1+\beta^{-1})H_{\rm g} \tag{1.2}$$

where $H_{\rm m}$ and $H_{\rm g}$ are the scale heights with and without the magnetic field, respectively, and $k_{\rm B}$ and $m_{\rm a}$ denote the Boltzmann constant and average molecular weight, respectively.

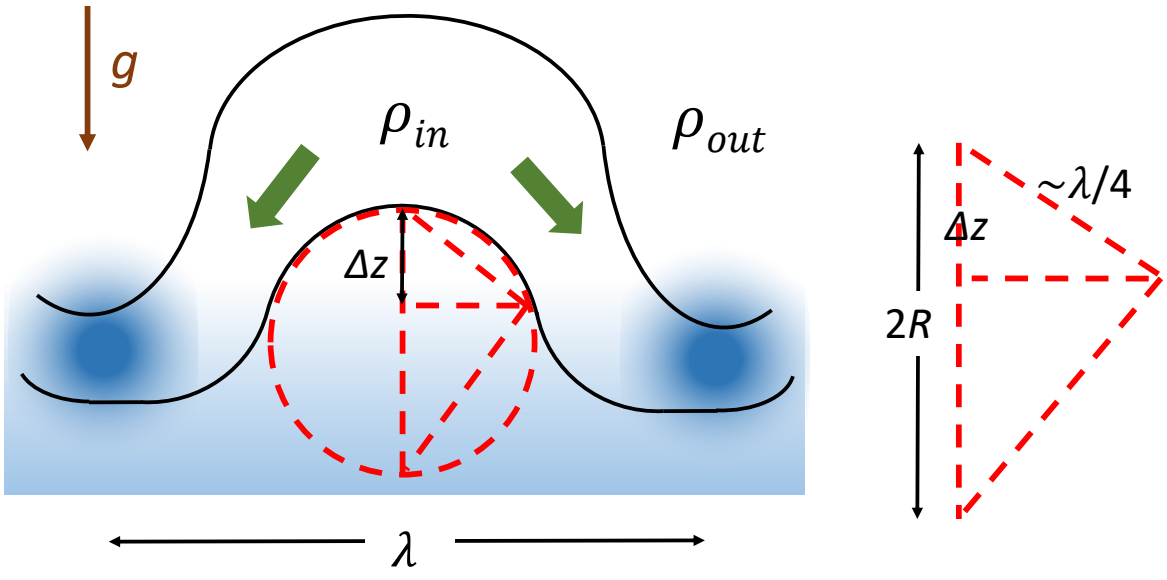

Figure 1.7: A schematic image of the Parker instability.

When a small perturbation of wavelength λ is imposed on the magnetohydrostatic gas as depicted in figure 1.7, buoyancy works around the top of the loop when $\rho_{\rm in} < \rho_{\rm out}$.

When the magnetic loop is levitated through a small displacement of Δz, the density of the gas inside the magnetic loop can be approximated as

$$\rho_{\rm in}(z+\Delta z) \sim \rho(z)\Big(1-\frac{\Delta z}{H_{\rm g}}\Big) \tag{1.3}$$

The density outside the magnetic loop is,

$$\rho_{\rm out}(z+\Delta z) \sim \rho(z)\Big(1-\frac{\Delta z}{H_{\rm m}}\Big). \tag{1.4}$$

Thus, the buoyancy force acting on the perturbed gas element can be given as

$$F_{\rm buoyacy} = -(\rho_{\rm in}(z+\Delta z) - \rho_{\rm out}(z+\Delta z))g \sim -\Big(\frac{\Delta z}{H_{\rm m}} - \frac{\Delta z}{H_{\rm g}}\Big)\rho(z)g = \beta^{-1}\frac{\Delta z}{H_{\rm m}}\rho(z)g \tag{1.5}$$

Here, we have assumed that $\Delta z \ll z$ and have further used a Taylor expansion. The Magnetic tension force can be evaluated from figure 1.7, as

$$F_{\rm tension} = \frac{B^2}{4\pi R} \tag{1.6}$$

where R is the curvature radius of the magnetic field line. Using similarity of the triangles in figure 1.7, we obtain $2R : \lambda/4 = \lambda/4 : \Delta z$. Instability occurs when $F_{\rm buoyancy} > F_{\rm tension}$. Thus, long-wavelength perturbations that satisfy

$$\lambda > \lambda_{cr} = 8H_{\rm g}\sqrt{1+\beta^{-1}} \tag{1.7}$$

are subjected to the Parker instability.

The Parker instability was originally proposed as a mechanism to explain the formation of interstellar clouds (Parker 1966). As depicted in figure 1.7, the interstellar gas sliding down along the magnetic field lines accumulates at the footpoints of the magnetic loops (the blue clump in figure 1.7). When this instability occurs in a warm interstellar gas ($T \sim 10^4$ K), cool ($T < 10^3$ K) clouds can be formed by cooling in the dense region.

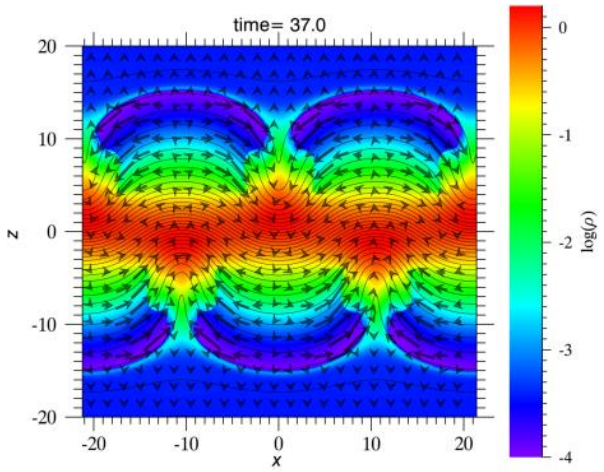

Figure 1.8: Density distribution (color), magnetic field lines (solid curves), and velocities (arrows) during the nonlinear stage of the development of the Parker instability. Lengths and densities are normalized by $H_0 = 3.086 \times 10^{20}$ cm and $\rho_0 = 1.6 \times 10^{-24}$ g cm^{-3} (Kudoh 2017).

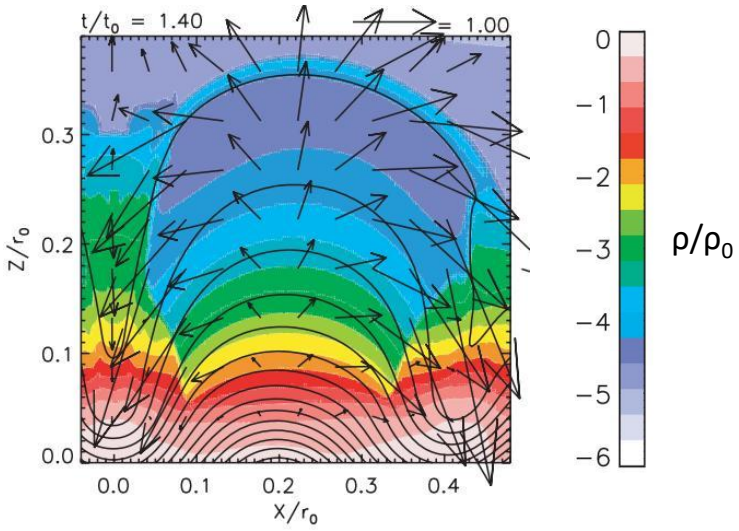

Figure 1.9: Density distribution (color), magnetic field lines (solid curves), and velocities (arrows) obtained by two-dimensional simulation of the Parker instability. Lengths and densities are normalized by $r_0 = 1$ kpc and $\rho_0 = 10^{-22}$ g cm^{-3}. (Credit: Takahashi, K., et al., Similarity between the Molecular Loops in the Galactic Center and the Solar Chromospheric Arch Filaments, PASJ, 2009, Vol. 61, Issue 5, p. 957-969 , by permission of Oxford University Press.)

Figure 1.8 shows the result of a two-dimensional simulation of Parker instability (Kudoh 2017). Matsumoto et al. (1988, 1990) showed by two-dimensional MHD simulations that the levitated gas slides down along the rising magnetic loops and forms dense spurs in the valleys between the magnetic loops. Furthermore, they showed that the loop-spur structure becomes quasi-steady when the magnetic field is strong ($\beta < 1$). When the velocity of the downflowing gas exceeds the sound speed, shock waves are formed around the footpoints of the magnetic loops. Shibata et al. (1991) proposed that dense molecular clouds can be formed by the shock compression of the accumulated gas.

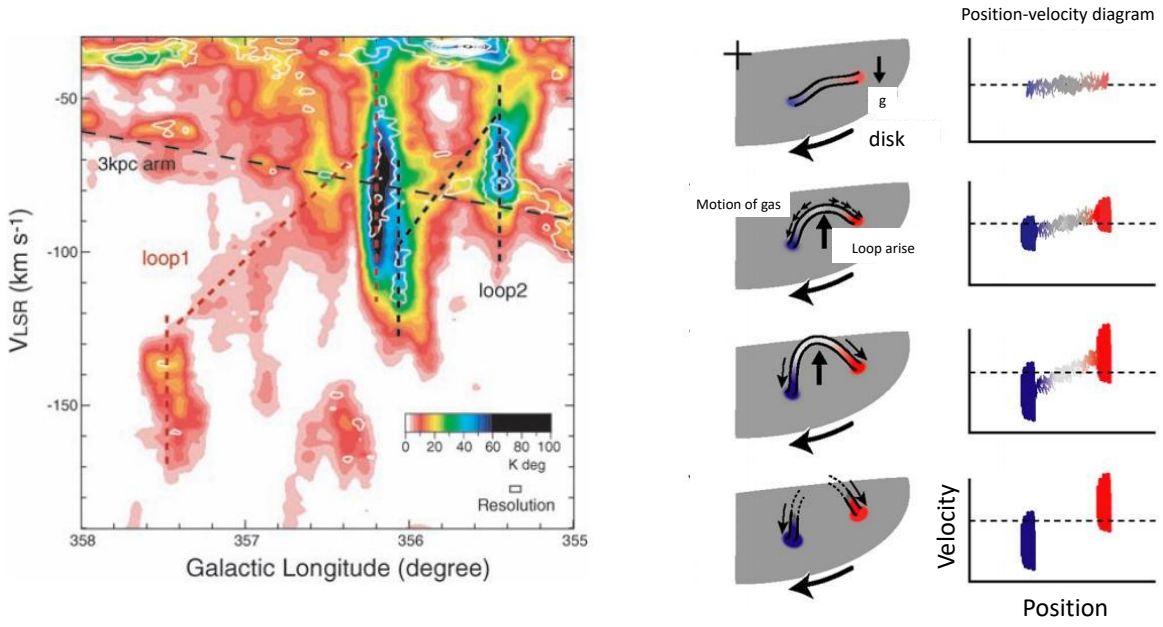

Figure 1.10: (left) Position-velocity diagram for loops 1 and 2. (Credit: Fukui, Y., et al., Molecular Loops in the Galactic Center: Evidence for Magnetic Flotation, Science, 2006, Vol. 314, Issue 5796, p. 106-109. https://doi.org/10.1126/science.1130425 Reprinted with permission from AAAS.) (right) Schematic drawings that depicts a mechanism by which a position-velocity diagram can be reproduced by the Parker instability in the Galactic disk. (Credit: Torii, K., et al., Magnetically floated loops in the galactic center, The Astronomical Herald, 2007, Vol. 100, No. 11, p. 581-585.)

Fukui et al. (2006) adopted the Parker instability model to explain the systematic variation of the line of sight velocities along the loop (Figure 1.10) and the large velocity dispersions around the footpoints of the loops. The velocity gradient along the loop can be explained by the motion of the dense gas sliding down along the rising magnetic loops created by the Parker instability and by the Galactic rotation (Machida et al. 2009). The large velocity dispersions that are observed around the footpoints of the loops can be explained by shock waves formed in the region where the supersonic downflow hits the gas in the Galactic disk (Matsumoto et al. 1988, 1990; Shibata and Matsumoto 1991; Machida et al. 2009; Takahashi et al. 2009). Figure 1.9 shows a result from Takahashi et al. (2009) in which the cool ($T \sim 10^3$ K), warm ($T \sim 10^4$ K), and hot components of the interstellar medium are considered. They demonstrated that the density enhancements can be created above the rising loops. However, the density around the top of the loop is less than $\rho = 10^{-25}$ g cm^{-3}, which is much smaller than that observed in the molecular loop. Dense filaments are not formed in their simulations because they did not consider the transition between warm and cool gas. In order to create dense molecular loops, we have to take into account the cooling of the warm interstellar gas. In the following section, we introduce a cooling function of ISM.

1.3 Interstellar Cooling and Heating

Here, we review the thermal state of the interstellar medium (ISM), which comprises gas (atoms, molecules, and ions), dust, and cosmic rays. The average number density of the gas in the ISM is $\sim$1 cm^{-3}, and the interstellar dust contains of heavy elements such as silicon, carbon, magnesium, and so on. The thermal state of the ISM is determined by the balance between the cooling and heating processes.

By considering the cosmic rays heating and radiative cooling due to the collisional excitation of H, He and CII, Field (1969) proposed a two-phase ISM model. In this model, the ISM consists of a cold neutral medium (CNM) in which the temperature is lower than 300 K and a warm medium (WM) in which temperature is approximately 10^4 K, and the two phases coexist in pressure equilibrium. The warm medium includes both a warm neutral medium (WNM) and a warm ionized medium (WIM). More recently, Wolfire et al. (1995) re-evaluated the thermal equilibrium of the ISM by considering the cooling and

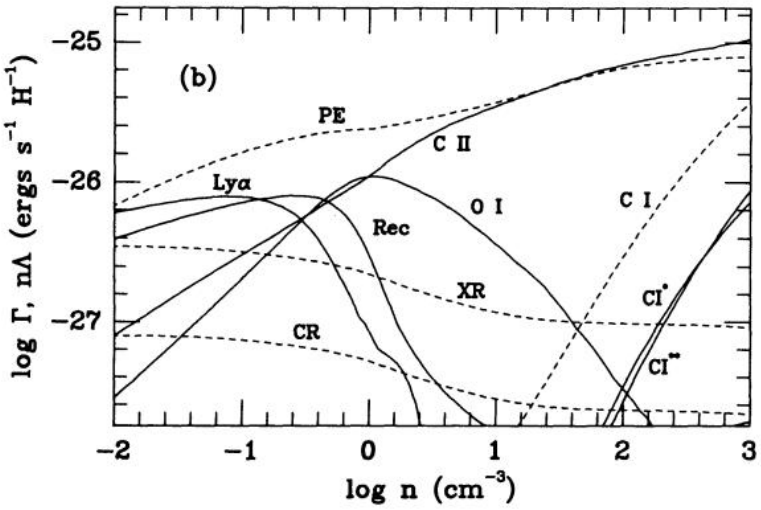

Figure 1.11: The cooling and heating rates in the ISM. The vertical axis shows the cooling(heating) rate, whereas horizontal axis shows number density on a log scale. The solid curves depict the cooling rates due to Lyα emission (Lyα), recombination (Rec) on grains and polycyclic aromatic hydrocarbon (PAHs), CII fine structure (CII), OI fine structure (OI), and CI fine structure (CI* and CI**). The dashed curves depicts the heating rates that are caused by the photoelectric effects (PE) on small grains and PAHs, X-rays (XR), cosmic rays (CR), and photoionization of carbon (CI). (Credit: Wolfire, M. G., Hollenbach, D., McKee, C. F., Tielens, A. G. G. M., Bakes, E. L. O., The neutral atomic phases of the interstellar medium, ApJ, Vol. 441, p. 152-168, 1995 Apr 10. https://doi.org/10.1086/175510 © AAS. Reproduced with permission.)

the heating processes depicted in figure 1.11. They included cooling due to hydrogen Lyα emission, recombination on grains and polycyclic aromatic hydrocarbon (PAHs), and the fine structure lines of CII, OI, and CI; further, they incorporateed heating processes such as photoelectric effect on gains and PAHs, X-rays, cosmic rays and the photoionization of carbon. Wolfire et al. (2003) investigated the dependence of the cooling/heating processes on radial distance from the center of the Milky Way Galaxy and they obtained thermal equilibrium curves at different radii (figure 1.12). Koyama & Inutsuka (2000) determined the cooling/heating rates of the dense, cold ISM over the number density range of 10^3 cm$^{-3} < n < 10^6$ cm^{-3}.

The cooling/heating function can be approximated using a fitting function (Koyama & Inutsuka 2002, Inoue et al. 2006). Figure 1.13 depicts a thermal equilibrium curve that was obtained by applying the cooling/heating functions summarized by Inoue et al.

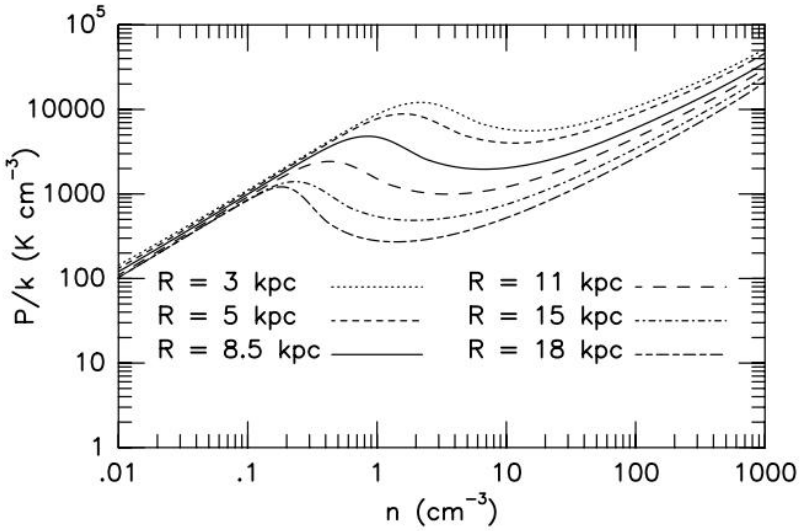

Figure 1.12: Thermal equilibrium curves at R = 3, 5, 8.5, 11, 15, and 18 kpc from the Galactic Center. The horizontal axis is the number density, whereas the vertical axis is the pressure. (Credit: Wolfire, M. G., McKee, C. F., Hollenbach, D., Tielens, A. G. G. M., Neutral Atomic Phases of the Interstellar Medium in the Galaxy, ApJ, Vol. 587, Issue 1, p. 278-311, 2003 Apr 10. https://doi.org/10.1086/368016 © AAS. Reproduced with permission.)

(2006). There are two stable states ($\frac{d\ln P}{d\ln n} > 0$): a warm state (red part) with temperature of $\sim$ 8000 K and a cold state (blue part) with a temperature of $\sim$ 50 K, respectively. Intermediate states between these two thermal equilibrium states are thermally unstable. We note that significant amounts of the ISM actually lie in between the warm and the cold states (e.g, Fukui et al. 2017).

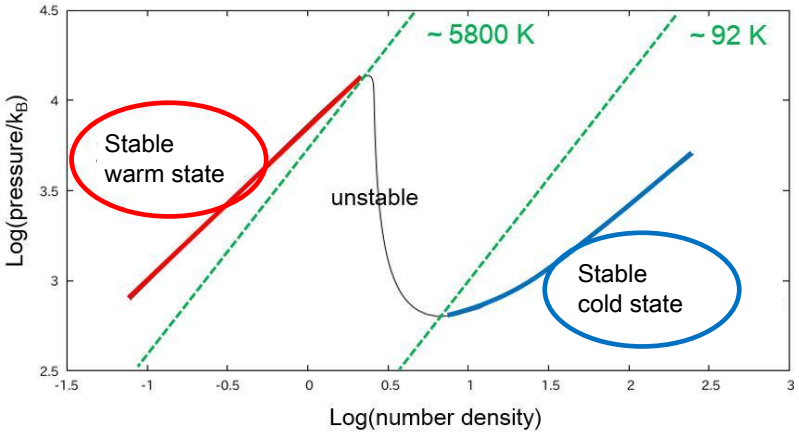

Figure 1.13: Thermal equilibrium curve for the ISM obtained by applying cooling/heating function by Inoue et al. (2006). The horizontal axis is the number density, whereas the vertical axis is the pressure.

1.4 Formation of Dense Filaments by the Parker Instability by Including Cooling

Mouschovias et al. (2009) performed simulations of the Parker instability that included cooling of and thermal conduction in the interstellar medium. They adopted the cooing/heating function $\rho\mathcal{L}$ that was given by Koyama and Inutsuka (2002).

$$\rho\mathcal{L} = (-\Gamma + n\Lambda)n, \tag{1.8}$$

$$\Gamma = 2 \times 10^{-26} \text{ erg s}^{-1}, \tag{1.9}$$

$$\frac{\Lambda}{\Gamma} = 10^7 \exp\Big(\frac{-118400}{T+1000}\Big) + 1.4 \times 10^{-2}\sqrt{T}\exp(-92/T) \text{ cm}^3. \tag{1.10}$$

Here n is number density, T is temperature, $n\Gamma$ and $n^2\Lambda$ are heating and cooling term respectively. They included thermal conduction with coefficient κ given by

$$\kappa = \frac{\rho^2\Lambda}{T}\Big(\frac{\Delta y}{\pi}\Big)^2 \max\Big[1 - \frac{\partial \ln\Lambda}{\partial \ln T}, 0\Big], \tag{1.11}$$

where Δy is computational mesh size. They demonstrated that an interstellar gas with high number density ($\sim 10^3$ cm^{-3}) and low temperature ($\sim$ 50 K) can be formed in the valleys of the magnetic field lines and in the Galactic disk (Figure 1.14). The typical mass accumulated in a dense filament is $\sim 10^5$ M$_\odot$. Since the density around the rising magnetic loops was much less than the critical density ρ_c to induce the cooling instability in warm interstellar gas ($\rho_c \sim 10^{-23}$ g cm^{-3}), no dense cool ($T < 10^3$ K) loop was formed during their simulation.

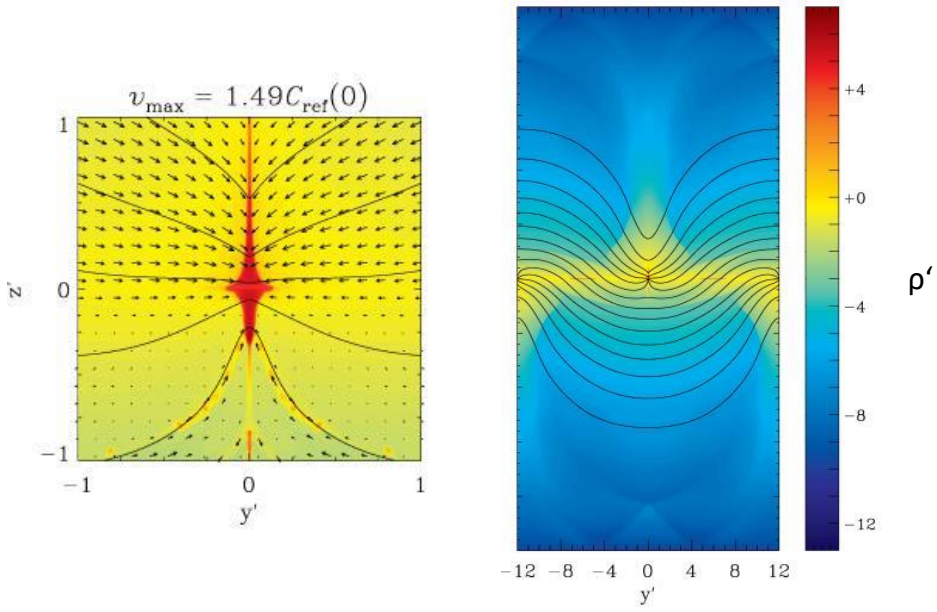

Figure 1.14: Density distribution obtained from the simulation of Parker instability that consider the cooling and heating processes (Mouschovias et al. 2009). The unit of length is 35.45 pc. The color scale depicts the density normalized by 2.1×10^{-24} g cm^{-3}. (Credit: Figure 4 and 5, Formation of interstellar clouds: Parker instability with phase transitions, Mouschovias, Telemachos Ch., Kunz, Matthew W., Christie, Duncan A., MNRAS, Vol. 397, Issue 1, p. 14-23.)

1.5 Models of Prominence Formation

1.5.1 Similarity between the Solar Prominences and Galactic Center Magnetic Loops

The Parker instability can explain the velocity gradient along the dense loops and the large velocity dispersions around the footpoints of the loops. However, it cannot explain how a dense molecular gas (number density > 100 cm^{-3}) is elevated in the warm interstellar medium (with the number density of a few cm^{-3}). The observed levitated dense filaments are similar to solar prominences for which the density is 10-100 times larger than that in the surrounding solar corona. Figure 1.15 shows a prominence observed in the Hα line by *Hinode*/SOT (Schmieder et al. 2010). Note that the solar prominences are warm gas with temperatures of 10^4 K, while the molecular loops are cold molecular gas with temperatures less than 100 K. Although the temperature and cooling mechanisms in solar prominences are different from those in the molecular loops, the density ratio between the dense filament and the ambient gas is similar in both the cases. Accordingly, Morris (2006) and Torii et al. (2010b) have discussed the probability that the formation mechanism of the molecular loops may be similar to that of the solar prominences. Thus, understanding the physical processes that cause the formation of solar prominences is a key factor in understanding the formation mechanism of molecular loops.

1.5.2 Two Types of Solar Prominences

As mentioned in the previous subsection, solar prominences are relatively cool, dense plasma that are formed in the hot corona. Prominences are classified into two types, which are schematically depicted in figure 1.16 . In a normal-polarity prominence, the magnetic polarity of the prominence is similar to that of the overlying arcade field. This type can be explained by a model proposed by Kippenhahn & Schlüter (1957; the KS model). In this model, the dense cold gas that accumulates in the valley of an undulating magnetic loop is supported by the magnetic tension force against gravity. The other type is an inverse-polarity prominence in which the magnetic polarity of the prominence is opposite to that of the overlying arcade field. This model of a prominence was proposed by Kuperus & Raadu (1974; the KR model).

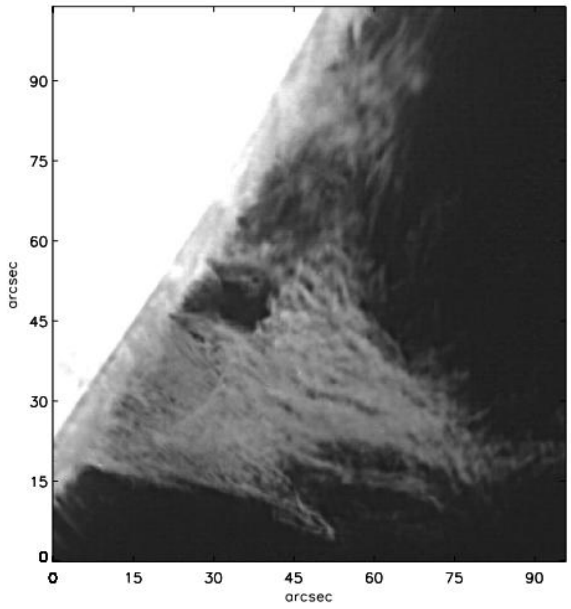

Figure 1.15: A solar prominence observed in Hα by *Hinode*/SOT at 13:19:50 UT on April 25, 2007. (Credit: Schmieder, B., Chandra, R., Berlicki, A., Mein, P., A&A, vol. 514, A68, 2010, reproduced with permission © ESO.)

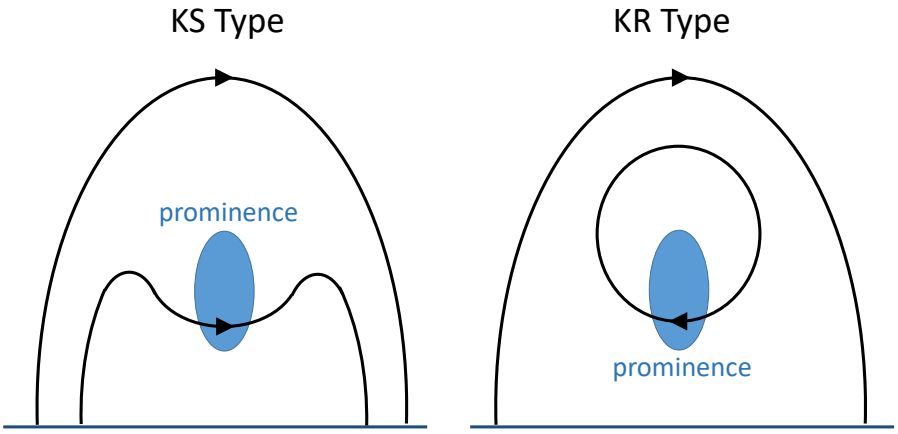

Figure 1.16: Schematic images of a normal-polarity prominence, called a KS type (left), and an invese-polarity prominence, called a KR type (right).

1.5.3 Numerical Simulations of the Formation of Solar Prominences

In both the KS and the KR models, prominences are formed by cooling the dense blobs accumulated in a valley of magnetic field lines. Choe & Lee (1996a; 1996b) performed

two-dimensional simulations of the formation of a KR-type prominence by imposing a shearing motion at the footpoints of the initial arcade-like magnetic field. The imposed shear flow triggers the expansion of the magnetic arcade. Figures 1.17 and 1.18 show their results. Figure 1.17 illustrates the result when resistivity is neglected. As the magnetic arcade rises, a current sheet is formed around $x = 0$ inside the expanding loop. When the resistivity is considered (Figure 1.18), however, magnetic reconnection takes place in the current sheet, thereby forming a plasmoid that is ejected upward.

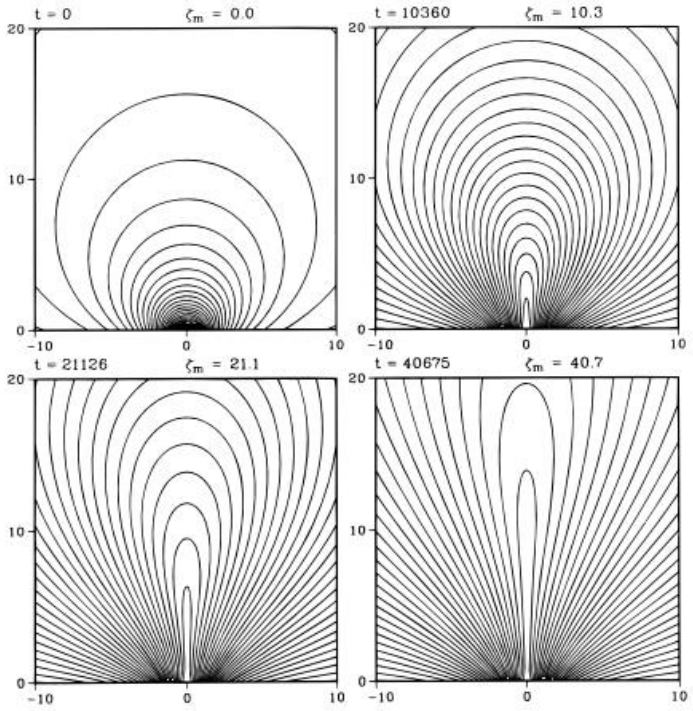

Figure 1.17: Time evolution of magnetic archades obtained by the two-dimensional ideal MHD simulations in which shear motions are imposed around the footpoints of the magnetic loops. The solid curves depict the magnetic field lines. (Credit: Choe, G. S., Lee, L. C., Evolution of Solar Magnetic Arcades. I. Ideal MHD Evolution under Footpoint Shearing, ApJ, Vol. 472, p. 360-371, 1996 Nov 20. https://doi.org/10.1086/178069 © AAS. Reproduced with permission.)

Eruptions of the magnetic arcades have been studied extensively as the models of solar flares as well as the prominence eruptions. Figure 1.19 illustrates the unified model of a solar flare (Shibata et al. 1995), in which magnetic reconnection occurs in the current sheet formed inside an inflating magnetic arcade and releases the magnetic energy along with triggering the plasmoid ejections and supersonic plasma flows. This model is based

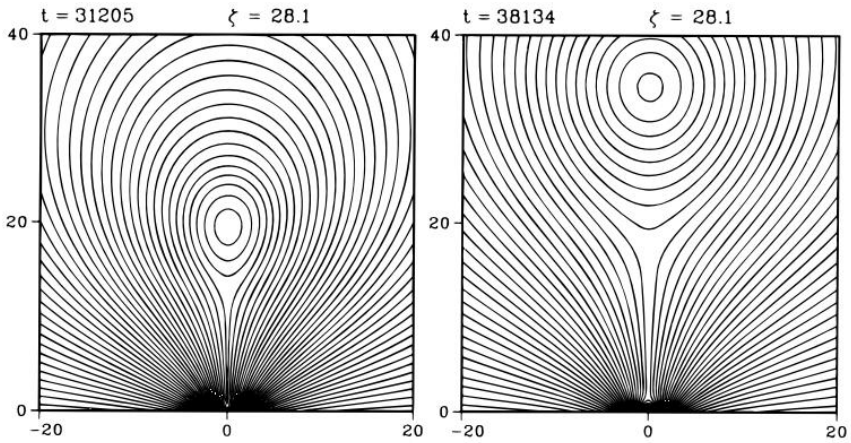

Figure 1.18: Time evolution of a magnetic arcade obtained by 2D resistive MHD simulations. The solid curves depict the magnetic field lines. (Credit: Choe, G. S., Lee, L. C., Evolution of Solar Magnetic Arcades. II. Effect of Resistivity and Solar Eruptive Processes, ApJ, Vol. 472, p. 372-388, 1996 Nov 20. https://doi.org/10.1086/178070 © AAS. Reproduced with permission.)

on the Yohkoh observations of solar flares, in which a cusp is formed at the top of a soft X-ray emitting loop (e.g., Tsuneta et al. 1992). Hard X-ray emitting regions that were formed around the top of the loop indicate that a supersonic downflow created by magnetic reconnection is striking the magnetic loop (Masuda et al. 1995).

Xia et al.(2014) conducted three-dimensional MHD simulations of the KR-type prominence formation by including radiative cooling, heating and thermal conduction. They showed that dense cool prominences can be formed inside a flux rope. However, their initial condition did not satisfy the thermal equilibrium because radiative cooling dominates inside the flux rope. Recently, Kaneko & Yokoyama (2015) have conducted the MHD simulations related to the formation of a KR prominence starting from a magnetostatic atmosphere in thermal equilibrium. They adopted the scenario proposed by van Ballegooijen & Martens (1989), in which, the magnetic arcades are inflated by injection of shear and converging motion at the footpoints of magnetic arches anchored to the solar photosphere. As the magnetic loops rise, a current sheet is formed around $x = 0$. During magnetic reconnection, a plasmoid is formed and ejected. Kaneko & Yokoyama (2015) conducted simulations by considering the cooling and showed that the dense plasma trapped in the flux rope condenses by radiative cooling and forms cool, dense filaments. Figures 1.20 and 1.21 show the results of their two-dimensional resis-

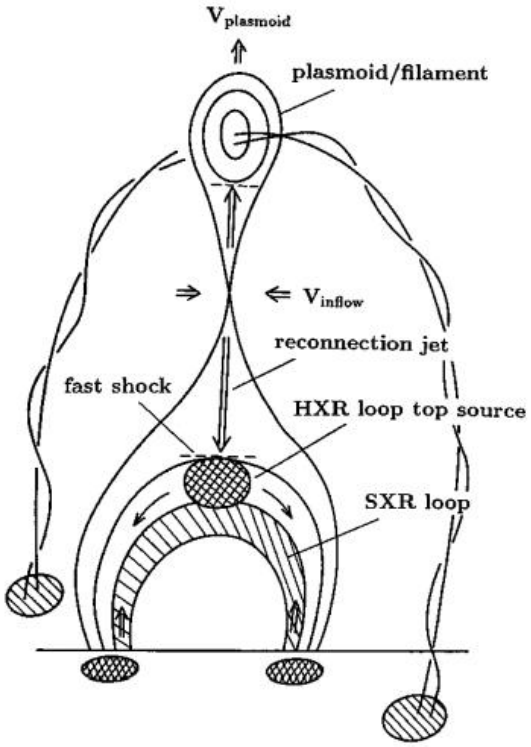

Figure 1.19: Schematic image of a unified model of a solar flare. (Credit: Shibata, K., Masuda, S., Shimojo, M., Hara, H., Yokoyama, T., Tsuneta, S., Kosugi, T., Ogawara, Y., Hot-Plasma Ejections Associated with Compact-Loop Solar Flares, ApJL, Vol. 451, p. L83-L85, 1995 Oct 1. https://doi.org/10.1086/309688 © AAS. Reproduced with permission.)

tive MHD simulations. The dense cool filaments are formed in the magnetic flux ropes that were created by magnetic reconnection. In the simulations by Kaneko & Yokoyama (2015), anisotropic thermal conductivities that depends on the direction of the magnetic fields are considered because thermal conduction plays a key role in heating/cooling the plasma in the solar corona when the magnetic field lines connect the hot and cool regions. In two-dimensional simulations, the plasma in a magnetic flux rope is thermally disconnected from the region outside the flux rope because the thermal conductivity $\kappa_\perp$ across the magnetic field lines is much smaller than that parallel to the magnetic field lines ($\kappa_\parallel$) in a rarefied plasma. This enables the cooling of the plasma inside the magnetic flux rope.

Kaneko & Yokoyama (2017) reported the results of three-dimensional resistive MHD simulations of prominence formation. Figure 1.22 depicts the density distribution and

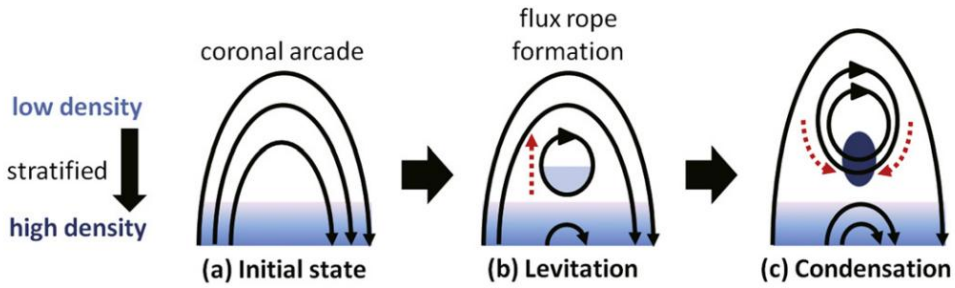

Figure 1.20: Schematic image of the reconnection-condensation model of prominence formation proposed by Kaneko & Yokoyama (2015). (Credit: Kaneko, T., Yokoyama, T., Numerical Study on In-Situ Prominence Formation by Radiative Condensation in the Solar Corona, ApJ, Vol. 806, Issue 1, article id. 115, 10 pp., 2015 Jun 10. https://doi.org/10.1088/0004-637X/806/1/115 © AAS. Reproduced with permission.)

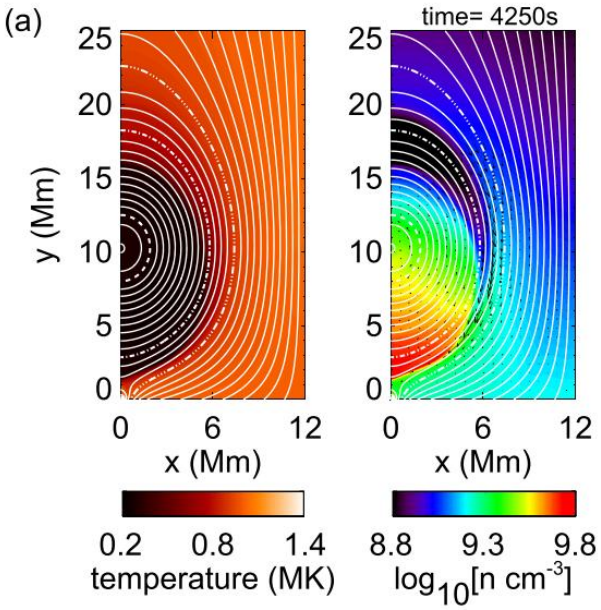

Figure 1.21: Density and temperature distributions after plasmoid formation, which was obtained from the two-dimensional simulations of prominence formation. (Credit: Kaneko, T., Yokoyama, T., Numerical Study on In-Situ Prominence Formation by Radiative Condensation in the Solar Corona, ApJ, Vol. 806, Issue 1, article id. 115, 10 pp., 2015 Jun 10. https://doi.org/10.1088/0004-637X/806/1/115 © AAS. Reproduced with permission.)

magnetic field lines that were obtained from their three-dimensional simulations. The dense cool gas is sustained against gravity in the magnetic valleys. In the three-dimensional

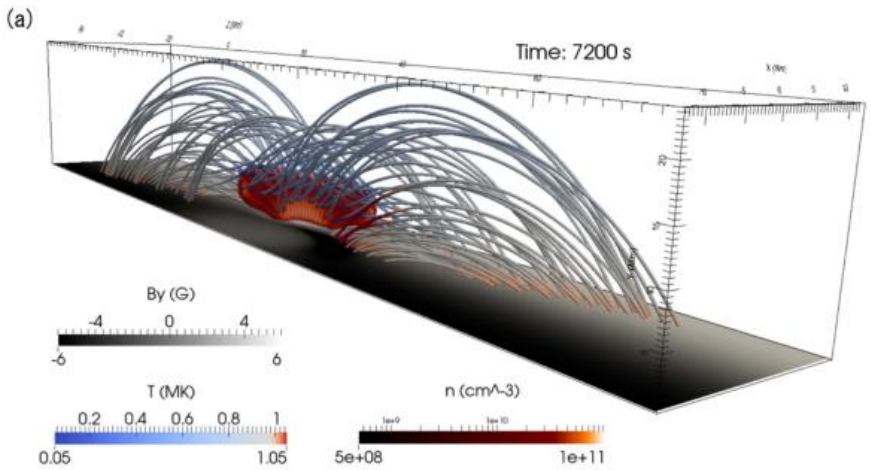

Figure 1.22: Distributions of density, temperature, and magnetic field lines obtained by the three-dimensional resistive MHD simulations of prominence formation. (Credit: Kaneko, T., Yokoyama, T., Reconnection-Condensation Model for Solar Prominence Formation, ApJ, Vol. 845, Issue 1, article id. 12, 10 pp., 2017 Aug 10. https://doi.org/10.3847/1538-4357/aa7d59 © AAS. Reproduced with permission.)

simulations, thermal conduction can trasport heat along the reconnected magnetic field lines and suppress the cooling of the dense gas. The dense cool filaments can therefore be formed when the length of a magnetic loop is long enough so that the timescale for radiative cooling becomes shorter than the timescale for thermal conduction along the magnetic field lines (Kaneko & Yokoyama 2017).

Since dense prominences are supported by the magnetic field against gravity, the bottom surface of a cool dense filament is subjected to the magnetic Rayleigh-Taylor instability. Accordingly, we have to conduct three-dimensional simulations to study the growth of this instability because the instability grows for perturbations with wave vectors perpendicular to the magnetic field lines. The results of the three-dimensional MHD simulations (Kaneko & Yokoyama 2017) indicate that the magnetic Rayleigh-Taylor instability is partially suppressed by the sheared magnetic field lines.

1.6 Comparison between Galactic Prominences and Solar Prominences

In this subsection we compare the Galactic prominences and solar prominences. Table 1.1 shows the typical parameters for our model of GC prominences and for solar prominences that were adopted in the simulation by Kaneko & Yokoyama (2015).

Quantity	unit	Galactic Prominence	Solar Prominence
Length	H_0	200 pc	31 Mm
Temperature	$T_{\rm cool}$	100 K	10^5 K
	$T_{\rm hot}$	10^4 K	10^6 K
Velocity	v_0	10 km/s	117 km/s
Time	$t_0 = H_0/v_0$	17 Myr	264 s

Table 1.1: Typical parameters for Galacitc Center prominences and the solar prominences adopted for simulations by Kaneko & Yokoyama (2015).

1.7 Effects of Thermal Conduction in Galactic Prominences

In Galactic prominences, since $T < 10^4$ K, the thermal conductivity can be expressed as $\kappa = 2.5 \times 10^3\ T^{1/2}$ in a CGS unit (Parker 1953). The time scale for thermal conduction is estimated to be $t_{\rm cnd} \sim 10^4$ Myrs if we consider n =1.0 cm^{-3}, T =10^4 K, and L =10 pc. This is longer than the timescale that is required for the formation of molecular loops as estimated by Fukui et al. (2006). Here, we note that thermal conduction determines the widths of the cool dense filaments in interstellar space. If the width of a filament is d, the cooling timescale becomes comparable to t_{cnd} when $d \sim 0.1$ pc. Recent observations of the CMZ using ALMA revealed that the widths of the dense filaments in the CMZ are $d \sim 0.1$ pc (Uehara et al. 2017), which is consistent with the aforementioned discussion. Furthermore, thermal conduction on sub-pc scales can drive the turbulence (Inoue et al. 2007). Therefore, we need to consider the thermal conductivity while we discuss the stability of dense filaments having thickness ~ 0.1 pc in the Galactic disk. On the

other hand, during the formation of a thin dense filament, thermal conductivity can be neglected if the width of the filament is $d \ll 0.1$ pc.

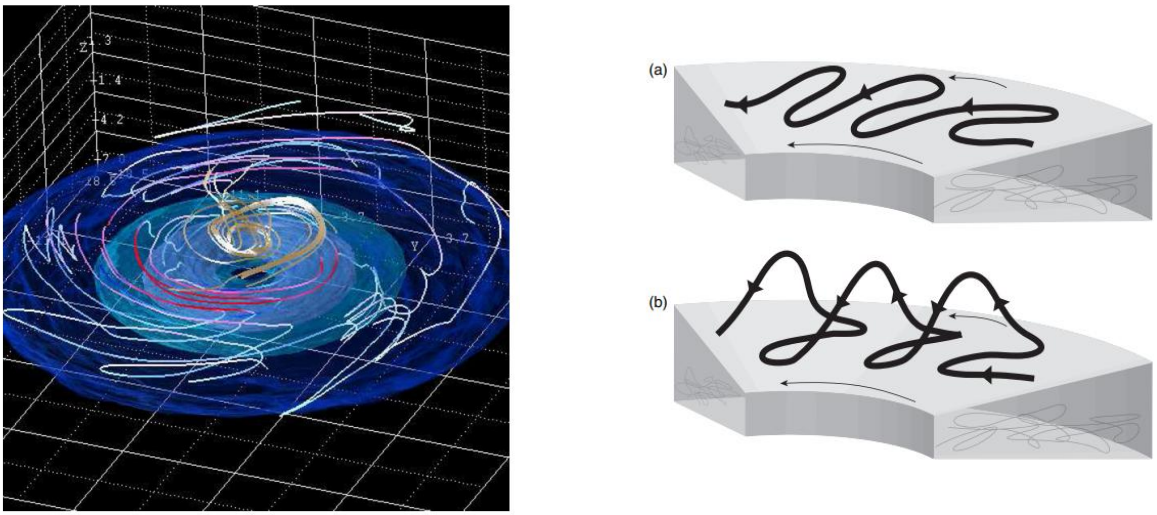

Figure 1.23: (left) A simulation result of the evolution of magnetic field lines in the Galactic disk. The solid curves and colored region depict the mean magnetic field lines and surfaces of constant density, respectively. (right) Schematic pictures of the mechanism of the MRI-Parker dynamo. (Credit: Machida, M., Nakamura, K. E., Kudoh, T., Akahori, T., Sofue, Y., Matsumoto, R., Dynamo Activities Driven by Magnetorotational Instability and the Parker Instability in Galactic Gaseous Disks, ApJ, Vol. 764, Issue 1, article id. 81, 9 pp., 2013 Feb 10. https://doi.org/10.1088/0004-637X/764/1/81 © AAS. Reproduced with permission.)

1.8 Effects of the Magneto-Rotational Instability (MRI)

In the solar atmosphere, magnetic arcades are formed when the magnetic loops emerge buoyantly from the solar convective zone into the solar corona. In the galactic gas disks and accretion disks, magnetic fields that are amplified inside the disks by MRI escape from the disks by buoyancy, as demonstrated by the three-dimensional global MHD simulations (e.g, Nishikori et al. 2006; Machida et al. 2009, 2013; Suzuki et al. 2015; Kakiuchi et al. 2017). The left-hand panel of figure 1.23 depicts the density distribution and magnetic field lines obtained by one of these simulations (Machida et al. 2013). The magnetic fields inside the disk are mainly azimuthal; however, buoyantly rising magnetic loops can be identified from figure 1.23. The right-hand panel schematically shows the mechanism

of formation of magnetic loops.

Magnetic loops formed by the Parker instability can be twisted by differential rotation, and the footpoint motions of these magnetic loops can drive further inflation of the loops. The three-dimensional simulations of differentially rotating disks show that the inflation of the magnetic loops and magnetic reconnection can trigger plasmoid ejections and produce large scale poloidal magnetic fields threading the disk (e.g, Kato et al. 2004, Machida et al. 2008).

1.9 Aim of This Thesis

In this thesis, the results of two- and three-dimensional MHD simulations are presented based on the model of solar prominences proposed by Kaneko & Yokoyama (2015, 2017). The cooling/heating function from Inoue et al. (2006) is adopted, in which radiative cooling due to emission lines, the photoelectric effect on dust, cosmic rays, etc., have been included. It is demonstrated that dense loop-like structures near the GC can be formed by the condensation of the warm interstellar medium. The total mass, line of sight velocities, and column densities of dense loop structures will be determined. The numerical models and results of two-dimensional simulations are presented in Chapter 2. Since Galactic rotation is not negligible for the formation of magnetic arcades, numerical simulations are conducted in the frame co-rotating with the disk. Numerical results of these simulations are shown in Chapter 3. In Chapter 4, we show numerical results that consider the gravitational potential near the GC. The Results of three-dimensional simulations are shown in Chapter 5, Chapter 6 is for summary and discussion.

Chapter 2

Two-Dimensional Numerical Simulations of Galactic Prominence Neglecting Disk Rotation

In this chapter, we present the results of two-dimensional MHD simulations of the formation of dense horizontal filaments (prominence) floating above the Galactic gas disk. The condensation of the warm interstellar medium is simulated in the plane perpendicular to the dense filament. In section 2.1, we present a numerical model. Basic equations, numerical scheme and initial/boundary conditions are presented in section 2.2 to 2.4. Numerical results for non-rotating disk are given in section 2.5.

2.1 In-situ Formation Model of Galactic Prominence

We adopted the in-situ formation model of solar prominences reported by Kaneko & Yokoyama (2015). Figure 2.1 schematically shows the formation mechanism of dense, cold filaments. We consider static magnetic arcades at the initial state (figure 2.1(a)). Subsequently, we impose converging and shearing motion at the footpoints of the arch to induce the rising motion of the arcade. Note that both the magnetic buoyancy around the loop top of the arch and the magnetic pressure gradient enhanced by the footpoint motion contribute to the rising motion of the arch. Current sheets can be formed inside the expanding magnetic arcade. Magnetic reconnection taking place in the current sheet forms rising dense plasmoids (figure 2.1(b)). Since the plasmoid is confined by the helical

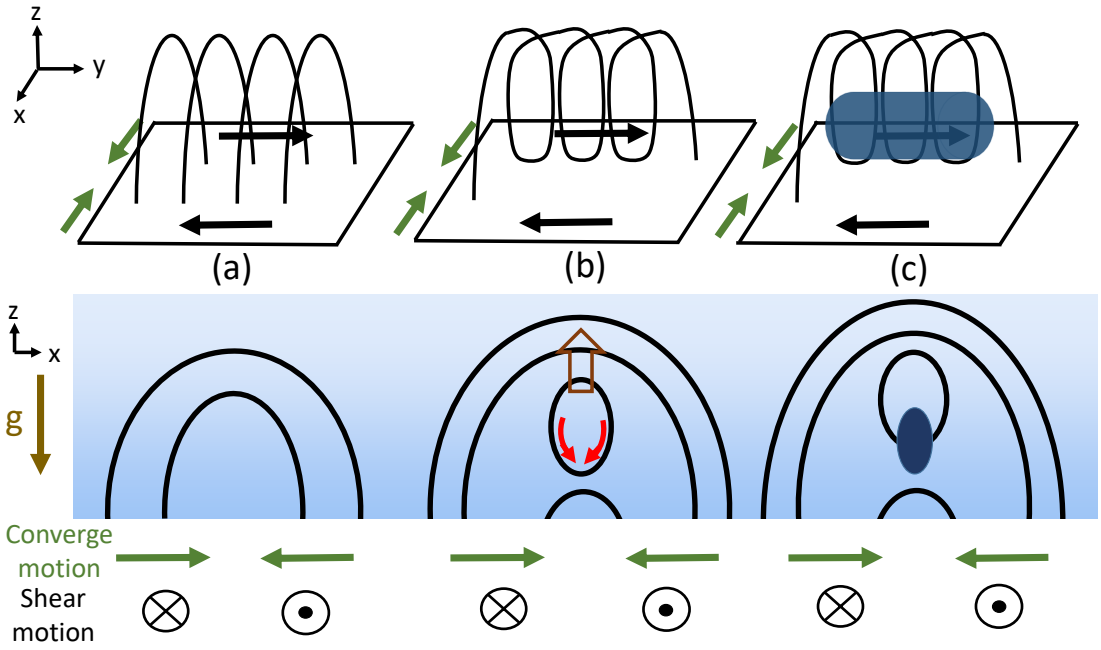

Figure 2.1: Schematic picture of a molecular loop formation. (a) Magnetic arches and footpoint motions (b) Closed magnetic loops (helical magnetic fields in three-dimension) are formed by magnetic reconnection taking place in the arch expanding by the imposed converging/shear motion. (c) Cooling instability taking place around the bottom of the magnetic flux rope forms dense, cool filaments (dark region).

magnetic fields, the warm gas accumulates around the bottom of the closed poloidal magnetic field lines (red arrows), where the cooling instability forms dense, cold filaments supported by magnetic tension force (figure 2.1(c)). In this chapter, since we neglect the variation of physical quantities perpendicular to the poloidal plane, the dense filaments are not arches but straight filaments.

2.2 Basic Equations for Non-rotating, Gravitationally Stratified Disk

In this section, we neglect rotation of the disk. The basic equations of resistive magnetohydrodynamics (MHD) are as follows:

$$\frac{\partial \rho}{\partial t} + \nabla \cdot (\rho \boldsymbol{v}) = 0 \tag{2.1}$$

$$\frac{\partial (\rho \boldsymbol{v})}{\partial t} + \nabla \cdot (\rho \boldsymbol{v}\boldsymbol{v}) = -\nabla P - \rho \boldsymbol{g} + \frac{(\nabla \times \boldsymbol{B}) \times \boldsymbol{B}}{4\pi} \tag{2.2}$$

$$\frac{\partial \boldsymbol{B}}{\partial t} = \nabla \times (\boldsymbol{v} \times \boldsymbol{B} - \eta \nabla \times \boldsymbol{B}) \tag{2.3}$$

$$\frac{\partial E}{\partial t} + \nabla \cdot \left[\left(E + P + \frac{B^2}{8\pi} \right) \boldsymbol{v} - \frac{\boldsymbol{B}(\boldsymbol{B} \cdot \boldsymbol{v}) - \eta (\nabla \times \boldsymbol{B}) \times \boldsymbol{B}}{4\pi} \right] = \rho \boldsymbol{v} \cdot \boldsymbol{g} - \rho \mathcal{L} \tag{2.4}$$

$$E = \frac{P}{\gamma - 1} + \frac{\rho v^2}{2} + \frac{B^2}{8\pi} \tag{2.5}$$

where γ is the specific heat ratio which we take $\gamma = 5/3$. The anomalous resistivity η is assumed to depend on the current density $J = c\nabla \times \boldsymbol{B}/4\pi$ (see Kaneko & Yokoyama 2015) as

$$\eta = \begin{cases} 0 & J < J_c \\ \eta_0 (J/J_c - 1)^2 & 4.16 J_c > J \geq J_c \\ 10\eta_0 & J \geq 4.16 J_c \end{cases} \tag{2.6}$$

Here $\eta_0 = 3 \times 10^{23}$ cm^2 s^{-1} and $J_c = 4.0 \times 10^{-17}$ dyn$^{1/2}$ cm s^{-1}. We adopt Cartesian coordinates (x, y, z) and assume translational symmetry with respect to y. The magnetic Reynolds number $R_\mathrm{m} = UL/\eta$ where the characteristic speed is U =10 km/s and the characteristic length is L =100 pc is $R_\mathrm{m} = 1000$. Electric resistivity is assumed to be non-zero only in the region where the current density exceeds J_c. The gravitational acceleration is assumed to be $\boldsymbol{g} = (0, 0, g_z)$ and $g_z = 3 \times 10^{-9}$ cm s^{-2}, for the fiducial model, which indicates that the scale height H for the warm interstellar gas with the sound speed $c_\mathrm{s} = 10$ km/s is $H = c_\mathrm{s}^2/g_z = 100$ pc. Cooling function $\rho\mathcal{L}$ includes cooling and heating term and other symbols have their normal meaning. In the interstellar medium, cold neutral medium with temperature 10-100 K and warm medium with temperature 10^4 K coexists by the balance of cooling and heating (Field 1965). We adopted cooling/heating

function summarized by Inoue et al. (2006).

$$\rho\mathcal{L} = \begin{cases} (-\Gamma + n\Lambda)n & 400\ \mathrm{K} < T < 20000\ \mathrm{K} \\ 0 & \text{otherwise} \end{cases} \tag{2.7}$$

$$\Gamma = 2 \times 10^{-26}\ \mathrm{erg\ s^{-1}} \tag{2.8}$$

$$\Lambda = 7.3 \times 10^{-21} \exp\left(\frac{-118400}{T + 1500}\right) + 7.9 \times 10^{-27} \exp(-92/T)\ \mathrm{erg\ cm^3\ s^{-1}} \tag{2.9}$$

Here n is number density. Figure 2.2 shows thermal equilibrium curve for the interstellar medium determined by the cooling/heating function (2.7)-(2.9). Two stable branches exist; warm medium (red) and cold neutral medium (blue). In this paper we assume that cooling/heating takes place at temperature range 400 K $< T <$ 20000 K, otherwise we set $\rho\mathcal{L} = 0$ in order for the dense, cold region to be resolved numerically with moderate number of grid points. We neglect thermal conduction.

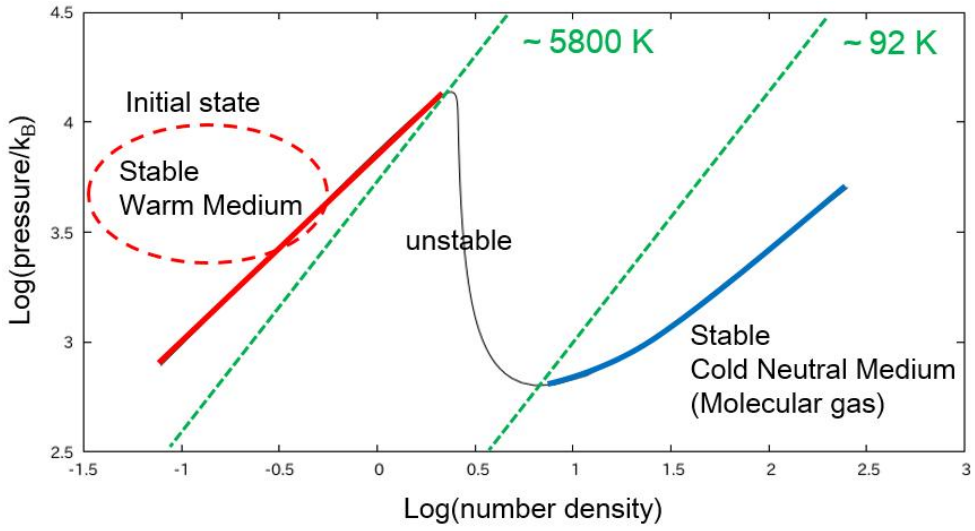

Figure 2.2: Thermal equilibrium curve computed from the cooling/heating function adopted in this paper.

2.3 Numerical Method

The basic equations are solved by applying the HLLD scheme (Miyoshi & Kusano 2005). Second order accuracy in space is preserved by linearly interpolating the values at the cell surface, and restricting them using the minmod limiter. The algorithm of evaluating the numerical flux at the cell surface is given in Appendix A. The solenoidal condition

$\nabla \cdot \boldsymbol{B} = 0$ is satisfied by applying the generalized Lagrange multiplier (GLM) scheme proposed by Dedner et al. (2002). The cooling/heating term is included by time-implicit method. This simulation code has been applied to MHD simulations of the interaction of jets with interstellar gas (Asahina et al. 2014). The size of the simulation box is -200 pc $< x <$ 200 pc, and 5 pc $< z <$ 2400 pc. The grid size is uniform with $\Delta x = 1$ pc and $\Delta z = 0.5$ pc.

2.4 Initial and Boundary Conditions

We assume gravitationally stratified layer in hydrostatic equilibrium. Initial magnetic field is assumed to be force-free and given by

$$B_x = -\Big(\frac{2L_a}{\pi H_m}\Big) B_a \cos\Big(\frac{\pi}{2L_a}x\Big) \exp\Big(-\frac{z}{H_m}\Big) \tag{2.10}$$

$$B_y = \sqrt{1-\Big(\frac{2L_a}{\pi H_m}\Big)^2}\, B_a \cos\Big(\frac{\pi}{2L_a}x\Big) \exp\Big(-\frac{z}{H_m}\Big) \tag{2.11}$$

$$B_z = B_a \sin\Big(\frac{\pi}{2L_a}x\Big) \exp\Big(-\frac{z}{H_m}\Big) \tag{2.12}$$

Initial distribution of density and magnetic filed are shown in Figure 2.3. We set $\rho(z$ = 5 pc) = 2.8 $\times$ 10^{-24} g/cm^3 and $P(z$ = 5 pc) = 1.56 $\times$ 10^{-12} dyn/cm^2 ($T(z$ = 5 pc) = 6700 K). Here $H_{\rm m}$ = 200 pc and L_a = 200 pc denote magnetic scale height and half length of magnetic arch, respectively. We assume strong magnetic field to sustain the dense filaments. The plasma β ($= P_{\rm gas}/P_{\rm mag}$) is assumed to be $\beta = 0.2$ at bottom of the simulation area (B_a = 1.54 x 10^{-5} G). The warm gas with temperature 6700$\sim$20000 K is assumed to satisfy mechanical equilibrium and thermal equilibrium before converge and shear motions are imposed. In region where $z >$ 900 pc, we assume the hot corona with $T_{\rm corona} = 2 \times 10^6$ K.

Boundary conditions in x-direction are symmetric for ρ, P, B_z, v_z and anti-symmetric for B_x, B_y, v_x, v_y. Absorption boundary conditions are applied at the upper boundary. At the lower boundary, density and pressure are fixed to the initial value. Converge (v_x) and shear (v_y) motions are imposed at foot points of the magnetic arcade as follows :

$$v_x = v_y = \begin{cases} -v_0 \dfrac{x}{L_a/4} & 0 \le x < L_a/4 \\ -v_0 \dfrac{L_a - x}{3L_a/4} & L_a/4 \le x \le L_a \end{cases} \tag{2.13}$$

$$v_z = 0 \tag{2.14}$$

Here v_0 is 4 km/s

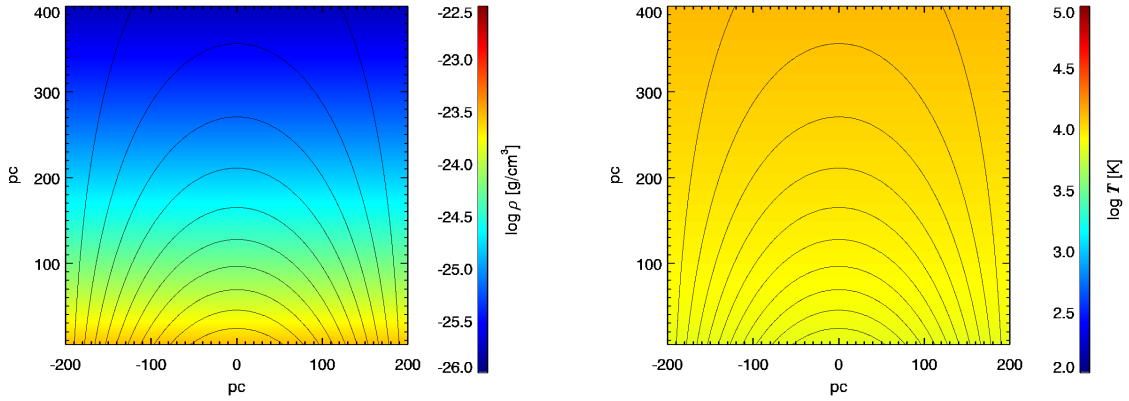

Figure 2.3: Initial distribution of density (left), temperature (right) and magnetic field lines (solid curves) in $x - z$ plane.

2.5 Numerical Results

2.5.1 Formation of a Dense Filament

Figure 2.4 shows density and temperature distribution in $x - z$ plane at $t = 30$ Myrs, 40 Myrs and 120 Myrs. The arcade field squeezed by the converge motion and stretched by the shear motion forms a current sheet around $x = 0$ inside the arcade. Magnetic reconnection taking place in the current sheet creates rising flux ropes. In this simulation, the flux rope is lifted up to ∼250 pc. Since the warm interstellar gas slides down along the closed magnetic field lines, the density around the bottom of the flux rope exceeds the threshold for the onset of the cooling instability. Thermal instability taking place in the dense region forms cold, dense filaments. Density of the filament becomes 10-100 times that of the initial state. The dense filament is lifted up to 100-200 pc and sustained for 100 Myrs. The length and thickness of the filament at $t = 120$ Myrs are ∼60 pc in vertical direction and 6-8 pc in x-direction, respectively.

Figure 2.5 enlarges the region where dense filaments are formed. Arrows show velocity vectors. The warm gas infalls along the magnetic field lines. The speed of the warm gas accumulating toward the filament is about 2 km/s. Figure 2.6 shows the distribution of B_y at $t = 120$ Myrs. Since B_y is amplified by shear motion, B_y becomes strong inside the magnetic flux rope. The flux rope corresponds to the blue-purple region in Figure

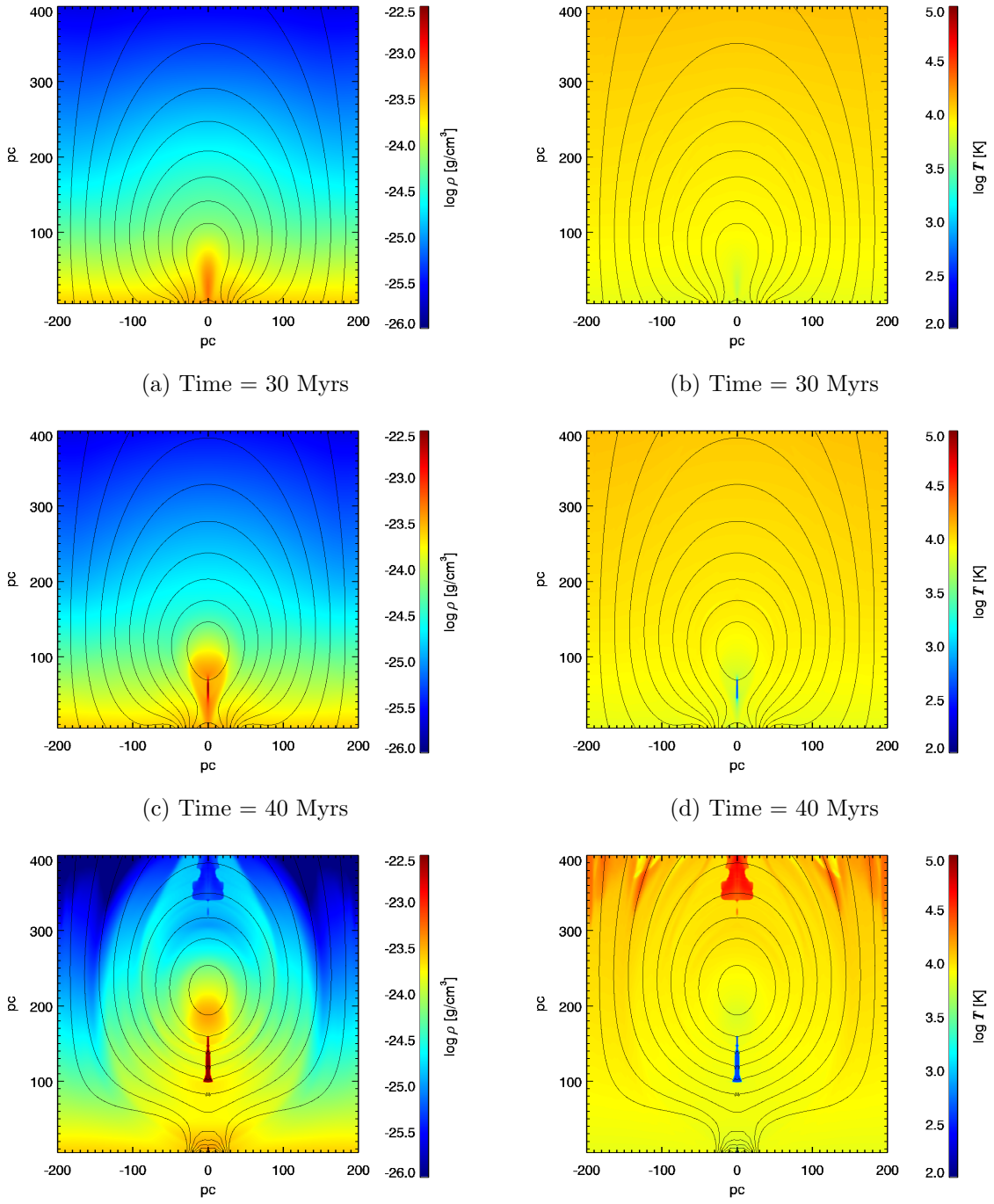

(a) Time = 30 Myrs

(b) Time = 30 Myrs

(c) Time = 40 Myrs

(d) Time = 40 Myrs

(e) Time = 120 Myrs

(f) Time = 120 Myrs

Figure 2.4: Density (left panels), temperature (right panels) distribution and magnetic field lines (solid lines) in $x - z$ plane at 30 Myrs (top), 40 Myrs (middle) and 120 Myrs (bottom).

2.6 where $B_y > 5.5$ μG. Magnetic field lines inside the flux rope have helical shape as schematically shown in figure 2.1(b). Red dots in figure 2.7 show the pressure and number density at each grid point. At the initial state (figure 2.7(left)), warm gas locates

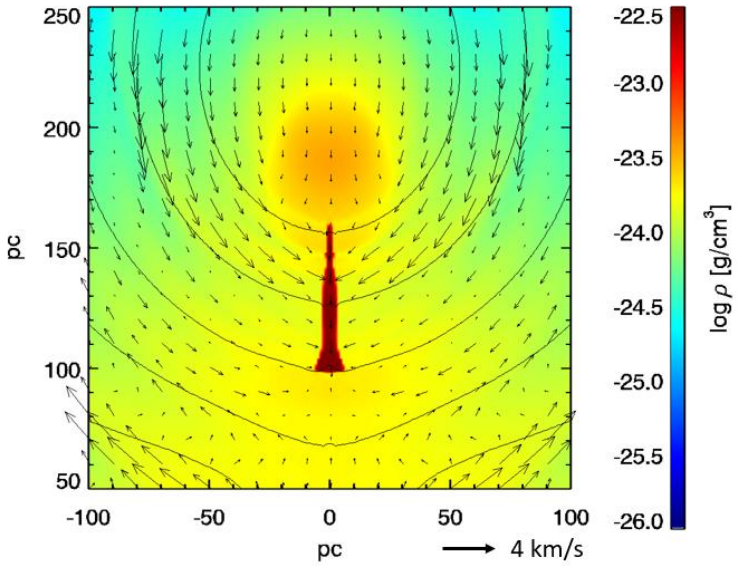

Figure 2.5: Density distribution (color), magnetic field lines (solid line) and velocities (arrows).

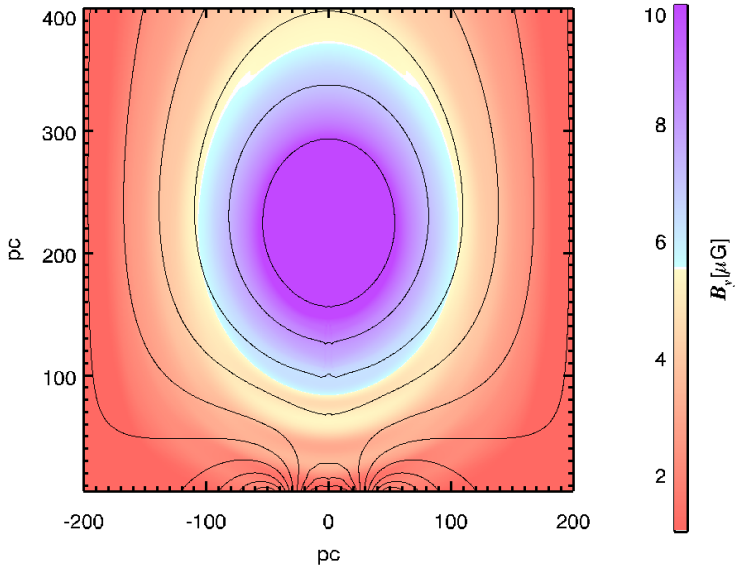

Figure 2.6: Distribution of B_y and magnetic field lines (solid line).

on the thermal equilibrium curve (solid line). Dashed line shows the isothermal line at $T = 400$ K and the dash-dotted line shows that at $T = 20000$ K. Figure 2.7(right) plots pressure P and number density n at $t = 120$ Myrs. Since the warm gas infalling along the closed magnetic field lines compresses the gas around the bottom of the flux rope ($x = 0$ pc), the number density exceeds the threshold for the cooling instability, and deviates from the warm gas branch. The dense, cool gas is transformed to the cold neutral medium

(CNM) where temperature is less than 400 K. Since we cut off cooling when $T < 400$ K to numerically resolve the filament, the CNM locates at the isothermal line at $T = 400$ K. Figure 2.8 shows time evolution of density, pressure and temperature at $x = 0$

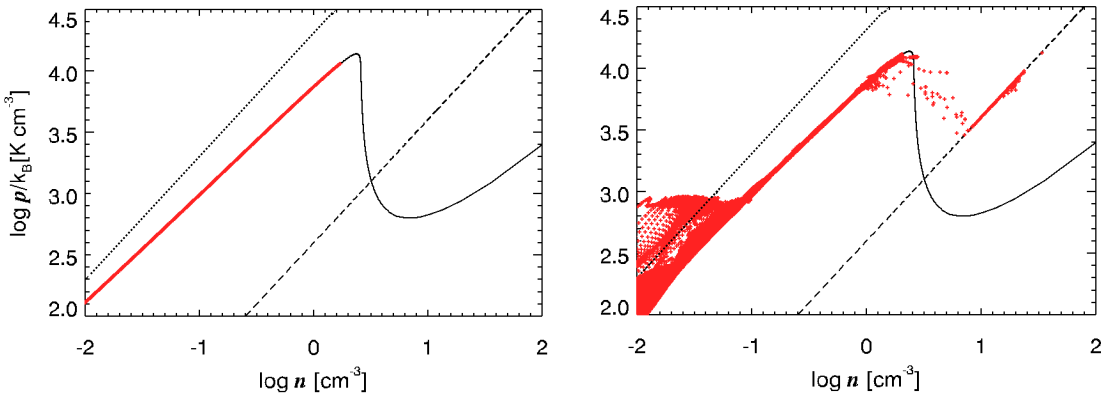

Figure 2.7: Pressure and number density at $t = 0$ Myr (left panel) and 120 Myrs (right panel). Solid curve shows the thermal equilibrium curve. The dashed curve shows the isothermal line at $T = 400$ K and the dotted curve shows that at $T = 20000$ K.

pc and $z = 105$ pc. The initially warm gas ($T \sim 10^4$ K) is compressed during $t = 30$-50 Myrs. Consequently, density and pressure increase and temperature slightly decreases. At $t = 50$ Myrs, the gas locates in the thermally unstable region in the P-n diagram. Figure 2.8 shows that pressure and temperature decrease due to the cooling instability and the density continues to increase. Finally, cool ($T = 400$ K), dense filament is formed. Figure 2.9 shows vertical distribution of temperature at $x = 0$ pc at 120 Myrs. The dense filament locates at $z = 100$-160 pc. Meanwhile, high temperature ($T = 35000$K-70000K) region appears at $z = 330$-450 pc. The hot region is formed by shock waves formed by the upward flow. When the temperature of the shocked gas exceeds 20000 K, the region stays in high temperature state. Figure 2.10 shows column density of the dense gas ($T <$ 500 K), the unstable neutral medium (UNM) in the temperature range 500 K $< T <$ 5000 K and the warm gas in the temperature range 5000 K $< T <$ 7000 K, at 120 Myrs for line of sight direction parallel to the x-axis. Column density of the dense filament is $\sim 1.0 \times 10^{-3}$ g cm^{-2} (column number density $= 6 \times 10^{20}$ cm^{-2}) around the bottom of

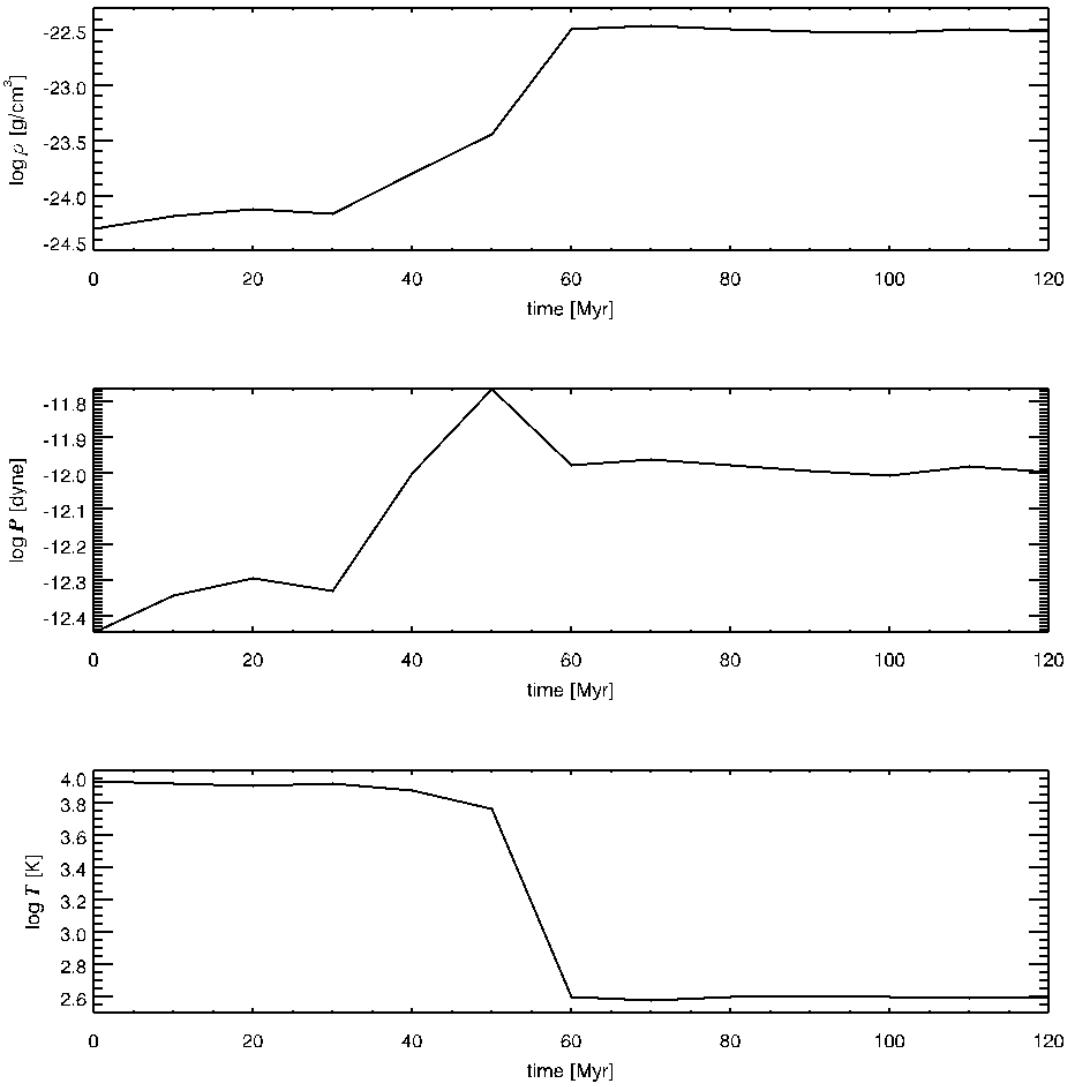

Figure 2.8: Time evolution of density (top), pressure (middle) and temperature (bottom) at $x = 0$ pc and $z = 105$ pc.

the dense filament. The column density of the unstable neutral medium is at largest 1.0 $\times$ 10^{-4} g cm^{-2} (column number density = 6 $\times$ 10^{19} cm^{-2}). The column density of the warm gas is 3 $\times$ 10^{-4} g cm^{-2} above the top of the dense filament. The dense gas can be observed by CO emission and the UNM and the warm gas can be observed by 21cm line emission by neutral hydrogen. Torii et al. (2010b) compared the distribution of CO emission and HI emission and found that they coincide in loop 1. In our simulation, the distribution of the UNM coincides with the dense filament but the warm gas above the dense filament has column density comparable to the dense filament.

The column density estimated from the CO emission is 3 $\times$ 10^{21} cm^{-2} around the top

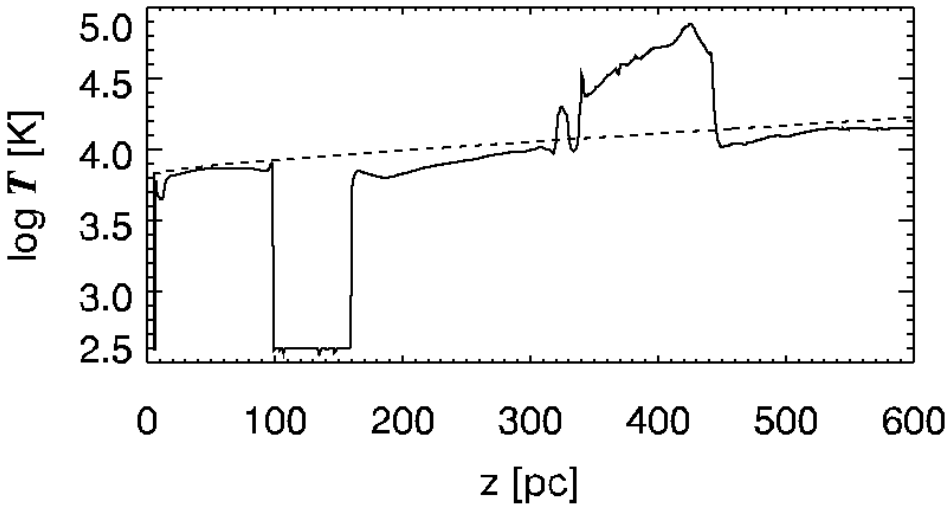

Figure 2.9: Vertical distribution of temperature at $x = 0$ pc at 120 Myrs (solid line) and initial temperature profile (dashed line).

of the loop 1 and the HI column number density of loop 1 obtained from the 21cm line emission is 6×10^{20} cm^{-2} (Torii et al. 2010b). These column densities are 5 times larger than that of our simulation, and will be discussed in the next subsection.

2.5.2 Mass Estimation of Dense Filaments

In this subsection, we would like to estimate the mass levitated in the cold, dense filament and compare the numerical results with observations. NANTEN observations indicate that the projected lengths of two loops (loop 1 and loop 2) are ∼500 pc and ∼300 pc, respectively, They are lifted up to ∼220 pc and ∼300 pc and the total mass of one loop was estimated to be 8×10^4 M$_\odot$ (Fukui et al. 2006). If we take average value of projected lengths of two loops and assume that the shape of loops are a half circle, the average length of the loop is 400 pc $\times$ $\pi/2$, $\sim$ 600 pc. In our simulation results at 120 Myrs, dense filament ($T < 500$ K) is lifted up to 100∼200 pc. The mass of the filament can be estimated to be 112 M$_\odot$ times the length of the loop in y-direction in unit of pc. In other words, the total mass of the dense filament is 7×10^4 M$_\odot$ if we assume the length of the filament in y-direction is 600 pc.

The total mass of the dense filament in the simulation is consistent with the lower

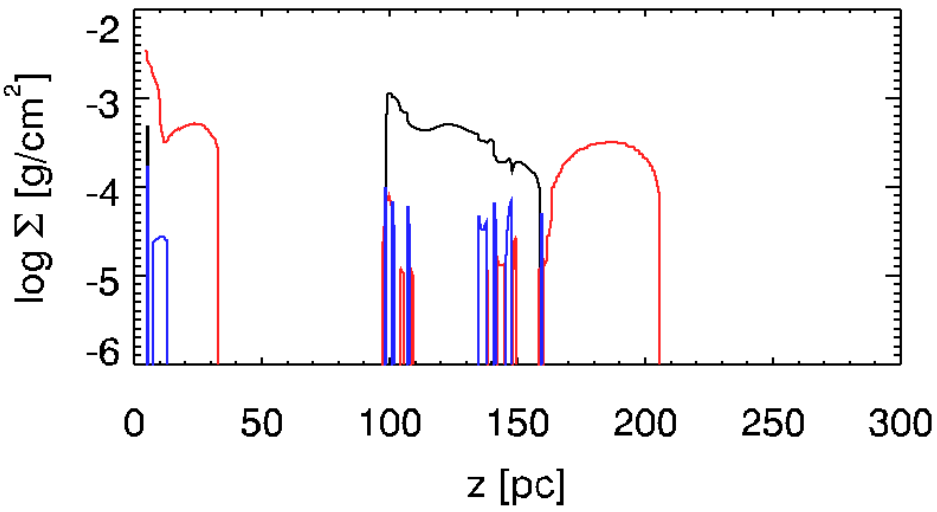

Figure 2.10: Vertical distribution of column density of the dense gas ($T < 500$ K) with black line and the unstable neutral gas (500 K $< T <$ 5000 K) and warm gas (5000 K $< T <$ 7000 K) with blue and red curves, respectively. The line of sight direction is parallel to the x-axis.

limit of the mass estimated from observation. However, Torii et al. (2010b) estimated by detailed analysis of the NANTEN ^{12}CO and ^{13}CO(J = 1-0) observations that the total mass of these two loops are 1.4 $\times$ 10^6 M$_\odot$ and 1.9 $\times$ 10^6 M$_\odot$, respectively. These values are an order of magnitude larger than those of our simulation.

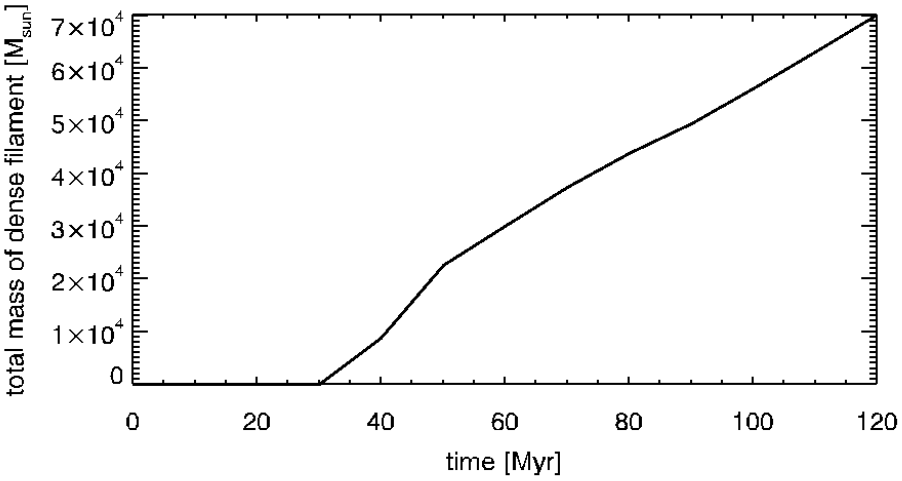

Figure 2.11: Time evolution of total mass of a dense filament.

Here we would like to point out that the mass of the dense filament increases with time. Figure 2.11 shows the time evolution of the total mass of the dense filament. As we have shown in Figure 2.5, warm gas in the magnetic flux rope continuously fall down towards the filament along magnetic field lines. The maximum mass of the filament can be estimated by assuming that all the gas inside the flux rope fall into the filament. The mass inside the flux rope corresponding to the blue-purple region in Figure 2.6 is 3.5×10^5 $M_\odot$ assuming that the depth in y-direction is 600 pc.

Chapter 3

Prominence Formation in Rotating Disks

The simulations we presented in section 2.5, neglects the disk's rotation. However, the Galactic rotation is not negligible in Galactic central region because the rotation time scale $t_{\rm rot} = 2\pi/\Omega$, where the angular speed of rotation $\Omega = 8 \times 10^{-15}$ s^{-1} (approximately 240 km s^{-1} at $R = 1$ kpc) is 30 Myr. which is comparable with the time scale of the prominence formation. In this chapter we present the results of two-dimensional MHD simulations of prominence formation in rotating disks.

3.1 Magnetohydrodynamics of Rotating Disks

Figure 3.1 shows the rotation curve of our galaxy (Clemens 1985). The rotational speed increases linearly when radius is between 0 and 0.6 kpc. However, it decreases between 0.6 and 2.7 kpc and is $\sim$ 220 km s^{-1} at around the radius of our sun.

When a weakly magnetized disk is rotating differentially, magnetorotational instability grows (MRI) (Balbus and Hawley 1991). MRI amplifies the magnetic fields of the disk and drives magnetic turbulence in time scale of several rotations (e.g., Hawley et al. 1995). Global three-dimensional simulations of the galactic gas disks have revealed that the mean azimuthal magnetic fields are reversed quasi-periodically in a time scale of 10 disk rotation periods (Nishikori et al. 2006, Machida et al. 2013). This cyclic dynamo is driven by MRI and the buoyant rise of magnetic fields that is caused due to Parker instability. The magnetic loops formed by the MRI-Parker dynamo can be twisted by

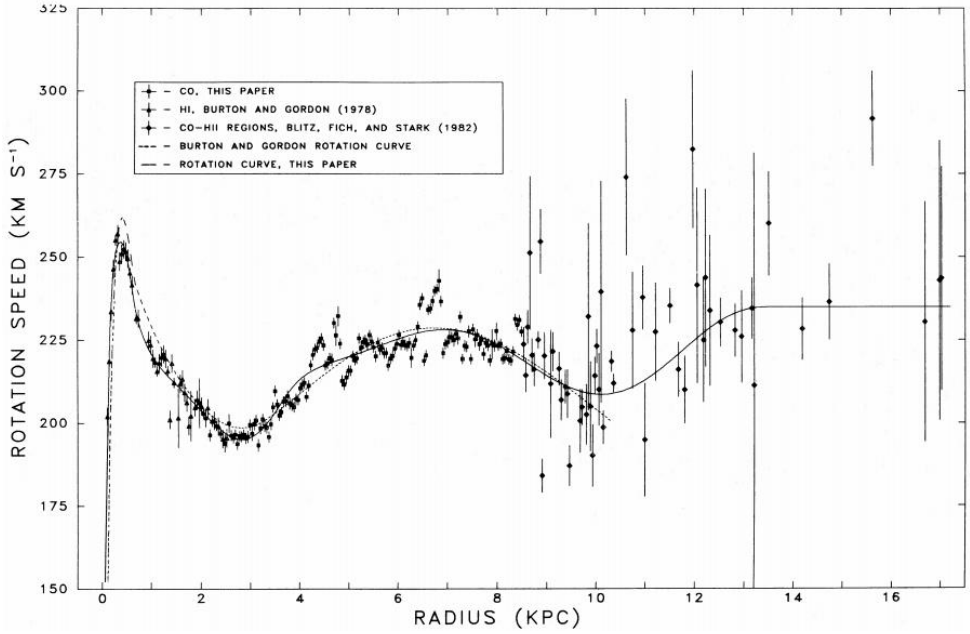

Figure 3.1: Rotation curve of our galaxy measured by CO and HI observations. (Credit: Clemens, D. P., Massachusetts-Stony Brook Galactic plane CO survey - The Galactic disk rotation curve, ApJ, Vol. 295, p. 422-436, 1985 Aug 15. https://doi.org/10.1086/163386 © AAS. Reproduced with permission.)

differential rotation and can be inflated.

Here, we consider a local region of the disk and neglect the differential rotation for simplicity. We investigate the evolution of magnetic loops in a frame that co-rotates with the disk with angular speed of Ω. Since this is a rotating frame, we have to consider the effect of Coriolis force. The turbulent motion of the disk is simulated by introducing motions of the foootpints of magnetic loops.

3.2 Effects of the Coriolis Force on Magnetic Loops

The importance of the Coriolis force is often parameterized using the Rossby number (ratio of the inertial and Coriolis forces) $Ro = U/(\Omega L)$, where U and L are the characteristic speed and the characteristic length, respectively. In galactic gas disks, $U = 10$ km s^{-1}, $L = 100$ pc, and $\Omega = 8{\times}10^{-15}$ rad s^{-1}; therefore $Ro \sim 0.5$. In solar corona, in which $U = 100$ km s^{-1}, $L = 10^5$ km, and $\Omega = 2{\times}\ 10^{-6}$ rad s^{-1}, $Ro = 500$, which further indicates that the Sun rotates much more slowly than the galactic gas disks. This is the reason why the Coriolis force is often ignored in simulations of solar prominence

formation. However, the Coriolis force is not negligible in galactic gas disks.

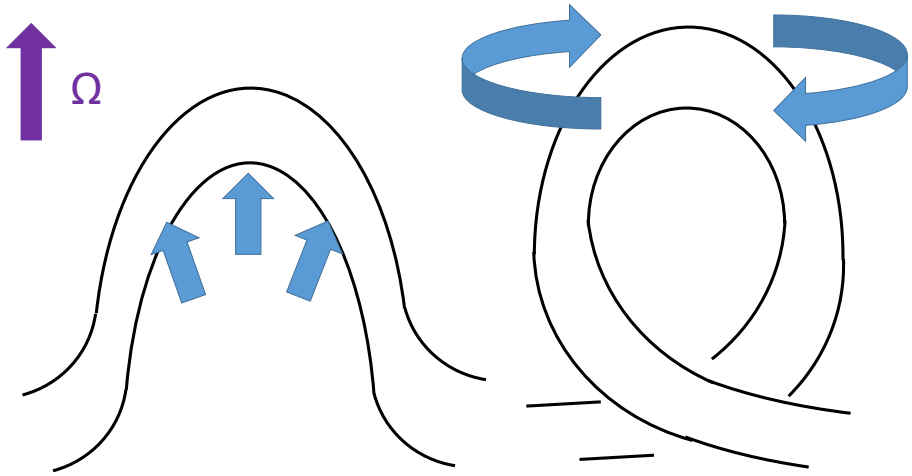

Figure 3.2: Schematic picture of expanding magnetic loops in rotating coordinates.

The effects of the Coriolis force on magnetic loops have been discussed in the context of galactic dynamos. Figure 3.2 depicts that the rising magnetic loops are twisted by a Coriolis force $2\rho\boldsymbol{v} \times \boldsymbol{\Omega}$, which generates a poloidal field from the toroidal field. This can be the origin of the α effect in $\alpha - \Omega$ dynamo theory (e.g., Parker 1970).

Chou et al. (1997) performed a linear analysis of the Parker instability in a co-rotating frame, which indicated that rotation reduces the growth rate of the instability. Nonlinear simulations of the Parker instability by considering the Coriolis force were performed by Chou et al. (1997) and Hanasz et al. (2002). The latter showed that magnetic loops twisted by the Coriolis force undergo magnetic reconnection.

In the succeeding sections, we present the results of the two-dimensional MHD simulations of prominence formation that considering the Coriolis force.

3.3 Basic Equations and Simulation Model

The equations of motion in a frame rotating with angular velocity $\boldsymbol{\Omega}$ are

$$\frac{\partial(\rho\boldsymbol{v})}{\partial t} + \nabla\cdot(\rho\boldsymbol{v}\boldsymbol{v}) = -\nabla P - \rho\boldsymbol{g} + \frac{(\nabla\times\boldsymbol{B})\times\boldsymbol{B}}{4\pi} + 2\rho\boldsymbol{v}\times\boldsymbol{\Omega} + \rho\boldsymbol{r}\times(\boldsymbol{r}\times\boldsymbol{\Omega}) \tag{3.1}$$

Here, we use a local Cartesian coordinate system where the galactic plane lies in the $x-y$ plane, and the z-direction is parallel to $\boldsymbol{\Omega} = (0, 0, \Omega)$ and $\Omega = 8\times10^{-15}$ s^{-1}. Initially we

assume that the magnetic fields satisfy the force-free condition $(\nabla \times \boldsymbol{B}) \times \boldsymbol{B} = 0$ and that the disk is static ($\boldsymbol{v} = 0$) in the co-rotating frame. We further assume that the horizontal components of gravity are balanced by the centrifugal force. In the vertical direction, we assume that there is hydrostatic balance, i.e.

$$\frac{dp}{dz} = -\rho g_z \tag{3.2}$$

where g_z is the gravitational acceleration in the vertical direction and is assumed to be $g_z = 3 \times 10^{-9}$ cm s^{-2}. Assuming the same temperature distribution as that we presented in section 2.4, we can obtain the distribution of ρ and P. The unperturbed force-free magnetic fields are

$$B_x = -\Big(\frac{2L_a}{\pi H_m}\Big) B_a \cos\Big(\frac{\pi}{2L_a}x\Big) \exp\Big(-\frac{z}{H_m}\Big), \tag{3.3}$$

$$B_y = \sqrt{1 - \Big(\frac{2L_a}{\pi H_m}\Big)^2}\, B_a \cos\Big(\frac{\pi}{2L_a}x\Big) \exp\Big(-\frac{z}{H_m}\Big), \tag{3.4}$$

$$B_z = B_a \sin\Big(\frac{\pi}{2L_a}x\Big) \exp\Big(-\frac{z}{H_m}\Big), \tag{3.5}$$

where $L_a = 200$ pc and $H_m = 200$ pc. The anomalous resistivity η is assumed to depend on the current density $J = c\nabla \times \boldsymbol{B}/4\pi$ (see Kaneko & Yokoyama 2015), as follows:

$$\eta = \begin{cases} 0 & J < J_c \\ \eta_0 (J/J_c - 1)^2 & 2J_c > J \geq J_c \\ \eta_0 & J \geq 2J_c \end{cases} \tag{3.6}$$

Here $\eta_0 = 6 \times 10^{23}$ cm^2 s^{-1} and $J_c = 4.0 \times 10^{-16}$ dyn$^{1/2}$ cm s^{-1}. The magnetic Reynolds number defined by $R_m = (c_s\ L_a)/\eta_0 = 1000$, where c_s is the speed of sound ($\sim 10^6$ cm/s when $T = 10000$ K). The critical current density J_c is defined by $J_c = \mathrm{c}B_0/(4\pi R_c)$ where $B_0 = 15$ μG and $R_c = 30$ pc. We assumed translational symmetry in the y-direction and performed two-dimensional simulations in the $x-z$ plane using a simulation box covering -212 pc $< x <$ 212 pc and 5 pc $< z <$ 1353 pc. The mesh sizes are $\Delta x = 0.2$ pc for -10 pc $< x <$ 10 pc and $\Delta z = 0.2$ pc for $z <$ 205 pc. When $|x| >$ 10 pc, Δx was increased by 5 % at each mesh point up to $\Delta x = 2$ pc. Further, when $z >$ 205 pc, Δz was increased by 5 % at each mesh point up to $\Delta z = 2$ pc. The number of mesh points is 366 $\times$ 1606.

To initiate the rising motion of the loop, we imposed a shear motion at the lower

boundary ($z = 5$ pc) by specifying the y- and z-component of velocity as

$$v_y = -v_0 \sin(2\pi x / L_a) \tag{3.7}$$

$$v_z = 0 \tag{3.8}$$

Here v_0 is 4 km s^{-1} for the fiducial model (Model A). Figure 3.3 depicts the distribution

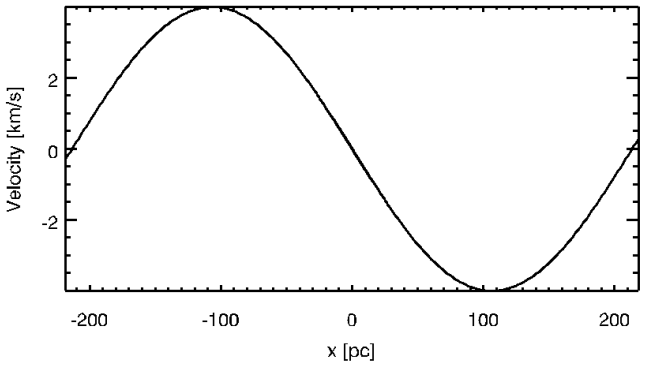

Figure 3.3: Shear motion imposed at the lower boundary.

of v_y at $z = 5$ pc. At the lower boundary, a free boundary condition is applied for v_x and the magnetic field except in the models that imposed the converging flow. The density and pressure are fixed at their initial values. The boundary conditions in the $x-$direction are symmetric for ρ, P, B_z, and v_z and anti-symmetric for B_x, B_y, v_x, and v_y. The absorbing boundary conditions are applied at $z = z_{max}$. We adopted the same heating/cooling function as that of the non-rotating models (equation 2.7-2.9). The MHD equations are solved using the HLLD scheme. Second order spatial accuracy is maintained by applying the MUSCL scheme by linearly interpolating the values at the cell surface and by restricting them using a monotonized central limiter. A third order TVD Runge-Kutta method is used for time integration. The solenoidal condition $\nabla \cdot \boldsymbol{B} = 0$ is approximately satisfied by applying the generalized Lagrange multiplier (GLM), proposed by Dedner et al. (2002). The heating/cooling term is included using time-implicit method.

Table 3.1 shows the parameters used for simulations. Model A is a fiducial model that we assumed a magnetic pressure dominant disk ($\beta = 0.2$). Model A$_c$ applied converging flow at the lower boundary, i.e., $v_x = v_y$ at the lower boundary. Model B is for weaker initial magnetic field. The shear motion is faster in model C. In warm medium ($T = 6000$ K), the sound speed is 8 km s^{-1}; therefore the maximum shear speed in model C equals

Model	β	v_y km s^{-1}	v_x km s^{-1}	Ω s^{-1}	η_0 cm^2 s^{-1}	g_z cm s^{-2}	$\Delta x_{\rm min}$ pc	$\Delta z_{\rm min}$ pc
A	0.2	4	0	8×10^{-15}	6×10^{23}	3×10^{-9}	0.2	0.2
N	0.2	4	0	0	6×10^{23}	3×10^{-9}	0.2	0.2
A_c	0.2	4	4	8×10^{-15}	6×10^{23}	3×10^{-9}	0.2	0.2
B	1.0	4	0	8×10^{-15}	6×10^{23}	3×10^{-9}	0.2	0.2
C	0.2	8	0	8×10^{-15}	6×10^{23}	3×10^{-9}	0.2	0.2
D	0.2	4	0	16×10^{-15}	6×10^{23}	3×10^{-9}	0.2	0.2

Table 3.1: Parameters of different models.

to the sound speed. Finally, higher rotation speed is applied in model D.

3.4 Results for the Fiducial Model (Model A)

This section presents the results for the fiducial model (Model A). Figure 3.4 shows the

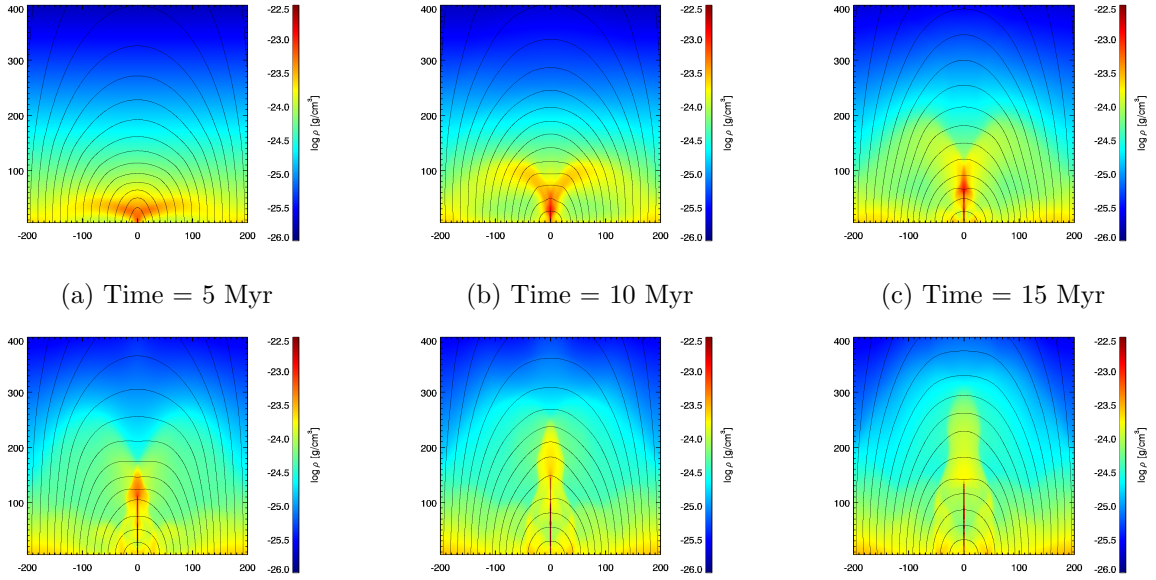

(a) Time = 5 Myr (b) Time = 10 Myr (c) Time = 15 Myr

(d) Time = 20 Myr (e) Time = 25 Myr (f) Time = 30 Myr

Figure 3.4: Evolution of the density in $x-z$ plane for model A (β=0.2) before magnetic reconnection takes place ($t = 0 - 30$ Myr).

early stages of evolution of the sheared magnetic arcade. Since motions in the negative y-direction were imposed at the lower boundary when $x > 0$ and in the positive y-direction when $x < 0$, Alfvén waves propagate along the magnetic field lines. Figure 3.4 (a) shows that the large amplitude Alfvén wave produces both compressible fast magnetosonic wave and slow magnetosonic wave. (See Appendix B for further details about the propagation of Alfvén waves in rotating disks). Figure 3.5 depicts the distribution of $v_{\rm y}$ and ($v_{\rm x}$, $v_{\rm z}$). At $t = 5$ Myr, the propagation speed of the fast magnetosonic wave is approximately 30 km s^{-1}, which indicates that its wavefront is located at around $z = 150$ pc, while that of the slow magnetosonic wave is located around $z = 50$ pc. The propagation of the slow magnetosonic wave generates density enhancements around $z = 50$ pc in figure 3.4(a), and we can further observe the propagation of this dense region along the magnetic loop at $t = 10$ Myr (Figure 3.4(b)). This dense region coincides with a kink with the magnetic field lines, which indicates that the wave has developed into a slow shock wave.

The dense gas that has accumulated around $x = 0$ subsequently begins to cool because the local density has exceeded the threshold for the onset of the cooling instability. This

instability forms a dense, thin, vertical filament near $x = 0$ pc at $t = 20 - 30$ Myr. The thickness of the dense vertical filament is 3 pc. This thickness is determined by the cutoff temperature ($\sim$ 400K) below which the heating/cooling rate is artificially reduced.

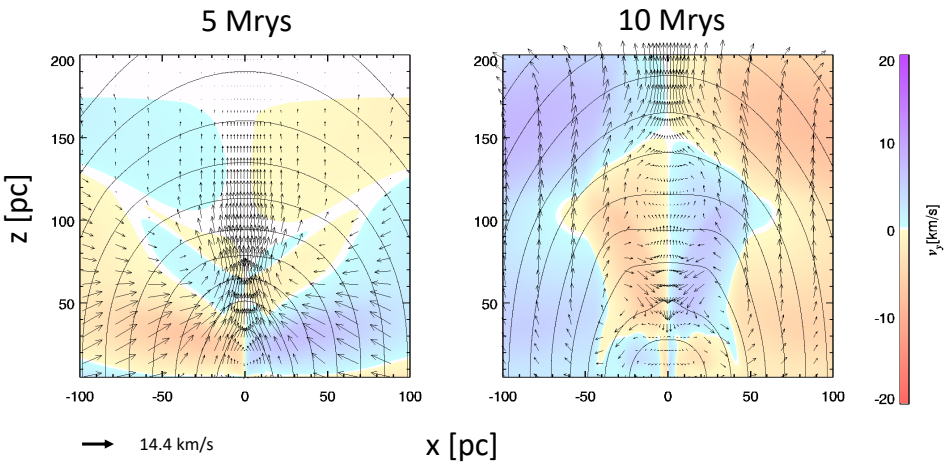

Figure 3.5: Distribution of v_y (color) and v_x, v_z(arrows) for model A.

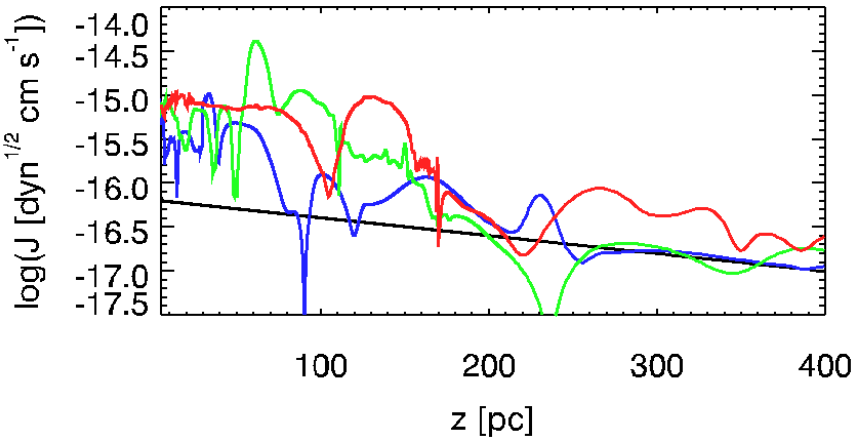

Figure 3.6: Current density distribution along the z-axis at $x = 0$ pc. The curves show distribution at $t = 0$ (black), 10 (blue), 20 (green), 50 (red) Myr.

Figure 3.6 depicts the variations in current density along the z-axis ($x = 0$ pc). It increases at $z \sim 60$ - 100 pc when $t = 20$ Myr because the magnetic tension force supports the dense blob located above this region, against gravity. Since the current density in this region exceeds $J_c = 4.0 \times 10^{-16}$ dyn$^{1/2}$ cm s^{-1} the currents can be dissipated by

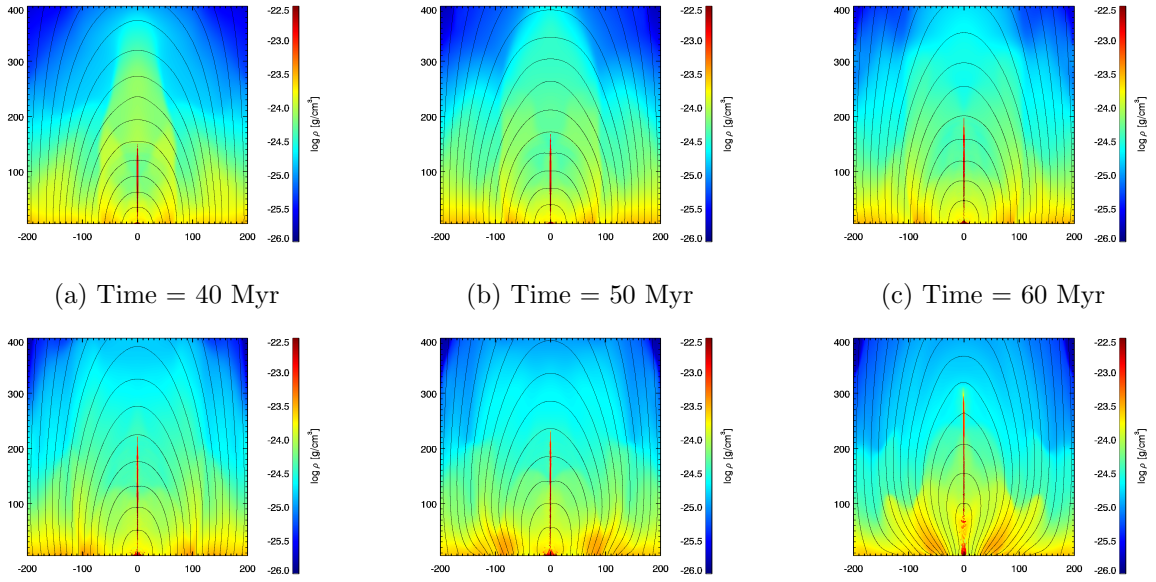

(a) Time = 40 Myr (b) Time = 50 Myr (c) Time = 60 Myr

(d) Time = 70 Myr (e) Time = 80 Myr (f) Time = 90 Myr

Figure 3.7: Evolution of the density in $x - z$ plane for model A (β=0.2) before magnetic reconnection takes place ($t = 40 - 90$ Myr).

resistivity.

Figure 3.7 shows that the magnetic loops and the dense filament are both elongated in vertically because the magnetic pressure is enhanced by foootpoint motion. In contrast to the non-rotating model that is illustrated in Chapter 2, the onset of magnetic reconnection in model A is delayed, which is possibly caused due to the slower converging motion at the lower boundary. Since we do not impose converging motion at the boundary in model A, the deformation of the magnetic loop to "Ω" shape is delayed until converging flow appears at the lower boundary when $t = 70$ Myr.

Figure 3.8 enlarges the region -50 pc $< x <$ 50 pc and 5 pc $< z <$ 100 pc at $t = 90$ Myr during the onset of the magnetic reconnection. The magnetic field lines indicate that the reconnection point is located at $x = 0$ pc and $z = 30$ pc. The dense filament is destroyed near the reconnection point where plasmoid is formed and ejected upward.

Figure 3.9 depicts the variations in density and velocity after the onset of magnetic reconnection. The maximum speed of the reconnection jet, which moves upward is 40 km s^{-1}. The reconnection point moves downward and reaches the lower boundary at $t = 93$ Myr. Subsequently, slow shock wave appears, which indicates the ongoing Petschek-like reconnection.

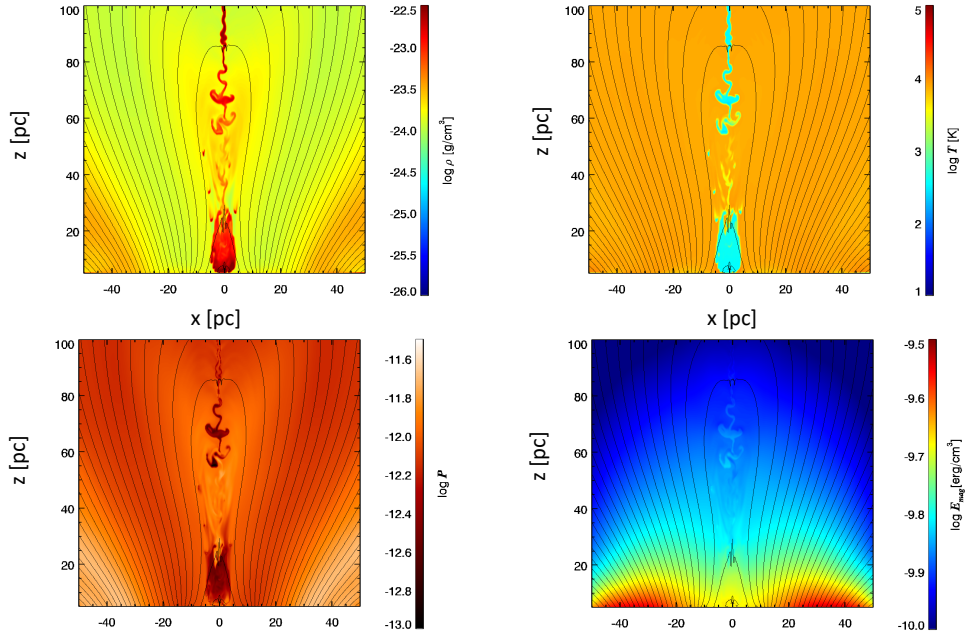

Figure 3.8: Density (left top), temparature (right top), pressure (left bottom) and mgnetic enrgy density (right bottom) at 90 Myrs at the beginning of the magnetic reconnection.

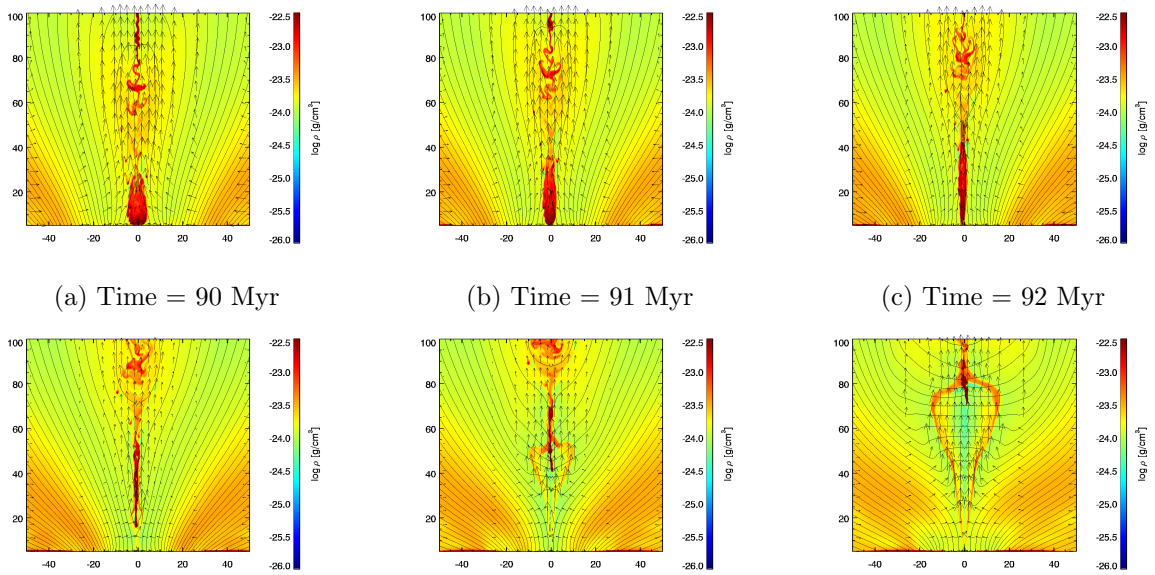

(a) Time = 90 Myr (b) Time = 91 Myr (c) Time = 92 Myr

(d) Time = 93 Myr (e) Time = 94 Myr (f) Time = 95 Myr

Figure 3.9: Density distribution in $x - z$ plane for model A when magnetic reconnection is taking place ($t = 90 - 95$ Mry).

Figure 3.10 depicts the current density distribution along the z-axis at t = 90 - 100 Myr, while the magnetic reconnection is releasing magnetic energy. This is indicates that magnetic reconnection is dissipating the current at z = 30 - 150 pc.

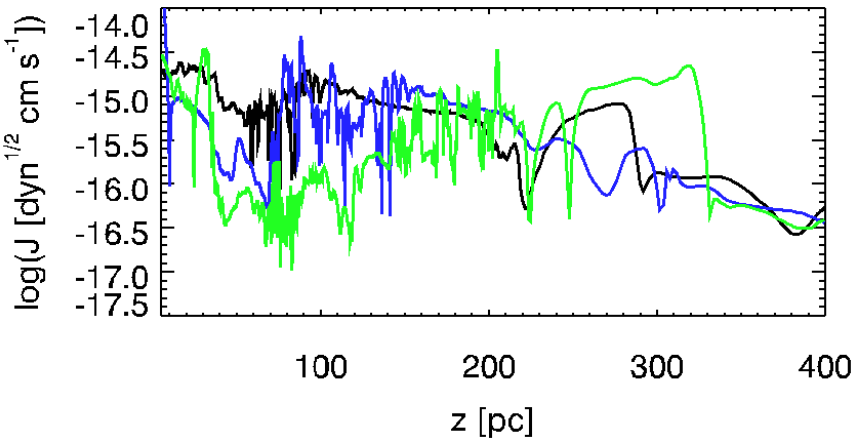

Figure 3.10: Current density distribution at $x = 0$ pc for $t = 90$ (black), 95 (blue), and 100 (green) Myr.

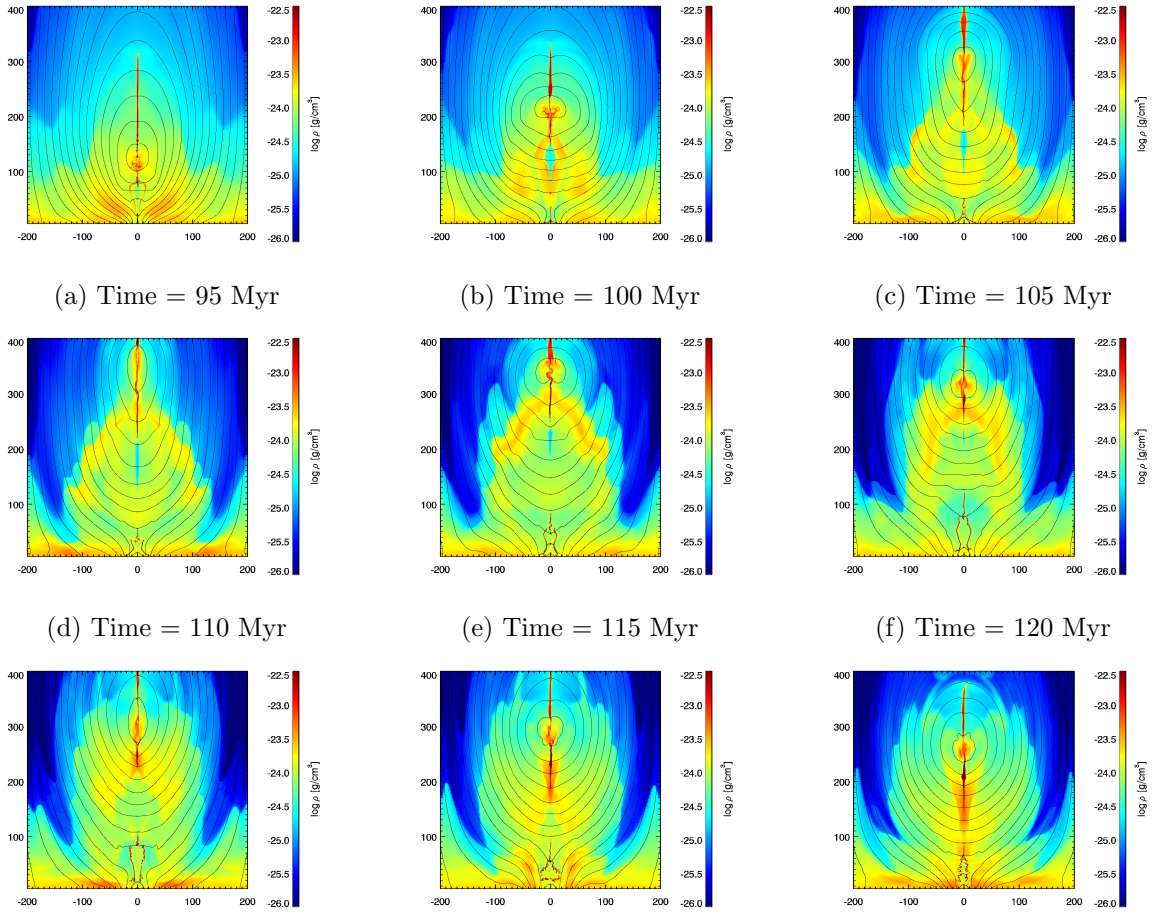

(a) Time = 95 Myr (b) Time = 100 Myr (c) Time = 105 Myr

(d) Time = 110 Myr (e) Time = 115 Myr (f) Time = 120 Myr

(g) Time = 125 Myr (h) Time = 130 Myr (i) Time = 135 Myr

Figure 3.11: Evolution of the density in $x - z$ plane for model A ($t = 95 - 135$ Mrys).

Figure 3.11 shows that the magnetic flux rope (plasmoid) formed by magnetic reconnection is ejected ($t = 95 - 105$ Myr) with the average upward speed at the center of the flux rope ~ 20 km s^{-1}. The rapid outflow generated by the reconnection causes the formation of an evacuated region below the center of the flux rope. The previously elevated cool ($T < 10^3$ K) gas in dense filament then falls back along the magnetic field lines at $t = 110 - 125$ Myrs. A dense region with number density $n > 10$ cm^{-3} is formed around $|x| < 100$ pc, $z = 200 - 300$ pc at $t = 115$ Myrs. The speed of the downflow along the magnetic field lines is ~ 10 km s^{-1}. The warm dense matter accumulates around $x = 0$, $z = 250$ pc at $t = 125$ Myr. Since the density of this region exceeds the threshold for the onset of the thermal instability, cool, dense filament is further formed around the bottom of the magnetic flux rope. The mass of this dense filament increases as the plasma confined in the rope falls along the magnetic field lines and accumulates around the bottom of closed magnetic field lines ($120 - 135$ Myrs).

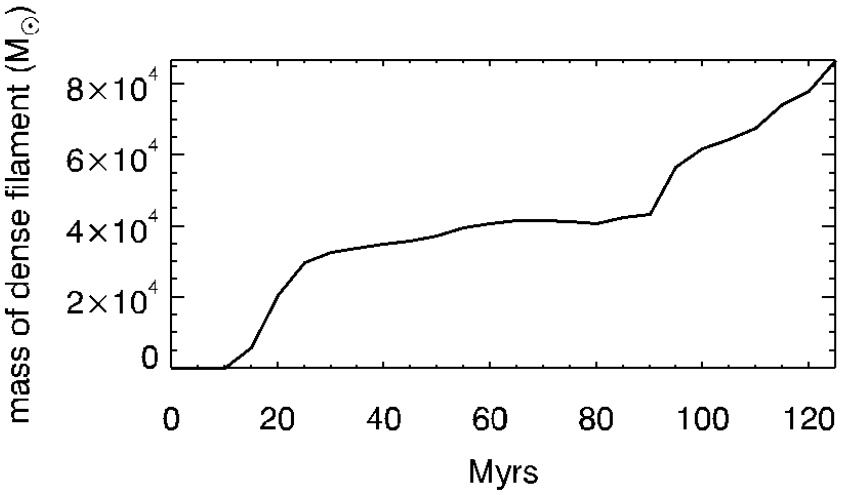

Figure 3.12: Time evolution of dense, cool mass ($T < 500$ K)for model A.

Figure 3.12 shows the time variation of the mass of the cool ($T < 500$ K) filament in the region by at -20 $< x <$ 20 pc and $z > 50$ pc where we have assumed that the length of the filament perpendicular to the $x - z$ plane is 600 pc. The filament (prominence) appears at around $t = 15$ Myr, and its mass is nearly constant until magnetic reconnection occurs at around $t = 90$ Myr. The mass of the filament subsequently increases when $t >$ 100 Myr because the plasma that is confined in the flux rope begins to fall toward the bottom of the closed magnetic field lines. Figure 3.13 illustrates how the disk's gas rises

and forms cool, dense filaments.

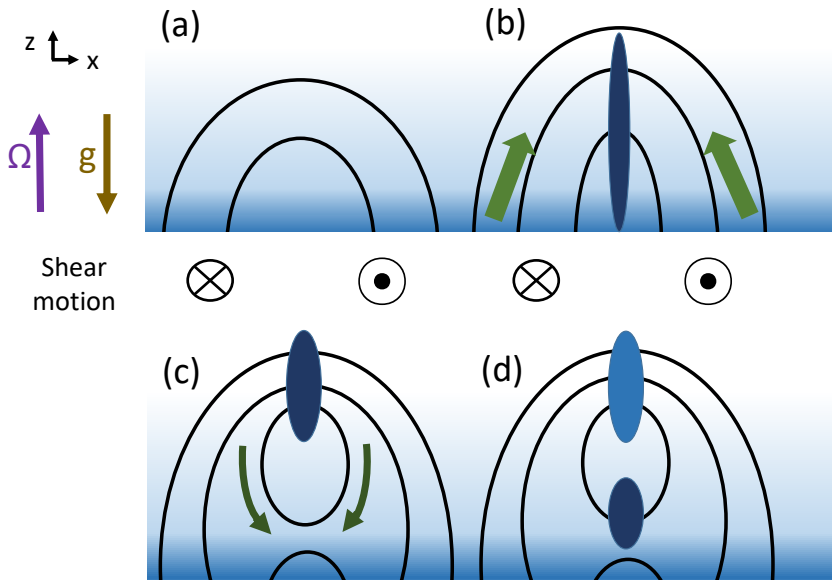

Figure 3.13: Illustration picture of time evolution for Model A.

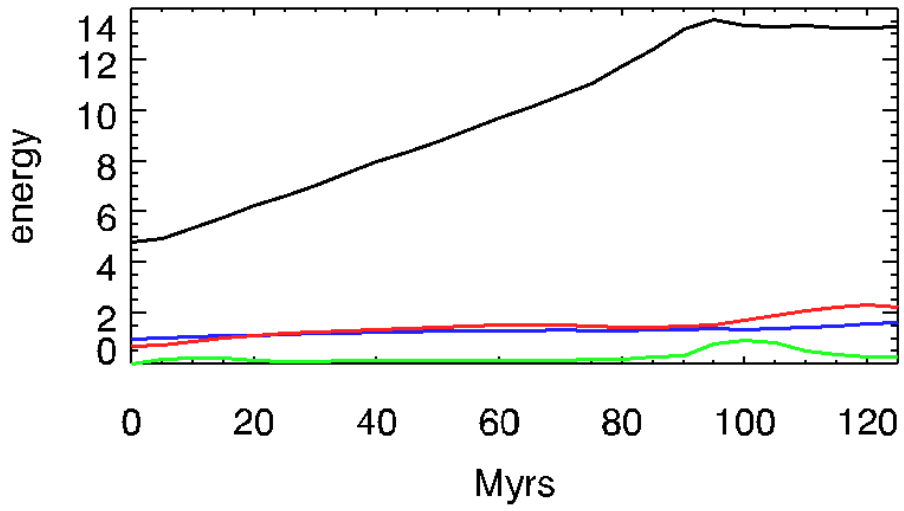

Figure 3.14: Time evolution of the magnetic energy (black), kinetic energy (green), gravitational energy (red) and thermal energy (blue) for model A. The energies are normalized using initial thermal energy for model A.

Figure 3.14 depicts how the energies vary over time for model A with all the energies normalized using the initial thermal energy. The magnetic energy increases almost lin-

early over time up to t ∼90 Myr when magnetic reconnection occurs due to the injection of shear motion at the lower boundary. The Poynting flux injected at the lower boundary per unit area and time is $F_p = (\boldsymbol{v} \times \boldsymbol{B}) \times \boldsymbol{B}/4\pi \sim B^2 v_y/4\pi \sim 10^{-5}$ erg s^{-1} cm^{-2}, which is comparable to $\dfrac{\Delta E_{\rm mag}}{\sigma \Delta t}$ (σ is the area of the lower boundary). After the onset of the magnetic reconnection, the magnetic energy is converted to both kinetic energy and gravitational energy.

The gravitational energy of the observed molecular loops can be estimated as $mgh \sim 10^{52}$ erg. If we assume area of lower boundary is 400 pc times 600 pc, the energy injection rate by the Poynting flux can be estimated to be $\sim 10^{52}$ erg/15 Myr. In this case, to levitate molecular gas to form the the molecular loop, the Poynting flux must be injected at least 15 Myrs.

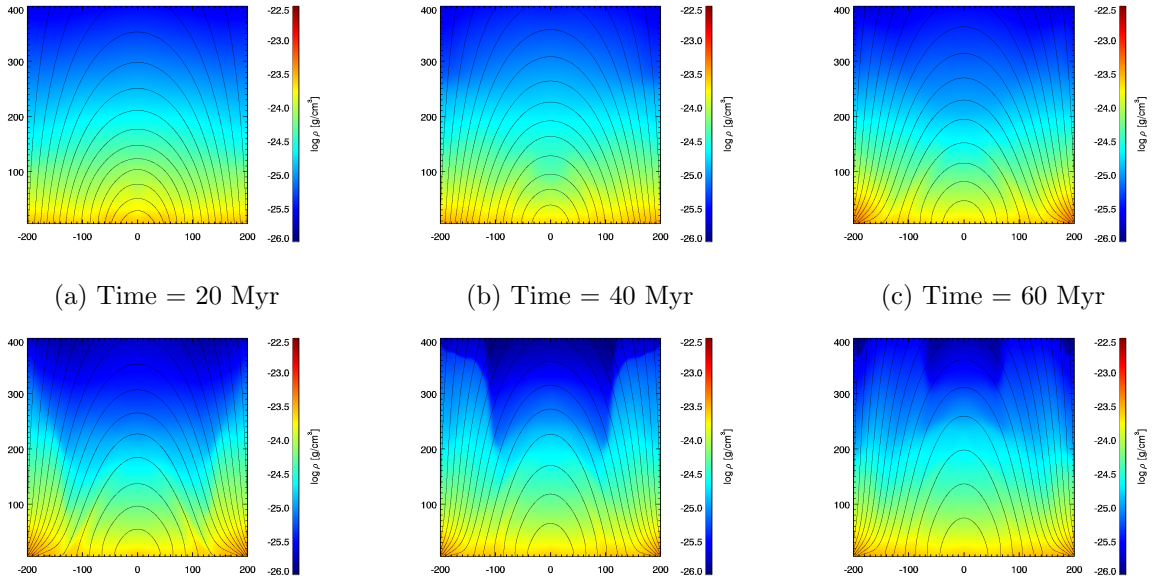

(a) Time = 20 Myr (b) Time = 40 Myr (c) Time = 60 Myr

(d) Time = 80 Myr (e) Time = 100 Myr (f) Time = 120 Myr

Figure 3.15: Evolution of the density in the $x - z$ plane for model N ($t = 20 - 120$ Myr).

Next, we demonstrate the effects of disk rotation. Figure 3.15 shows the evolution of the density and magnetic field lines for model N in which the disk is not rotating ($\Omega = 0$). Figure 3.16 shows the distribution of v_y and v_x, v_z at $t = 5$ and 10 Myr. Although we can still observe the fast and slow magnetosonic waves, the increase in density is much smaller than that observed for model A. In Appendix B, we show that the disk's rotation enhances the increase in density during the propagation of the slow magnetosonic wave. Figure 3.17 depicts the time evolution of the current density along $x = 0$ for model

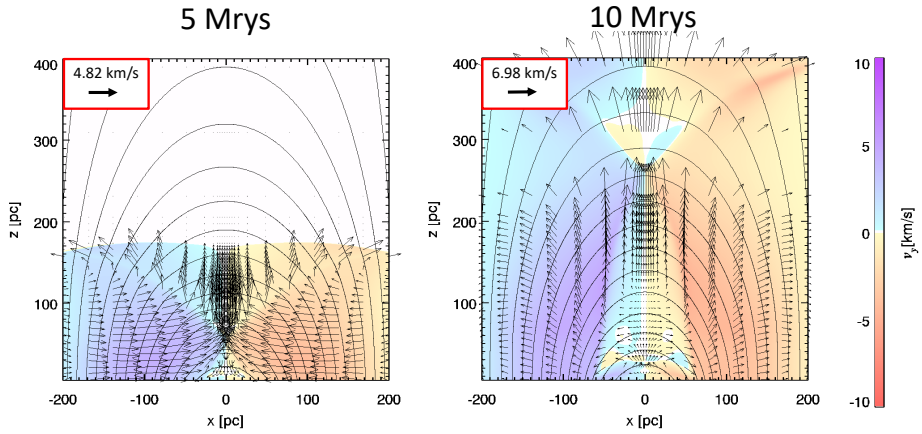

Figure 3.16: Distribution of v_y (color) and v_x, v_z(arrows) for model N.

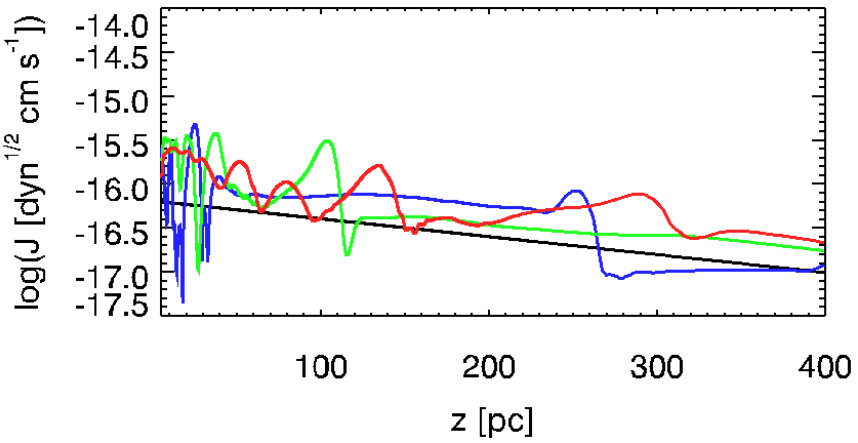

Figure 3.17: Current density distribution at $x = 0$ pc. Curves show distribution at $t = 0$ (black), 10 (blue), 20 (green), 50(red) Myrs of model N.

N. In contrast to model A, the current density is smaller than J_c even in later stages because converging motion is not imposed at the lower boundary (see Chapter 2). Such a converging motion is essential for the formation of dense filaments in non-rotating disks; however, it is not essential for the prominence formation in rotating disks.

3.5 Effects of Converging Motion

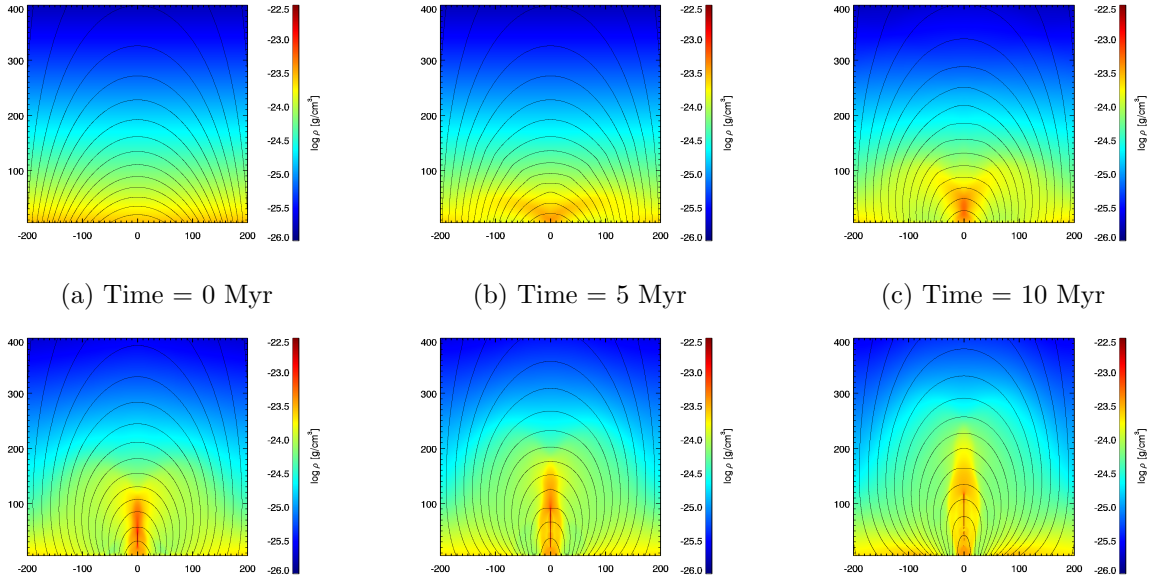

(a) Time = 0 Myr (b) Time = 5 Myr (c) Time = 10 Myr

(d) Time = 15 Myr (e) Time = 20 Myr (f) Time = 25 Myr

Figure 3.18: Evolution of the density in $x - z$ plane for model A_c before the occurrence of magnetic reconnection ($t = 0 - 25$ Myr).

In this section, we discuss the results for model A_c which includes both converging motion and the Coriolis force. Figure 3.18 depicts its density distribution in the $x - z$ plane. During the early stages ($0 - 25$ Myrs), a dense region is formed around the midpoint of the arch ($x = 0$). Due to the occurrence of a cooling instability in this region, dense filament forms at around $x = 0$ and $z = 30$ - 100 pc at $t = 25$ Myr. After the onset of magnetic reconnection, the evolution is observed to be similar to that of the non-rotating model presented in Chapter 2. Figure 3.19 shows that the height of the flux rope in is similar to that observed in the non-rotating model ($\sim$ 200 pc). Magnetic reconnection is triggered earlier ($t \sim 35$ Myr) because the converging motion imposed at the lower boundary deforms the magnetic arcade into a "Ω" shape, which is favourable for magnetic reconnection. The dense filament that is formed in this model is thicker ($\sim$ 10 pc) than the non-rotating model and shows a wavy shape; further, the reason for such behavior are discussed in Appendix C.

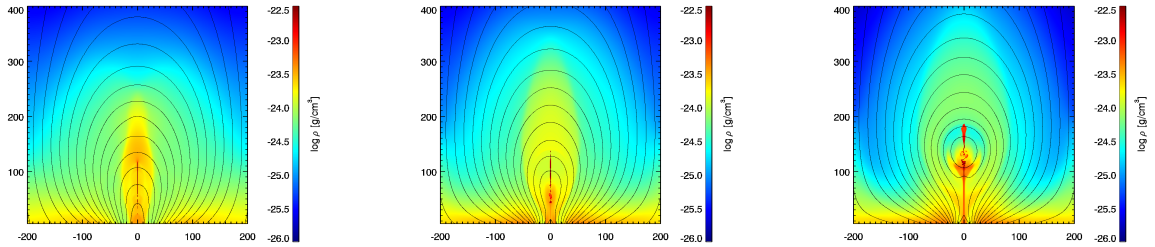

(a) Time = 25 Myr (b) Time = 35 Myr (c) Time = 45 Myr

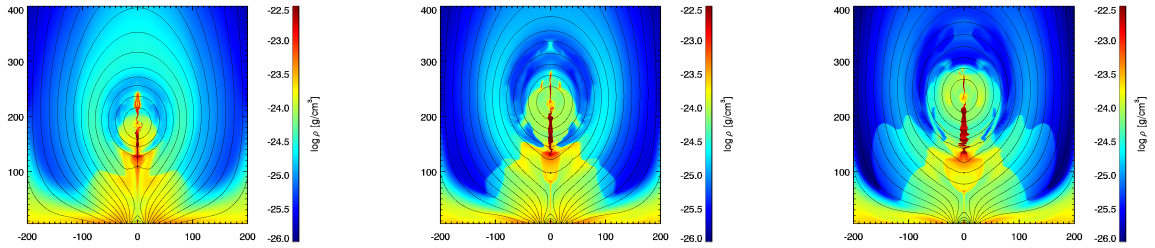

(d) Time = 55 Myr (e) Time = 65 Myr (f) Time = 75 Myr

Figure 3.19: Evolution of the density in $x-z$ plane for model A_c ($t = 25 - 75$ Myr).

3.6 Parameter Dependence

In this section, we investigate the dependence of numerical results on the initial magnetic field strength and imposed shear velocity.

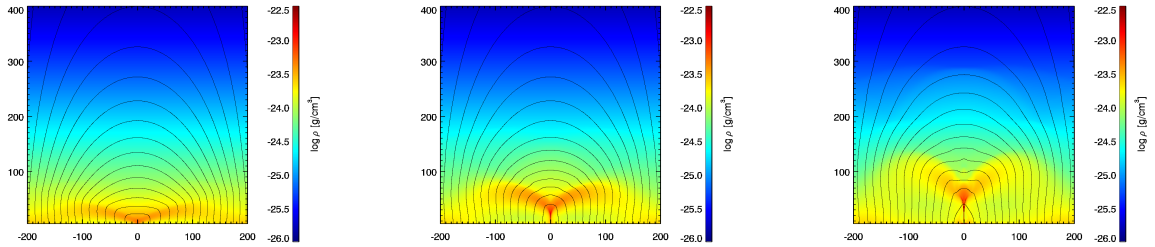

(a) Time = 5 Myr (b) Time = 10 Myr (c) Time = 15 Myr

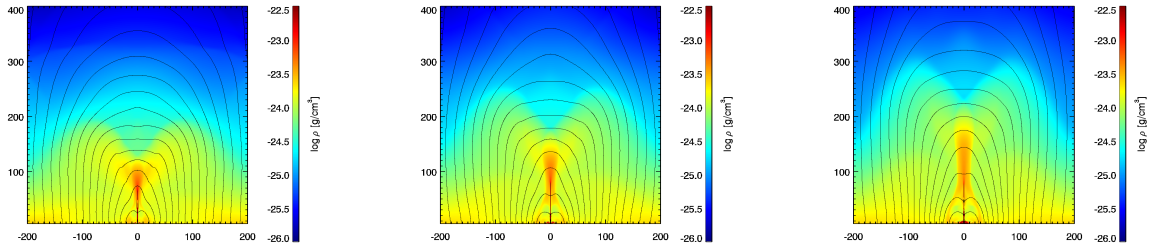

(d) Time = 20 Myr (e) Time = 25 Myr (f) Time = 30 Myr

Figure 3.20: Evolution of the density in $x-z$ plane for model B ($t = 5 - 30$ Mry).

Figure 3.20 depicts the evolution of the density for model B ($\beta = 1.0$). In contrast to

model A ($\beta = 0.2$), the density of the filament formed at $z > 50$ pc is observed to be less than $n = 10$ cm^{-3}. Therefore a cooling instability only occurs at low latitude ($z < 50$ pc).

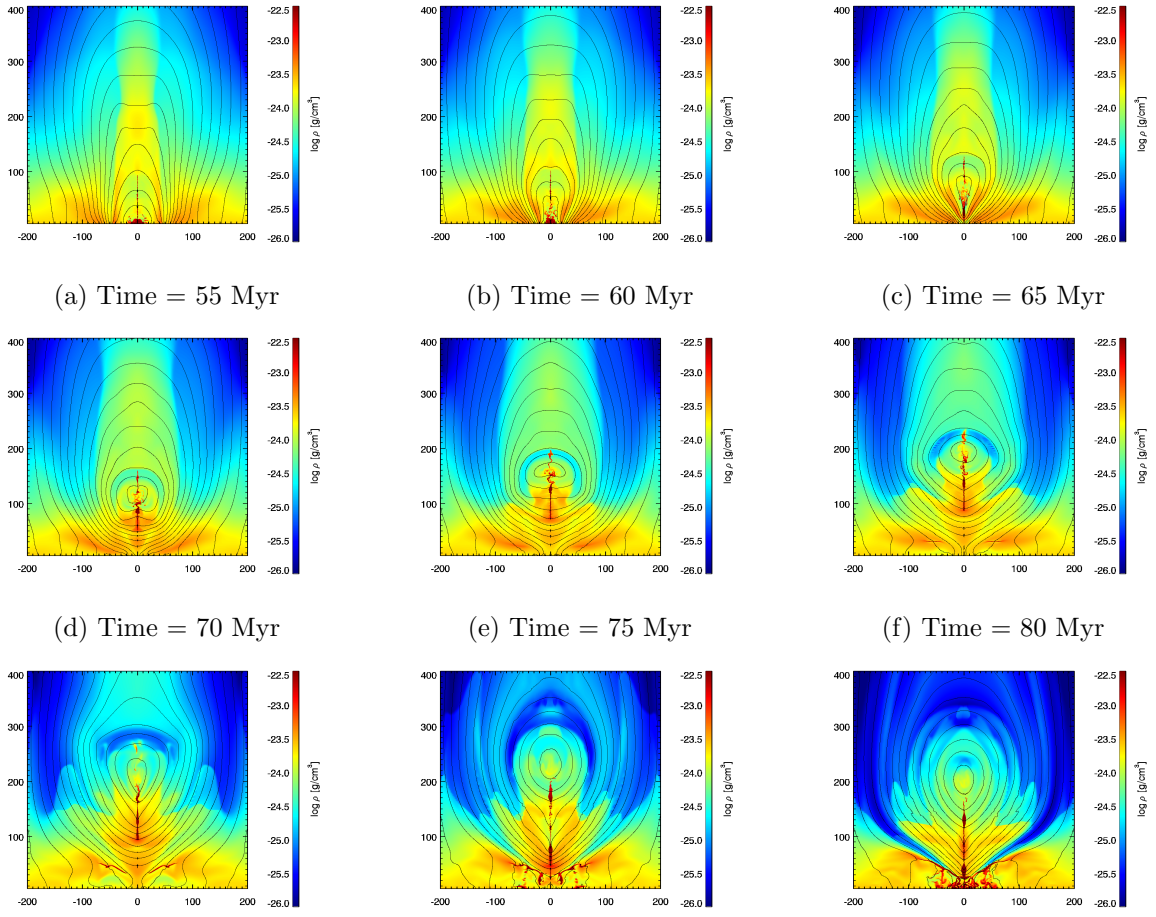

(a) Time = 55 Myr (b) Time = 60 Myr (c) Time = 65 Myr

(d) Time = 70 Myr (e) Time = 75 Myr (f) Time = 80 Myr

(g) Time = 90 Myr (h) Time = 110 Myr (i) Time = 130 Myr

Figure 3.21: Evolution of the density in $x - z$ plane for model B ($t = 55 - 130$ Mrys).

Figure 3.21 shows that magnetic reconnection occurs in model B at around $t \sim 60$ Myr and that it elevates the dense filament to a maximum height ~ 200 pc, which is less than that observed for model A (~ 400 pc). The maximum downflow speed of the dense gas along the magnetic field lines of the magnetic flux rope is ~ 5 km s^{-1}. The filament can only be sustained for around 20 Myr and falls down into the region below $z = 100$ pc. The height of the flux rope's center also decreases with time.

Figure 3.22 shows the time evolution of the density for model C where the shear speed at the lower boundary is 8 km $^{-1}$. The maximum height of the filament ejected after magnetic reconnection at t =60 Myr is 700 pc which is higher than that for model A and the maximum downward speed of the gas flow is ∼20 km s^{-1}

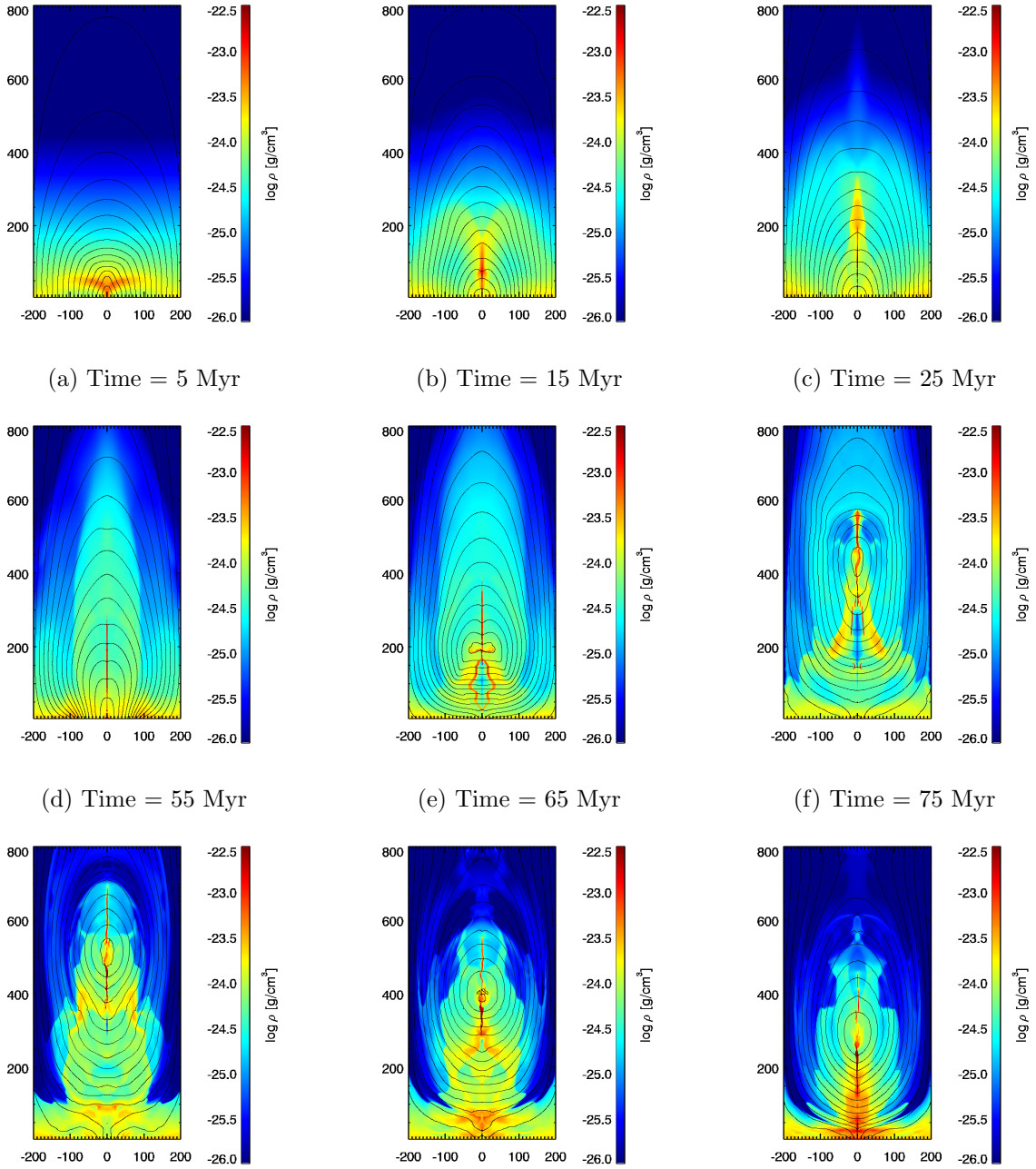

(a) Time = 5 Myr (b) Time = 15 Myr (c) Time = 25 Myr

(d) Time = 55 Myr (e) Time = 65 Myr (f) Time = 75 Myr

(g) Time = 100 Myr (h) Time = 110 Myr (i) Time = 120 Myr

Figure 3.22: Evolution of the density in $x - z$ plane for model C.

Figure 3.23 depicts the evolution of density for model D where Ω is 16 $\times$ 10^{-15} rad s^{-1} (twice as fast as that of the other models). Since the cooling instability occurs earlier during the propagation of the slow magnetosonic waves, the dense filament that was formed before magnetic reconnection shows two arms at z = 50 - 100 pc. The maximum height of the filament ejected after magnetic reconnection at t = 70 Myr is z = 400 pc, which is higher than that observed for model A.

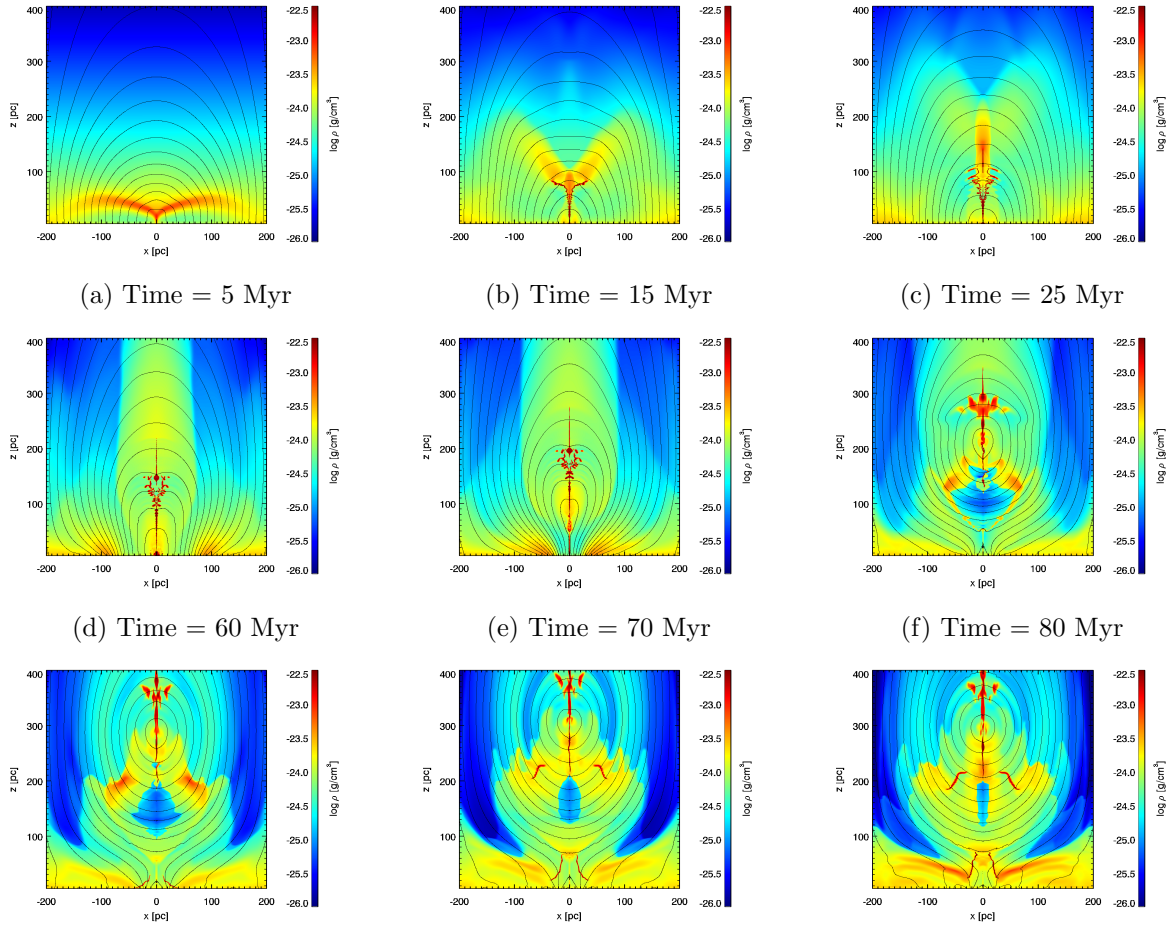

(a) Time = 5 Myr (b) Time = 15 Myr (c) Time = 25 Myr

(d) Time = 60 Myr (e) Time = 70 Myr (f) Time = 80 Myr

(g) Time = 90 Myr (h) Time = 100 Myr (i) Time = 110 Myr

Figure 3.23: Evolution of the density in $x - z$ plane for model D.

Figure 3.24 compares the time variations in magnetic energy for models A, B, C, and D. The energy increase is the fastest in model C due to the faster shear motion; however it increases slowly in model B where $\beta = 1$ at the initial state.

Figure 3.25 compares the time variations in kinetic energy for the same models. The kinetic energy increases drastically after the onset of magnetic reconnection, which occurs at $t \sim 90$, 60, 60, 70 Myr for model A, B, C, and D, respectively.

Figure 3.26 compares the time variations in thermal energy. Model A shows a smaller energy increase because the compressed gas is converted to CNM by cooling. The thermal energy increases after magnetic reconnection in models C and D.

Figure 3.27 compares the time variations in gravitational energy. Model C shows the largest energy increase, because its plasmoid ejection speed is the fastet from among all the models. Since the ejected gas falls downward, the gravitational energy decreases after 90 Myr in models B, C, and D.

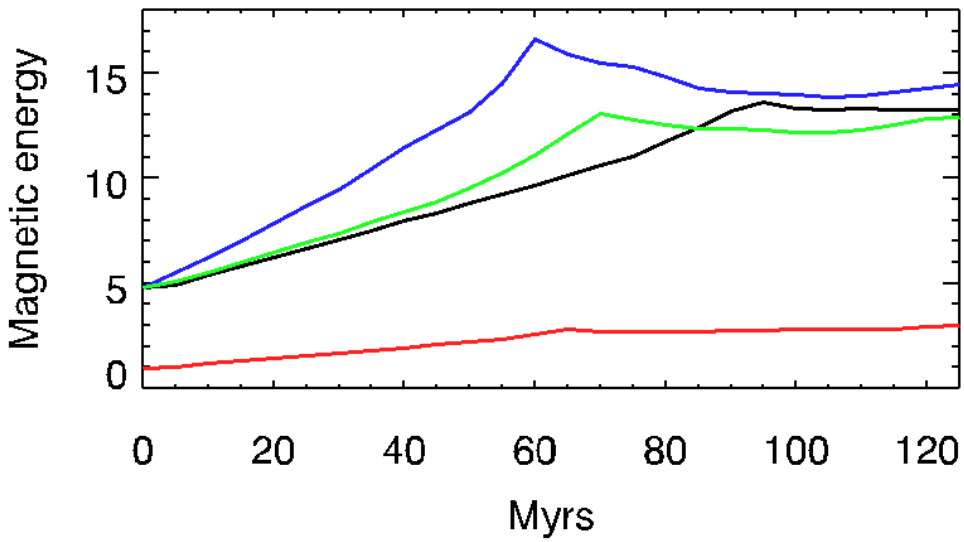

Figure 3.24: Evolution of the magnetic energy for models A (black), B (red), C (blue), and D (green), normalized by the initial thermal energy.

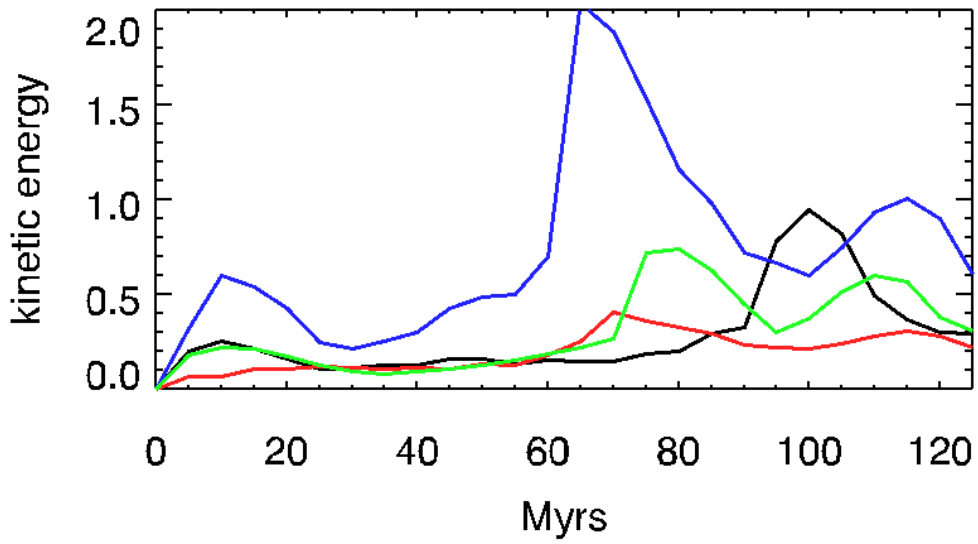

Figure 3.25: Evolution of the kinetic energy for models A (black), B (red), C (blue), and D (green), normalized by the initial thermal energy.

Figure 3.28 depicts the time evolution in the mass of the dense filament computed using cool ($T < 500$ K) gas in the region $|x| < 20$ pc and $z > 50$ pc. In models A, C and

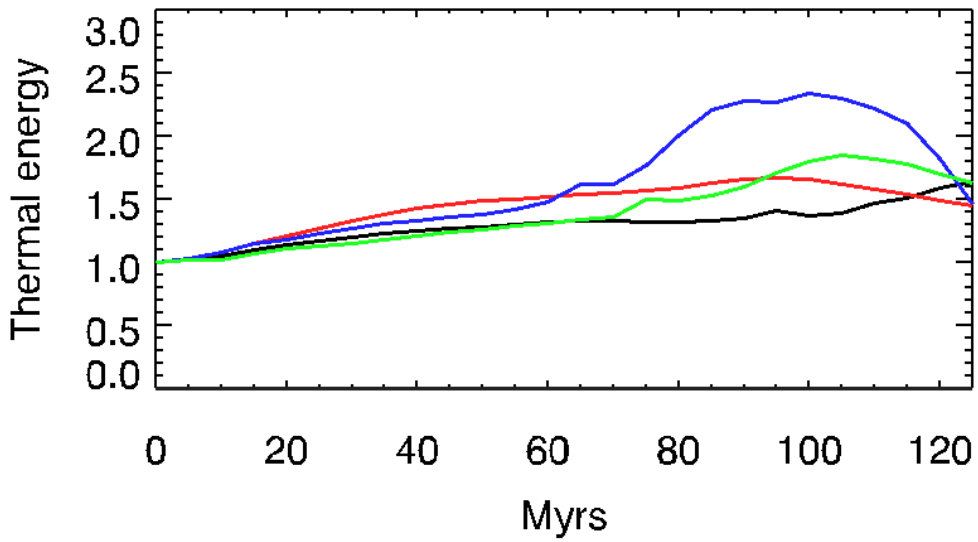

Figure 3.26: Evolution of the thermal energy for models A (black), B (red), C (blue), and D (green), normalized by the initial thermal energy.

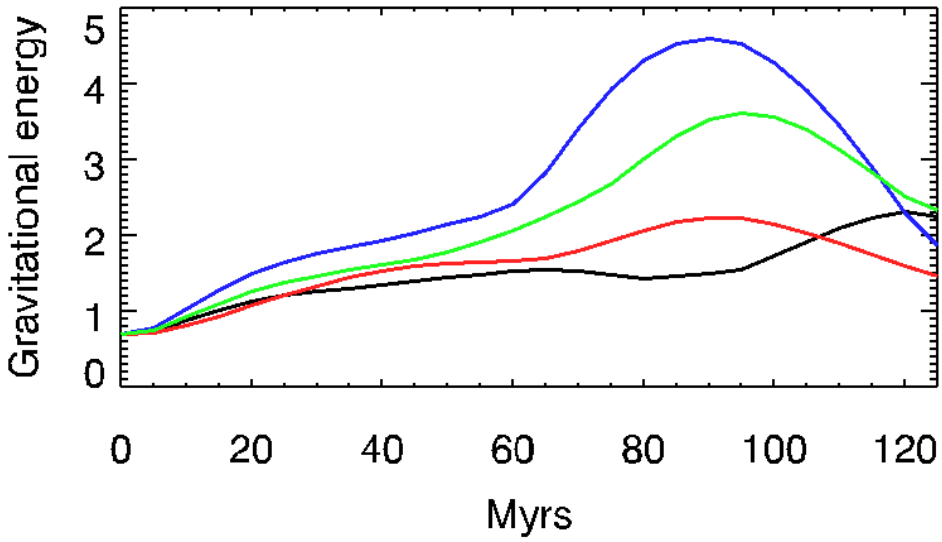

Figure 3.27: Evolution of the gravitational energy for models A (black), B (red), C (blue), and D (green), normalized by the initial thermal energy.

D, the total mass exceeds $10^5 M_\odot$ and is still increasing; however, it decreases in model B because the filament falls down to $z < 50$ pc

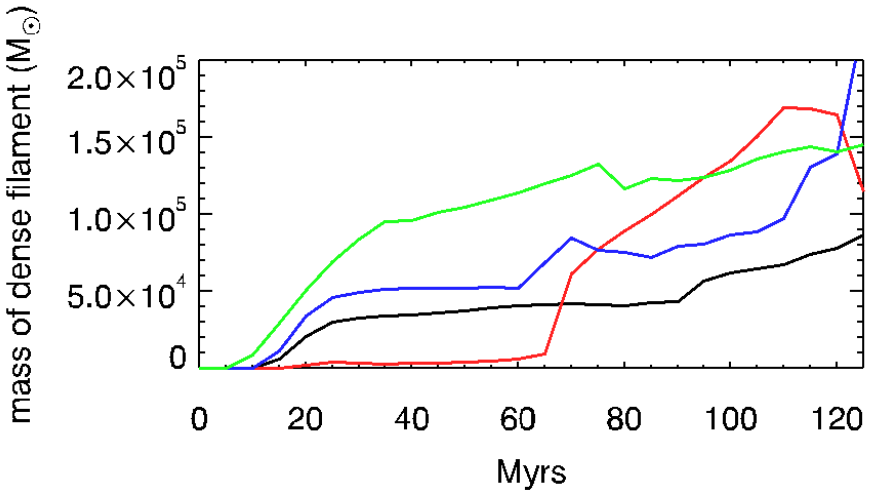

Figure 3.28: Evolution of the mass of the dense, cool filament ($T < 500$ K) for models A (black), B (red), C (blue), and D (green).

Figure 3.29 depicts the magnetic field lines, which were identified by the choosing the points where the y-component of vector potential is 1.4×10^{15} G cm (Models A, C, and D) or 0.63×10^{15} G cm (Model B). Figures 3.29 (b), (c), (d), and (e) depict the stages at which magnetic reconnection occurs. Figure 3.30 illustrates the evolution of the height of the identified magnetic field loops at $x = 0$ pc. The height of loop's top increases during the magnetic reconnection and plasmoid ejection. In models B, C, and D, it starts to decrease at 15-20 Myr after the onset of magnetic reconnection.

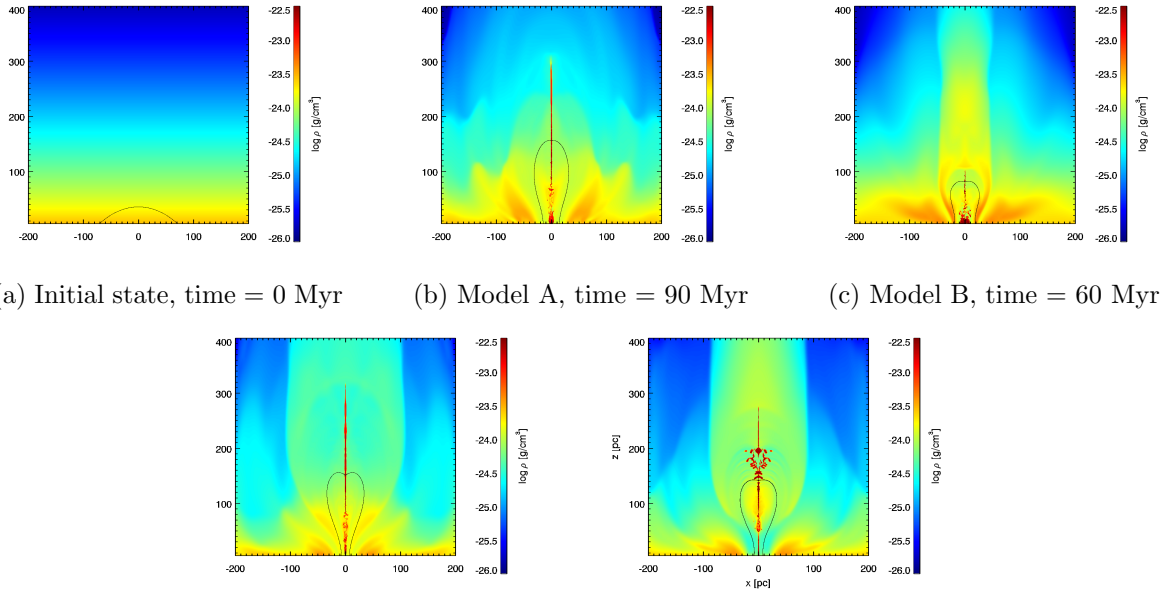

(a) Initial state, time = 0 Myr (b) Model A, time = 90 Myr (c) Model B, time = 60 Myr

(d) Model C, time = 60 Myr (e) Model D, time = 70 Myr

Figure 3.29: Density distribution (color) and magnetic field lines (black curves), which were identified by choosing the points where the y-component of the vector potential A_y = 1.4 × 10^{15} G cm (Models A, C, D) or 0.63 × 10^{15} G cm (Model B) at (a) initial state and (b)-(e) the stage when magnetic reconnection occurs.

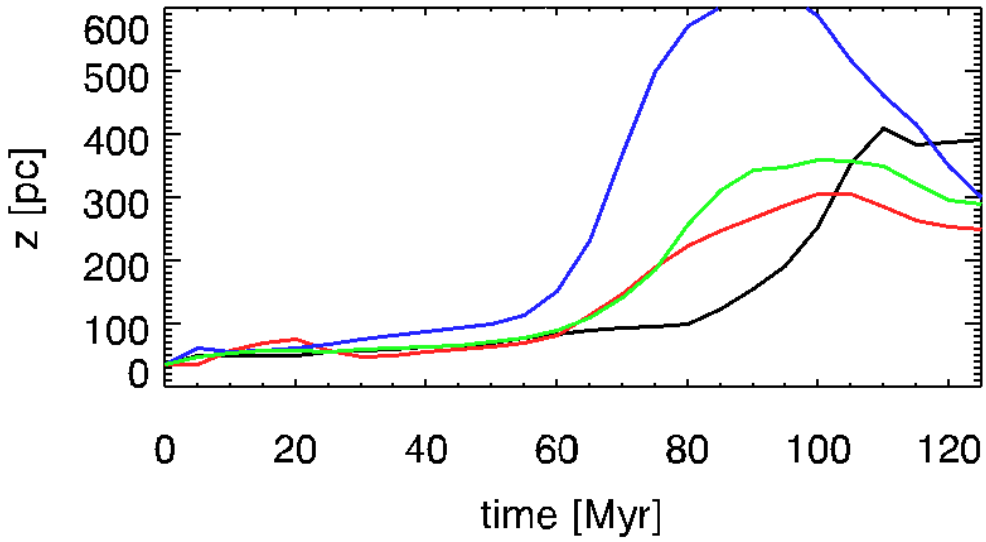

Figure 3.30: Evolution of the height of the top of the magnetic loop at $x = 0$ for models A (black), B (red), C (blue) and D (green).

Chapter 4

Prominence Formation in Nonuniform Galactic Gravitational Fields

In this chapter, we present the results of two-dimensional MHD simulations of the formation of galactic prominences in the gravitational fields of the Galactic central region. In contrast to the uniform gravity model adopted in Chapter 2 and Chapter 3, these account for the changes in the gravitational acceleration with height. This increases the potential difference between the galactic disk and halo, which causes the dense gas in the galactic prominence to fall with faster speed.

4.1 Gravitational Potential and Initial Conditions

The axisymmetric Miyamoto-Nagai potential, which was modified by Sofue (1996) is adopted.

$$\Phi(R,z) = -\sum_{n=1}^{2}\left(\frac{GM_i}{\left\{R^2+\left[a_i+(z^2+b_i^2)^{1/2}\right]^2\right\}^{1/2}}\right) \tag{4.1}$$

Here, $R = 1$ kpc is the radius from the Galactic center. Two component are considereds: a bulge ($n = 1$) and a disk ($n = 2$). For the bulge component, $M_1 = 0.1\times\ 10^{11}$ $M_\odot$, $a_1 = 0.0$ kpc, and $b_1 = 0.75$ kpc are assumed. For the disk component, $M_2 = 1.6\times$ 10^{11} $M_\odot$, $a_2 = 6.0$ kpc, and $b_2 = 0.5$ kpc are assumed. Figure 4.1 shows the distribution

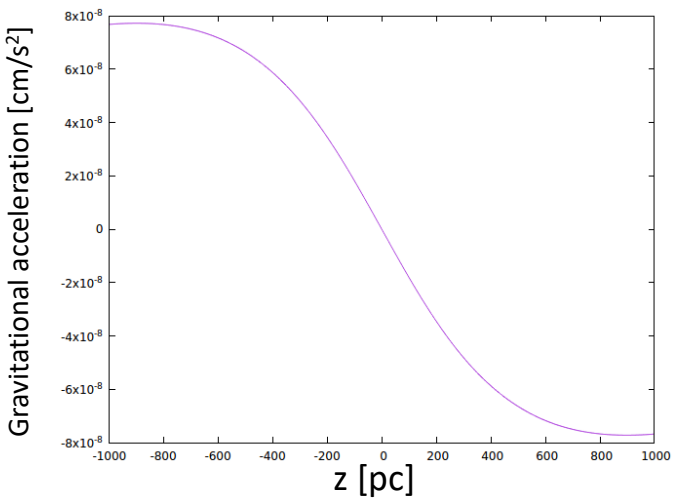

Figure 4.1: Vertical distribution of gravitational acceleration g_z.

of the gravitational acceleration $g_z = -\nabla\Phi(1\mathrm{kpc}, z)$. The gravity increases with height at $z = 0$ - 500 pc.

The simulation box covers -200 pc $< x <$ 200 pc and 5 pc $< z <$ 1226 pc. In x-direction the mesh size is $\Delta x = 0.5$ pc. In z-direction the mesh size is $\Delta z = 0.5$ pc when 5 pc $< z <$ 255 pc; this size is subsequently increased 5% at each mesh point up to $\Delta z =$ 5 pc for $z >$ 255 pc. A total of 806 $\times$ 726 mesh points are used.

The unperturbed force-free magnetic field is as follows:

$$B_x = -\left(\frac{2L_a}{\pi H_m}\right) B_a \cos\left(\frac{\pi}{2L_a}x\right) \exp\left(-\frac{z}{H_m}\right) \tag{4.2}$$

$$B_y = \sqrt{1-\left(\frac{2L_a}{\pi H_m}\right)^2}\, B_a \cos\left(\frac{\pi}{2L_a}x\right) \exp\left(-\frac{z}{H_m}\right) \tag{4.3}$$

$$B_z = B_a \sin\left(\frac{\pi}{2L_a}x\right) \exp\left(-\frac{z}{H_m}\right) \tag{4.4}$$

Here $L_a = 100$ pc and $H_m = 80$ pc. We adopted a smalles H_m value than that adopted in previous chapters because the scale height of the interstellar medium was smaller due to the strong gravity. We adopted the same cooling/heating function adopted in previous chapters (equations 2.7-2.9) and assumed that the interstellar medium is in hydrostatic state and thermal equilibrium in its unperturbed state. In the region where $z >$ 90 pc, we assumed a hot corona with T_{corona} =1.0$\times 10^6$ K. Figure 4.2 shows the initial density, temperature, and plasma β distributions for a model with $\beta = 0.2$ at $z = 5$ pc.

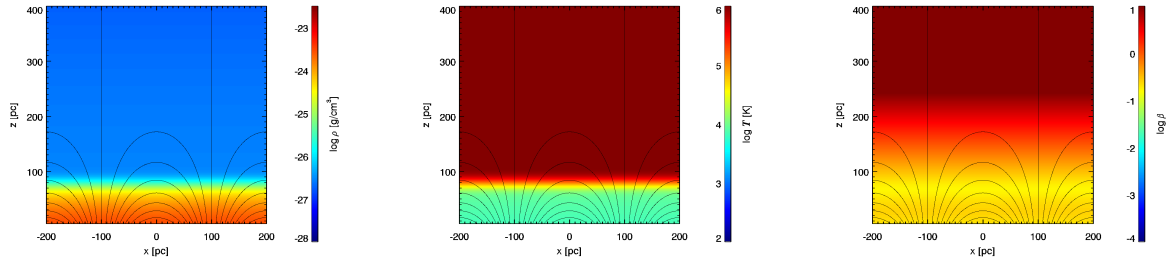

(a) Density (b) Temperature (c) Plasma β

Figure 4.2: Initial density, temperature, and plasma β distribution.

4.2 Numerical Method

To initiate the rising motion of the magnetic arcades, we introduced shear motions at the lower boundary ($z = 5$ pc) by setting the y- and z-components of the velocity, v_y and v_z, as follows

$$v_y = \begin{cases} -v_0 \sin(2\pi x/L_a) & |x| < L_a \\ 0 & \text{otherwise} \end{cases} \tag{4.5}$$

$$v_z = 0 \tag{4.6}$$

Here v_0 is 4 km s^{-1}. Figure 4.3 depicts the profile of v_y at $z = 5$ pc. Free boundary

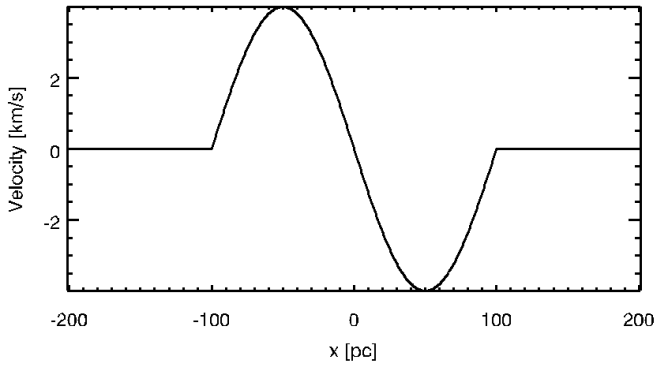

Figure 4.3: Shear motion imposed at the lower boundary.

conditions were applied at the lower boundary for v_x and magnetic field. The density and pressure are fixed to the initial values. The boundary conditions in x-direction are symmetric for ρ, P, B_x, B_y, and v_z and anti-symmetric for B_z, v_x, and v_y. The absorbing boundary conditions are applied at $z > 1200$ pc. The resistive magnetohydrodynamic equations 2.1-2.5 are solved using CANS+ (Matsumoto et al. 2016) which uses the HLLD

scheme. This simulation code is used in this study because it is more robust for strongly magnetized regions than the second order scheme that was used in Chapter 2 and Chapter 3. Fifth order spatial accuracy is attained by the MP5 scheme (Suresh & Huynh 1997). A third order TVD Runge-Kutta method is used for time integration. The solenoidal condition $\nabla \cdot \boldsymbol{B} = 0$ is approximately satisfied using the generalized Lagrange multiplier (GLM) scheme proposed by Dedner et al. (2002). The heating/cooling term is included by time-implicit method. The parameters used for the simulations are listed in Table 4.1. Since plasma β at top of the magnetic arcades could be smaller than those for the models presented in Chapter 2 and Chapter 3, the time step determined by the Courant condition sometimes becomes to be too small in late stage. Thus, we restrict the density at $\rho_{\rm min} = 10^{-28}$ g/cm^3 (density floor value) and set $\rho = \max(\rho, \rho_{\rm min})$. Only the region around the top of the loop is affected by this density floor.

Model	β	v_y km/s	v_x km/s	Ω s^{-1}	$\Delta x_{\rm min}$ pc	$\Delta z_{\rm min}$ pc	Heating rate Γ erg s^{-1}
GA	0.2	4	0	8×10^{-15}	0.5	0.5	2×10^{-26}
GB	1.0	4	0	8×10^{-15}	0.5	0.5	2×10^{-26}
GC	0.2	4	4	8×10^{-15}	0.5	0.5	2×10^{-26}
GH	0.2	4	0	8×10^{-15}	0.5	0.5	10×10^{-26}

Table 4.1: Parameters for models reported in this chapter.

4.3 Numerical Results

Figure 4.4 shows the evolution of the density and magnetic field lines for model GA (β =0.2) where we imposed shear motion v_y at -100 pc $< x <$ 100 pc in the lower boundary. After the fast and slow magnetosonic waves propagated, a dense filament is formed around -20 pc $< x <$ 20 pc and $z <$ 50 pc. The height of the filament's top is lower than that for model A in Chapter 3 because the scale height of the disk is smaller. Since we did not impose shear motion for $|x| >$ 100 pc, the magnetic arcade is elevated only in the central region. Magnetic reconnection occurs between t = 42 Myr and t = 48 Myr, thereby forming a magnetic flux rope. Magnetic reconnection is observed earlier than in model A because the rising magnetic arcade can expand in the x-direction, which indicates that the magnetic field lines deform into an $\Omega-$shape earlier than model A.

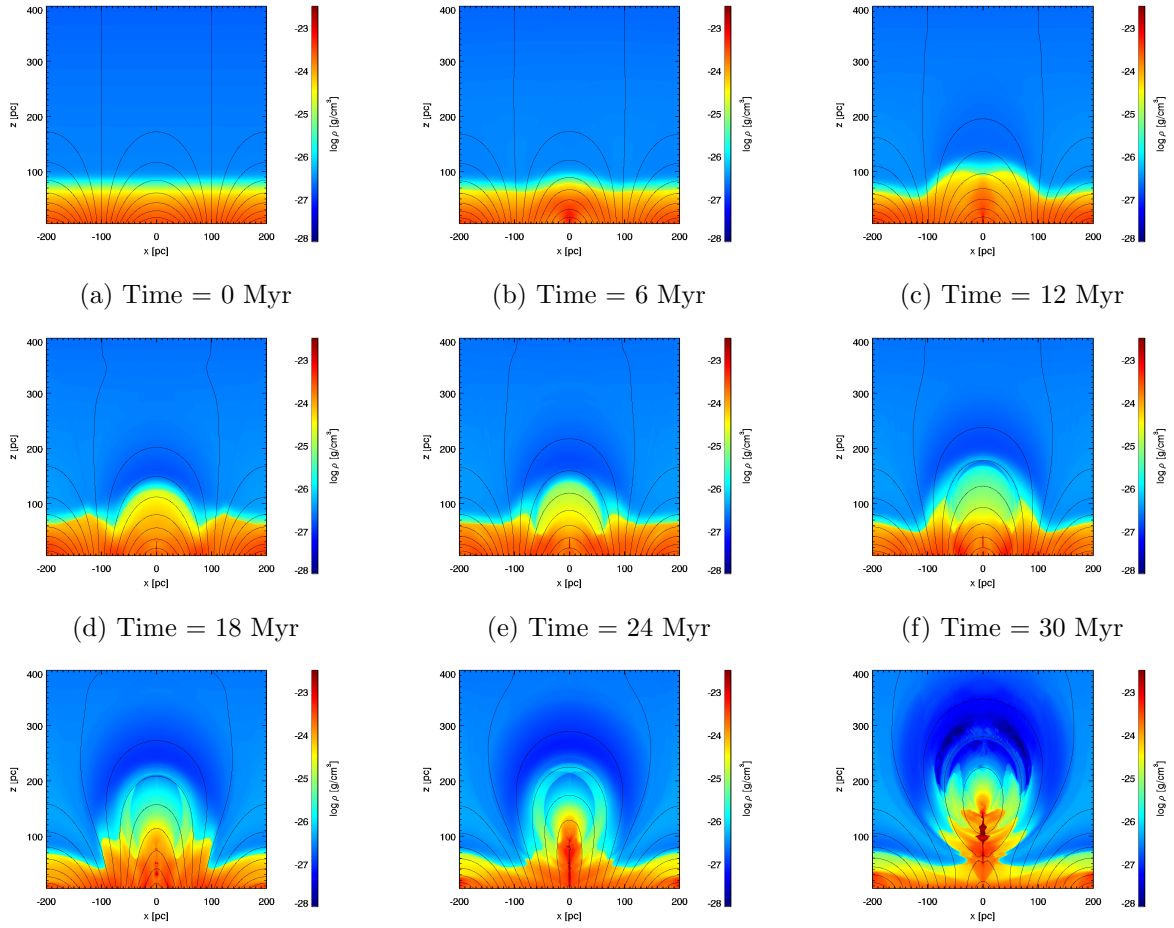

(a) Time = 0 Myr (b) Time = 6 Myr (c) Time = 12 Myr

(d) Time = 18 Myr (e) Time = 24 Myr (f) Time = 30 Myr

(g) Time = 36 Myr (h) Time = 42 Myr (i) Time = 48 Myr

Figure 4.4: Evolution of density (color) and magnetic field lines (solid line) for model GA ($t = 0 - 48$ Mrys).

After the occurrence of the magnetic reconnection, warm, dense medium accumulates around $x = 0$ pc and $z = 120$ pc at $t = 48$ Myr. Since the density in this region exceeds the density required to onset thermal instability, a cool, dense filament is formed around the bottom of the flux rope. Figure 4.5 shows the plasma β distributions for model GA at $t = 24$, 36, and 48 Myr. When the flux rope is formed in the hot corona, the gas in the upper part of the flux rope falls downward, which creates a low β region in the upper part of the flux rope.

Figure 4.6 depicts the time evolution of the mass of the filament ($T < 500$ K) in -20 $< x <$ 20 pc and z $>$ 50 pc. Here the longitudinal length of the filament perpendicular to the $x-z$ plane is assumed to be 600 pc. The dense filament (prominence) appears around $t = 40$ Myr when magnetic reconnection occurs, and its mass increases and reaches 10^5 $M_\odot$ at $t = 48$ Myr

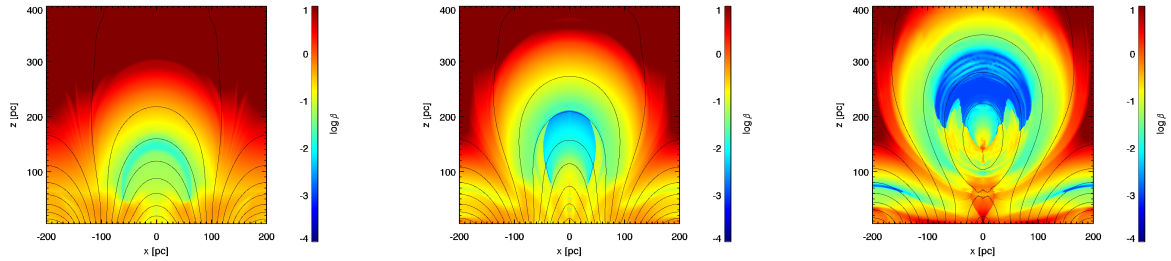

(a) Time = 24 Myr (b) Time = 36 Myr (c) Time = 48 Myr

Figure 4.5: Evolution of Plasma β (color) and magnetic field lines (solid line) for model GA ($t = 24 - 48$ Mrys).

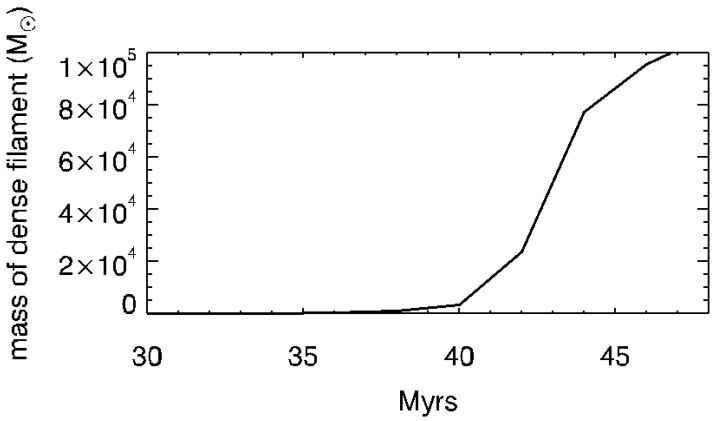

Figure 4.6: Evolution of dense, cool mass ($T < 500$ K) for model GA.

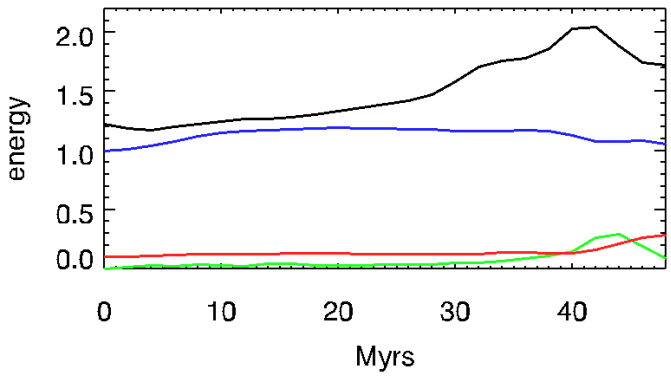

Figure 4.7: Evolution of magnetic energy (black), kinetic energy (green), gravitational energy (red) and thermal energy (blue) for model GA, normalized by the initial thermal energy.

Figure 4.7 shows the time evolution of various energies for model GA, normalized by the initial thermal energy. The thermal energy is comparable to the magnetic energy at $t = 0$ because the gas pressure is dominant in the corona (see figure 4.2(c)). The magnetic energy increases more slowly than that in model A because the imposed shear motions is restricted to a smaller region (only $|x| < 100$ pc). After the onset of the magnetic reconnection, the magnetic energy is converted into both kinetic and gravitational energy.

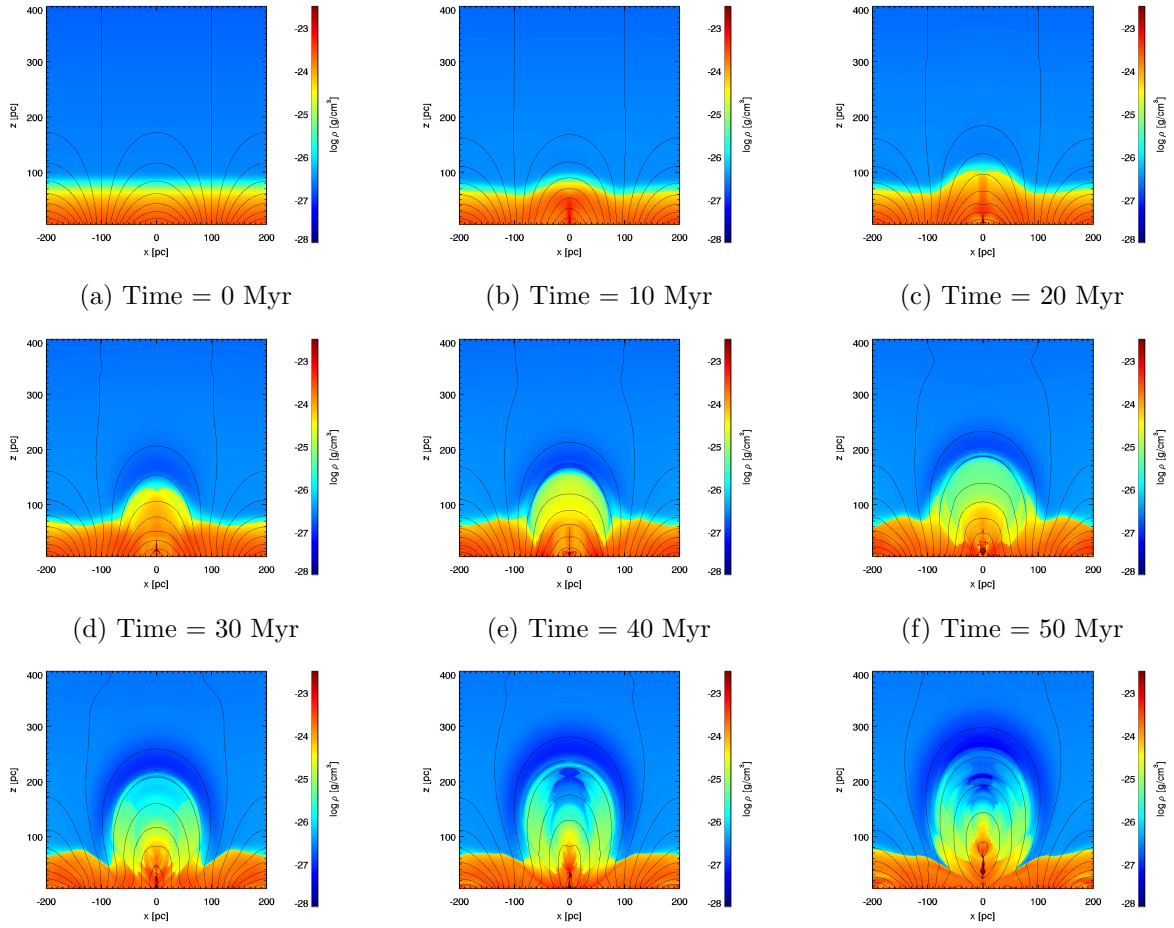

(a) Time = 0 Myr (b) Time = 10 Myr (c) Time = 20 Myr

(d) Time = 30 Myr (e) Time = 40 Myr (f) Time = 50 Myr

(g) Time = 60 Myr (h) Time = 70 Myr (i) Time = 80 Myr

Figure 4.8: Evolution of density (color) and magnetic field lines (solid line) for model GB in which the magnetic pressure is comparable to the gas pressure ($t = 0 - 80$ Mry).

Figure 4.8 depicts the evolution of density and magnetic field lines for model GB ($\beta = 1.0$). Magnetic reconnection occurs at around $t \sim 74$ Myr, and the dense filament is elevated but its hight is at maximum of 30-60 pc, which is lower than that of model GA (~ 140 pc).

Figure 4.9 shows the evolution of density and magnetic field lines for model GC where we have imposed both shear and converging motion at -100 pc $< x <$ 100 pc when $z = 5$

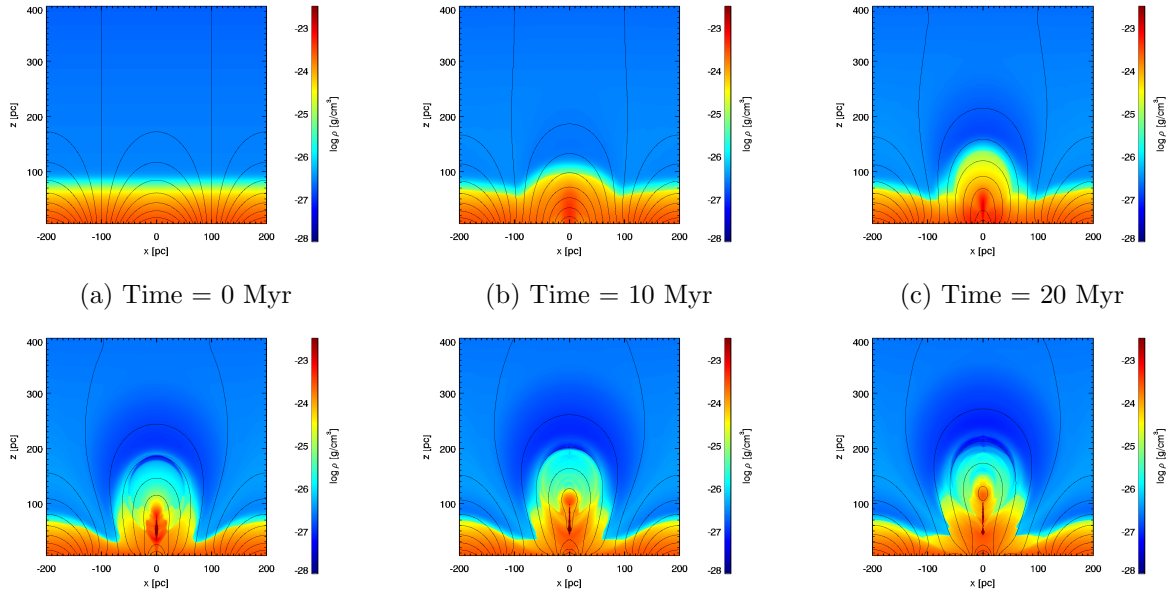

(a) Time = 0 Myr (b) Time = 10 Myr (c) Time = 20 Myr

(d) Time = 30 Myr (e) Time = 40 Myr (f) Time = 50 Myr

Figure 4.9: Evolution of density (color) and magnetic field lines (solid line) for model GC ($t = 0 - 50$ Mrys).

pc. Due to the onset of cooling instability, a dense filament forms at around $x = 0$ pc and $z = 30$ - 70 pc when $t = 20$ Myr and creates the maximum mass of the dense filament $\sim 7 \times 10^4$ $M_\odot$.

Figure 4.10 shows the evolution of density and magnetic field lines for model GH where we adopted larger heating rate to simulate the region with higher equilibrium density. The magnetic reconnection occurs around $t \sim 38$ Myrs and the dense filament is lifted up to ~ 90 pc. The mass of dense filament at -20 $< x <$ 20 pc and z $>$ 50 pc rapidly increase after $t = 40$ Myr. At $t = 48$ Myrs. The maximum mass of the dense filament is $\sim 10^6$ $M_\odot$.

Figure 4.11 shows evolution by which dense, cool mass ($T < 500$ K) is formed in the region -20 $< x <$ 20 pc and $z > 50$ pc for models GA, GB, GC, and GH. Since magnetic pressure in model GB is lower than that in the other models, the dense, cold filament cannot be elevated and is instead formed only at low latitudes ($z < 50$ pc). In model GC, the converging motion compress the warm medium in the equatorial region, which forms the dense, cold filament earlier than in model GA. Its mass decreases after $t = 46$ Myr because the filament falls down to $z < 50$ pc. In model GH, since the initial density is higher, the mass of dense filament approaches to $\sim 10^6$ $M_\odot$ which is comparable to the

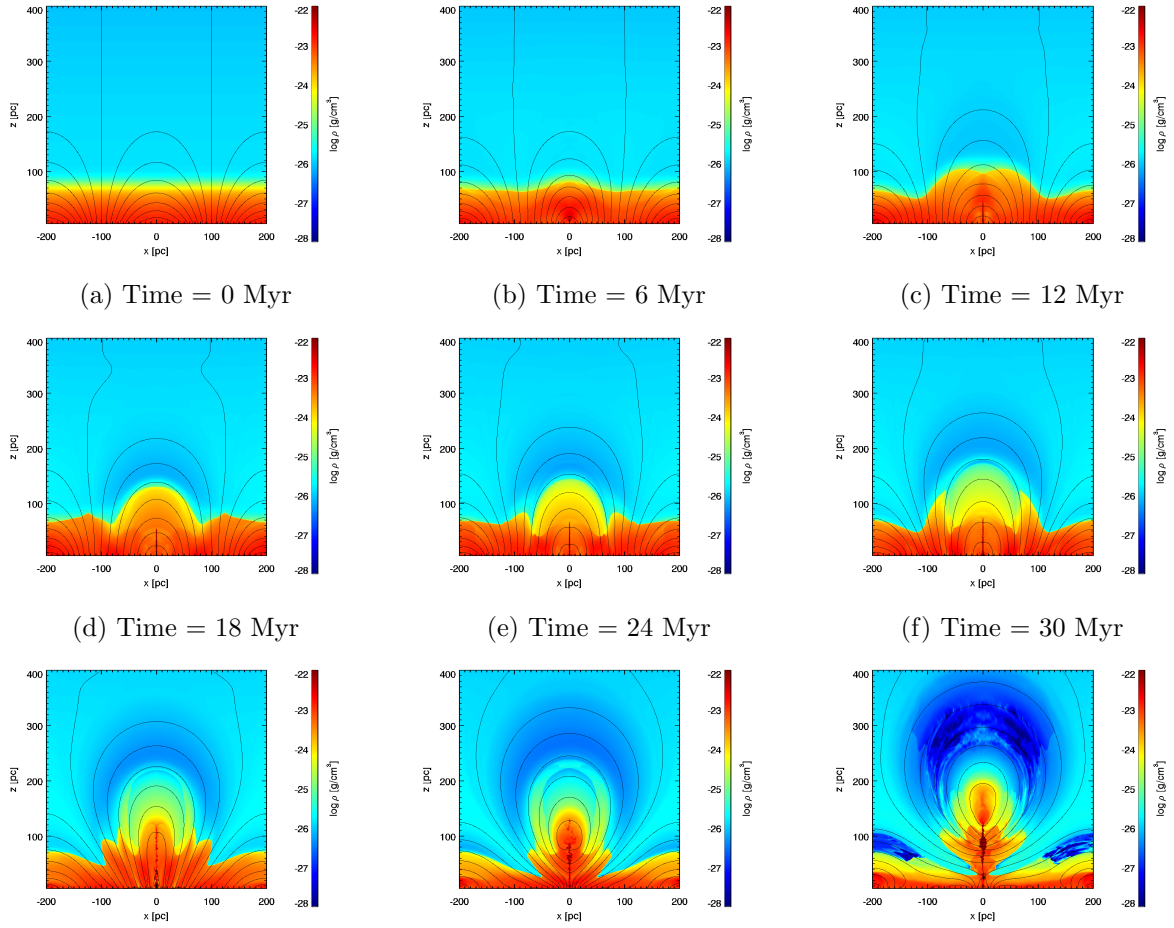

(a) Time = 0 Myr (b) Time = 6 Myr (c) Time = 12 Myr

(d) Time = 18 Myr (e) Time = 24 Myr (f) Time = 30 Myr

(g) Time = 36 Myr (h) Time = 42 Myr (i) Time = 48 Myr

Figure 4.10: Evolution of density (color) and magnetic field lines (solid line) for model GH ($t = 0 - 48$ Mrys).

mass of the molecular loops observed in Galactic central region.

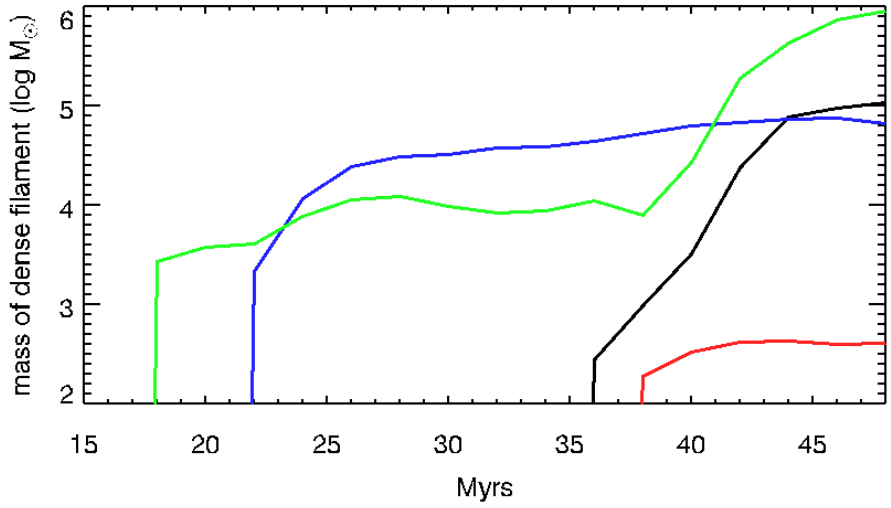

Figure 4.11: Evolution of the dense, cool mass ($T < 500$ K) in the region -20 $< x <$ 20 pc and $z > 50$ pc for models GA (black), GB (red), GC (blue), and GH (green).

Chapter 5

Three-Dimensional Numerical Simulations

In this chapter, we report the results of three-dimensional simulations of Galactic prominences formed by motions at the footpoints of magnetic arcades. Figure 5.1(left) schematically shows the dense filament (blue) confined by helical magnetic fields. When such horizontal, helical magnetic fields are perturbed, dense matter in the filament slides down along the helical magnetic fields (right). Such sliding motion can be the origin of velocity gradients and large velocity dispersions observed in molecular loops in the Galactic central region.

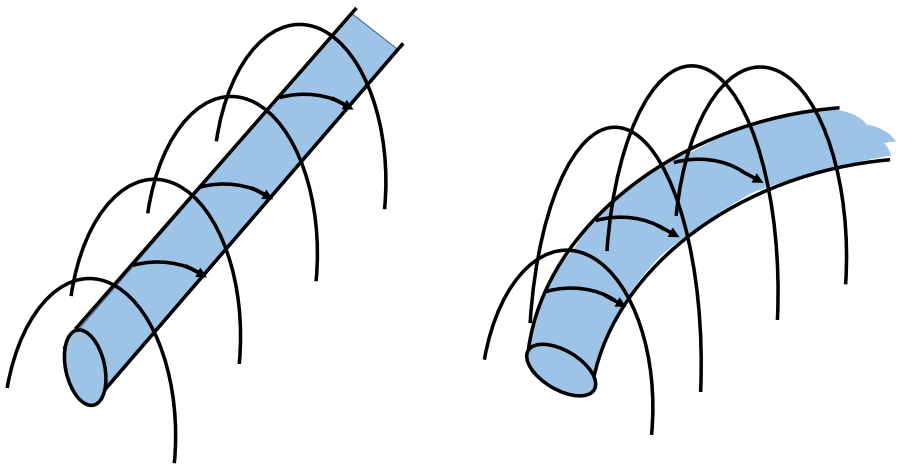

Figure 5.1: Schematic picture of the dense filament confined by helical magnetic fields.

Three-dimensional simulations of the reconnection condensation model of the solar prominence have been carried out by Kaneko and Yokoyama (2017) and Kaneko (2017, PhD Thesis). They showed that thermal conduction along the longitudinal magnetic fields confining the dense filament plays an essential role to stabilize the cooling instability. Kaneko and Yokoyama (2017) showed that solar prominences can be formed when the longitudinal length of magnetic fields becomes longer than the Field length defined as the length in which the conduction time scale is comparable to the cooling time scale. Since the cooling time scale becomes shorter than the conduction time scale when this condition is satisfied, dense region can be cooled down. In Galactic prominences, because the Field length is ~ 0.1 pc as we discussed in Chapter 1.5, the length of the magnetic loops is long enough to induce the cooling instability.

5.1 Numerical Models for Three-Dimensional Simulations of Galactic Prominence

For three-dimensional simulations of Galactic prominences, we consider a local part of the disk and take x, y coordinate as horizontal direction, and z-coordinate in vertical direction.

Figure 5.2 shows the initial state. We set $\rho(z = 5 \text{ pc}) = 1.9 \times 10^{-22}$ g/cm^3 and $P(z = 5 \text{ pc}) = 9.4 \times 10^{-12}$ dyn/cm^2 ($T(z = 5 \text{ pc}) \sim 6000$ K). Gravitational potential is the Miyamoto-Nagai potential modified by Sofue (1996) we adopted in chapter 4. Figure 5.3 shows the potential difference $\Phi(R, 200 \text{ pc}) - \Phi(R, 0 \text{ pc})$. The potential difference between $z = 0$ pc and $z = 200$ pc is 1.07×10^{13} cm^2 s^{-2} for $R = 1$ kpc and 1.47×10^{12} cm^2 s^{-2} for $R = 8.5$ kpc. When the fluid element falls down from $z = 200$ pc, the vertical velocity at $z = 0$ is 46 km/s for $R = 1$ kpc and 17 km/s for $R = 8.5$ kpc. In this section, we adopt $R = 8.5$ kpc. The initial state is a hydrostatic atmosphere with force free magnetic fields. They are expressed as follows:

$$B_x = -\Big(\frac{2L_a}{\pi H_m}\Big) B_a \cos\Big(\frac{\pi}{2L_a}x\Big) \exp\Big(-\frac{z}{H_m}\Big) \tag{5.1}$$

$$B_y = \sqrt{1 - \Big(\frac{2L_a}{\pi H_m}\Big)^2}\, B_a \cos\Big(\frac{\pi}{2L_a}x\Big) \exp\Big(-\frac{z}{H_m}\Big) \tag{5.2}$$

$$B_z = B_a \sin\Big(\frac{\pi}{2L_a}x\Big) \exp\Big(-\frac{z}{H_m}\Big) \tag{5.3}$$

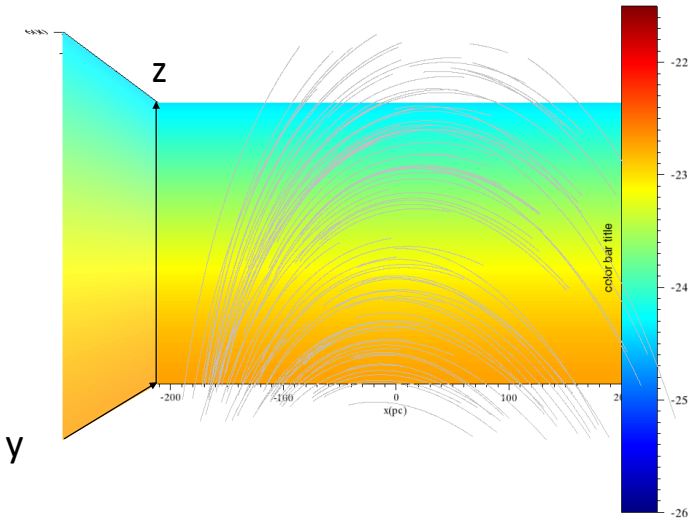

Figure 5.2: Density distribution (color) and magnetic field lines (solid curves) at the initial state of three-dimensional simulations.

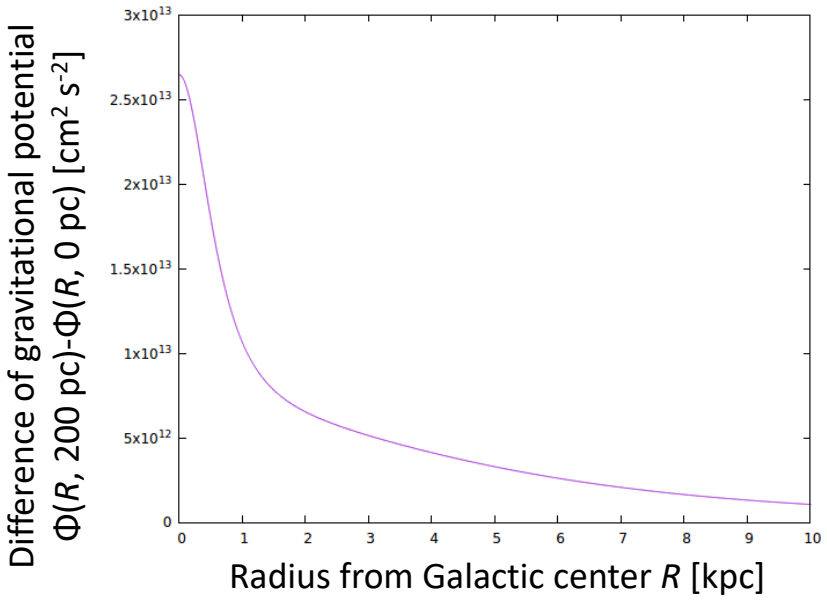

Figure 5.3: The potential difference $\Phi(R,200\ \mathrm{pc})$-$\Phi(R,0\ \mathrm{pc})$.

Here $H_{\mathrm{m}} = 205$ pc is magnetic scale height, and $L_{\mathrm{a}} = 205$ pc is the half length of the magnetic arcade. The plasma β ($= P_{\mathrm{gas}}/P_{\mathrm{mag}}$) is assumed to be $\beta = 0.2$ at bottom of the simulation area ($B_a = 3.52$ x 10^{-5} G). Cooling rate is adopted from Inoue et al. (2006)

as

$$\rho\mathcal{L} = \begin{cases} (-\Gamma + n\Lambda)n & 400 \text{ K} < T < 20000 \text{ K} \\ 0 & \text{otherwise} \end{cases} \tag{5.4}$$

$$\Gamma = 10 \times 10^{-26} \text{ erg s}^{-1} \tag{5.5}$$

$$\Lambda = 7.3 \times 10^{-21} \exp\left(\frac{-118400}{T + 1500}\right) + 7.9 \times 10^{-27} \exp(-92/T) \text{ erg cm}^3 \text{ s}^{-1} \tag{5.6}$$

Here we adopted larger heating rate to simulate the region with higher equilibrium density. Figure 5.4 shows thermal equilibrium curve for smaller (black) and larger (red) heating

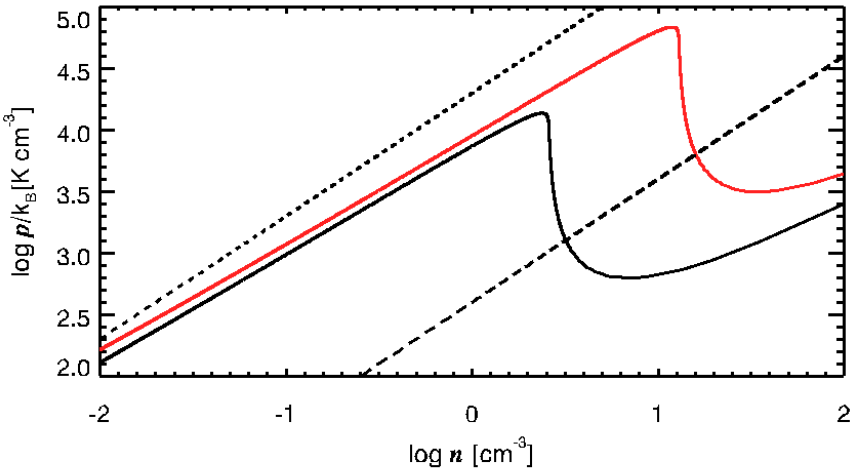

Figure 5.4: Thermal equilibrium curve in $P - n$ plane for models with the heating rate $\Gamma = 2 \times 10^{-26}$ erg s^{-1} (black) and the enhanced heating model with $\Gamma = 10 \times 10^{-26}$ erg s^{-1} (red). Dotted line shows $T = 20000$ K and the dashed curve shows $T = 400$ K.

rate.

Figure 5.5 schematically shows the model for three-dimensional simulation. We adopt Cartesian box covering -205 pc $< x <$ 205 pc, 0 pc $< y <$ 800 pc and 5 pc $< z <$ 1310 pc. Figure 5.5 shows the magnetic fields at the initial state. A red dashed curve in the left panel of shows the initial magnetic field. Red dashed lines in the right panel shows magnetic field lines projected on the $x - y$ plane. Green dashed arrows show the motion at the footpoints of the magnetic loops. In this three dimensional simulation, we assumed converge (v_x) and shear (v_y) motions depending on y. They are imposed at foot points

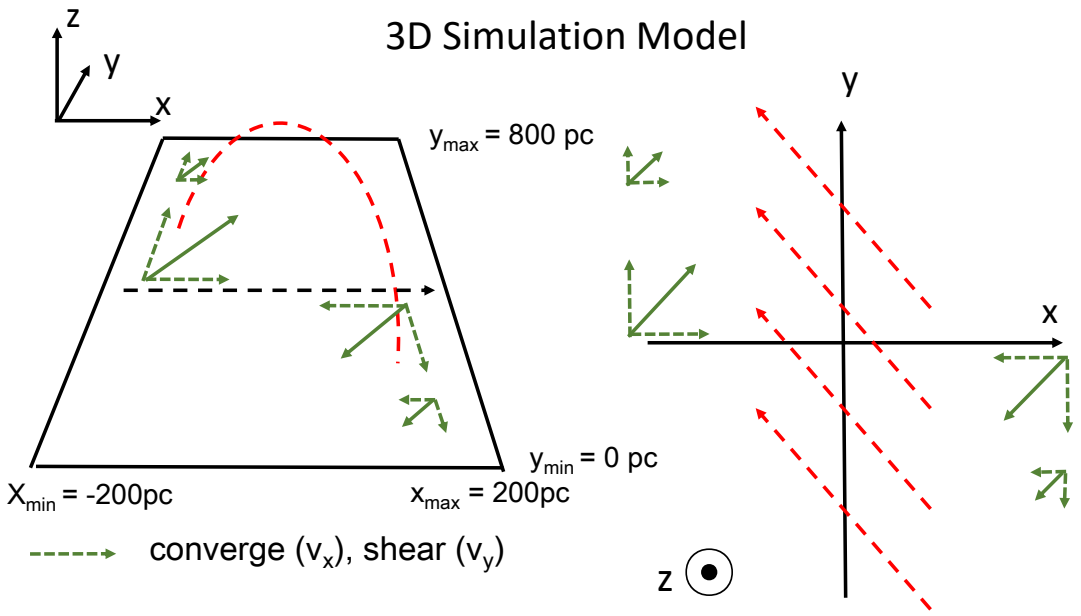

Figure 5.5: Schematic picture of the initial condition of the three-dimensional simulation.

of magnetic arch as follows :

$$v_x = v_y = -v_0(y)\sin\left(\frac{2\pi x}{L_a}\right) \tag{5.7}$$

$$v_z = 0 \tag{5.8}$$

$$v_0(y) = \begin{cases} v_{00} - \frac{1}{2}v_{00}\cos\left(\frac{2\pi(y-200\mathrm{pc})}{400\mathrm{pc}}\right) & 200\ \mathrm{pc} < y < 600\ \mathrm{pc} \\ \frac{1}{2}v_{00} & \text{otherwise} \end{cases} \tag{5.9}$$

Here v_{00} is 4 km/s and L_a is 205 pc. Boundary conditions in x-direction and z-direction are the same as two-dimensional simulation and we applied periodic boundary condition in y-direction. The mesh size is $\Delta x = 1$ pc when $|x| < 10$ pc. When $|x| > 10$ pc, Δx increases by 5 % at each mesh point up to $\Delta x = 2$ pc. The mesh size is $\Delta z = 1$ pc when $|z| < 400$ pc and gradually increases by 5 % at each mesh point up to $\Delta z = 4$ pc when $z > 400$ pc. Uniform mesh with mesh size $\Delta y = 2$ pc is used for y-direction. We adopted the same anomalous resistivity as equation 2.20. The basic equations are solved by applying the HLLD scheme (Miyoshi & Kusano 2005). Second order accuracy in space is preserved by applying MUSCL scheme by linearly interpolating the values at the cell surface, and restricting them using the monotonized central limiter. Third order accurate TVD Runge-Kutta method is adopted in time integration. The solenoidal condition $\nabla \cdot \boldsymbol{B} = 0$ is satisfied by applying the generalized Lagrange multiplier (GLM) scheme proposed by Dedner et al. (2002). The cooling/heating term is included by time-implicit method.

5.2 Numerical Results for $R = 8.5$ kpc

Figure 5.6 shows the density distribution obtained by a three-dimensional MHD simulation. Color shows the density in $y - z$ plane ($x = 0$), and $x - z$ plane ($y = 800$ pc) at $t = 40$ Myrs. Dense, arch-like filament is formed by cooling instability. Figure 5.7 shows magnetic field lines projected on the $x - z$ plane and the density distribution in $x - z$ plane at $y = 400$ pc at $t = 40$ Myr. The dense filament is initially formed by the warm gas accumulated around $x = 0$ by converging flow toward $x = 0$ produced by footpoint motions, and later by accumulation of warm gas downflowing toward the bottom of helical magnetic field lines (magnetic flux rope) formed by magnetic reconnection. When the density of the accumulated gas exceeds the threshold for the cooling instability, dense, cool filaments are formed. The number density of the filament is $n \sim 100$ cm^{-3}, which corresponds to the density of the molecular gas. Note that the critical density for the onset of the cooling instability in this 3D model ($n \sim 10$ cm^{-3}) is larger than other models because the heating rate is artificially enhanced. The thickness of the dense filament in this model is one pc in x-direction. The dense matter accumulated around the bottom of the magnetic flux rope slides down along longitudinal magnetic field lines, and form dense cold loop similar to the galactic center molecular loops.

Figure 5.8 shows the velocity distribution in $y-z$ plane at $t = 40$ Myrs. In the regions 200 pc $< y <$ 300 pc, and 500 pc $< y <$ 600 pc, the dense, cold material slides down along magnetic field lines with speed ~ 13 km/s. Since this speed exceeds the sound speed of the warm gas, shock waves are formed around the footpoints of the longitudinal loop, and the shock compressed gas forms dense regions around $(y, z) =$ (220 pc, 10 pc) and (580 pc, 10 pc). These shocked layer may correspond to the footpoints of Galactic Center molecular loops where the emission of shock tracer molecules such as SiO are observed (Riquelme et al. 2010, 2017).

To compare numerical results with observations of Galactic Center molecular loops, we computed the line of sight velocity by assuming the direction of the line of sight. Figure 5.9 schematically shows the dense loop in $x - y$ plane (blue) and the direction of the line of sight (red arrow). The line of sight velocity is computed by $(v_{\rm x}, v_{\rm y})$ as $v_{\parallel} = v_{\rm x} \cos\theta - v_{\rm y} \sin\theta$, where $\theta = 60$ degree is the angle between the $y-$axis and the projection plane perpendicular to the line of sight. Figure 5.10 shows the $p - v$ diagram plotted by using this line of sight velocity. The dense loop has constant velocity gradient

with 5 km/s per 100 pc. Velocity dispersion along the loop and at the foot points of the loops are about 15 km/s.

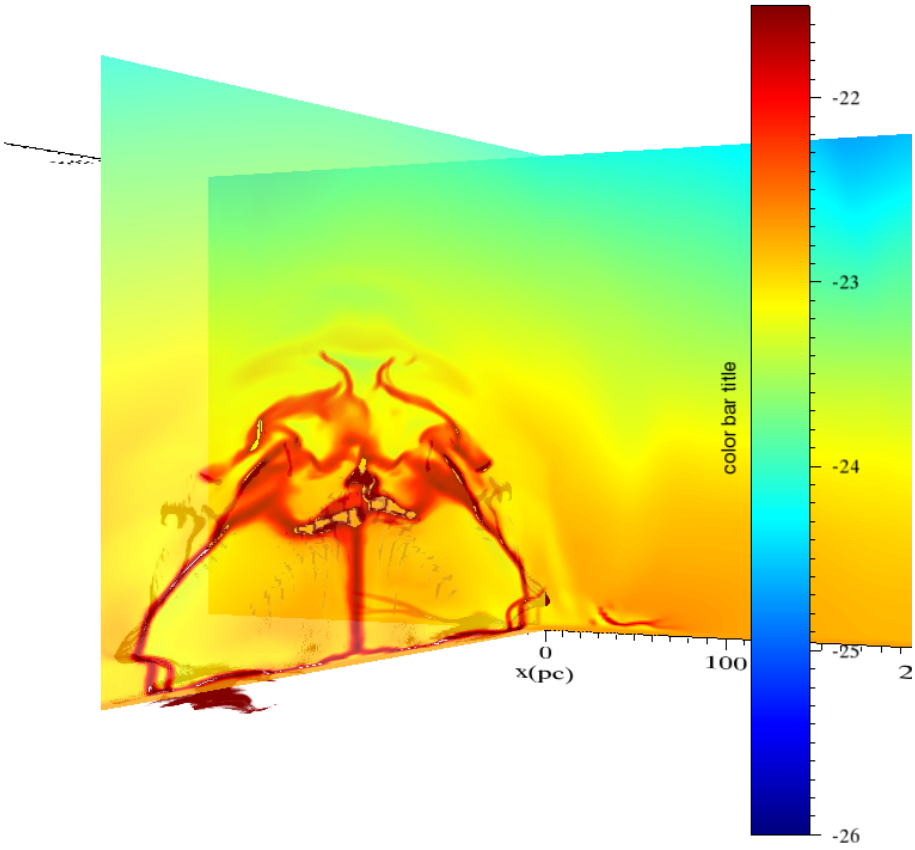

Figure 5.6: Density distribution at $t = 40$ Myrs.

Figure 5.11 compares the observations of the molecular loop1 and loop 2 at the Galactic Center (Fukui et al. 2006) and the p-v diagram obtained by 3D MHD simulation. The velocity gradient along the loop is 30 km/s per 100 pc in observation, which is 5 times larger than numerical results (15 km/s per 250 pc = 6 km/s per 100pc). The velocity dispersion around the foot points of the magnetic loops is 40-80 km/s in observation, which is 3-5 times larger than that of numerical results ($\sim$ 15 km/s). This discrepancy can be due to the smaller potential difference adopted in this 3D model. The potential difference between z =0 and z =200pc corresponds to 17 km/s in this model, meanwhile the difference is 46 km/s at at $R = 1$ kpc.

The total mass of the dense filament obtained by three-dimensional simulation is 4 $\times 10^5$ solar mass, which is comparable to that of the total mass estimated by Torii et al. (2011) for loop 1 and loop 2.

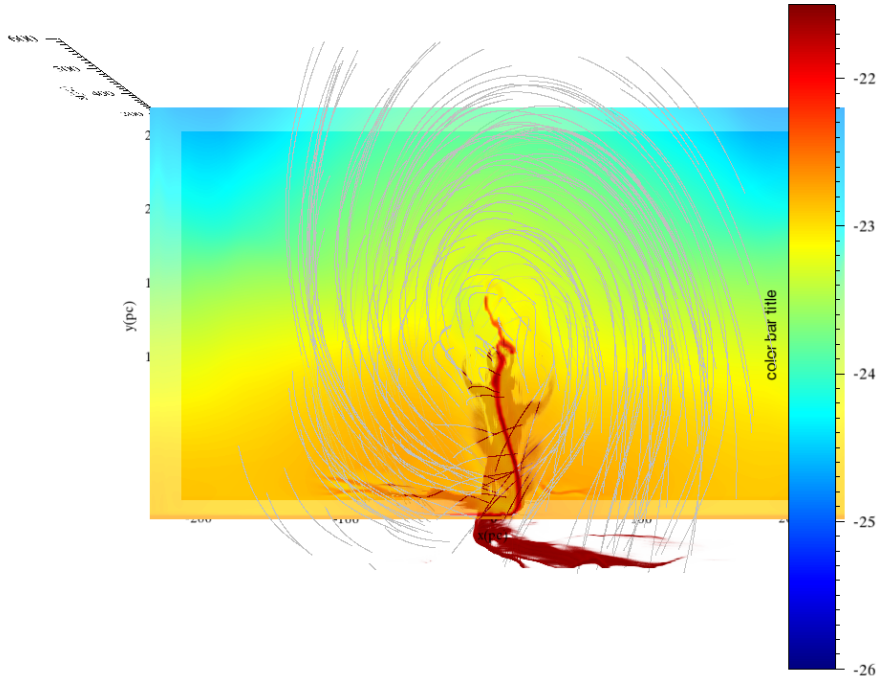

Figure 5.7: Density distribution at $t = 40$ Myrs in $x - z$ plane.

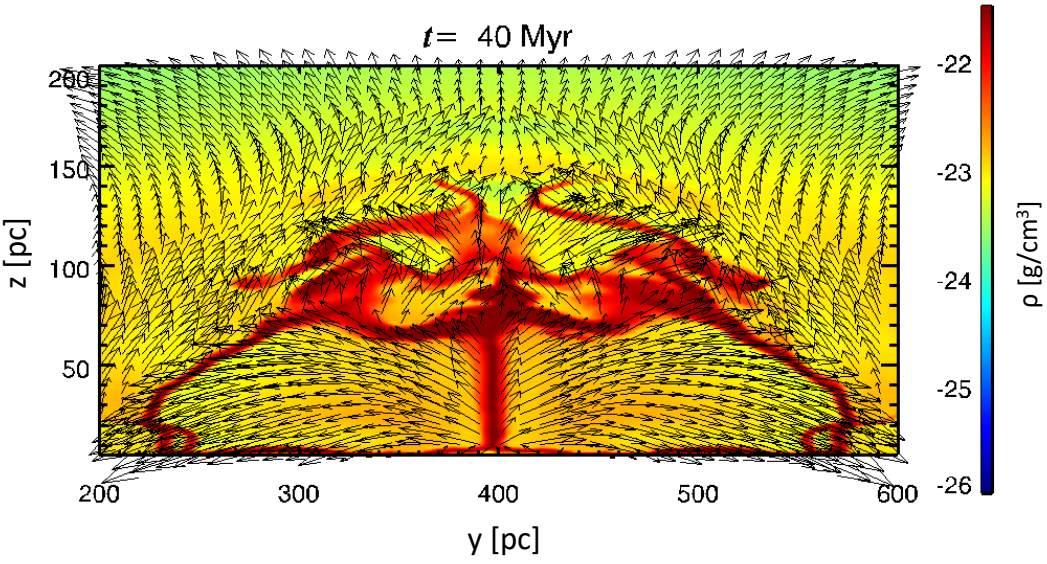

Figure 5.8: Density distribution (color) and velocity (vector) at $x = 0$ pc and $t = 40$ Myrs.

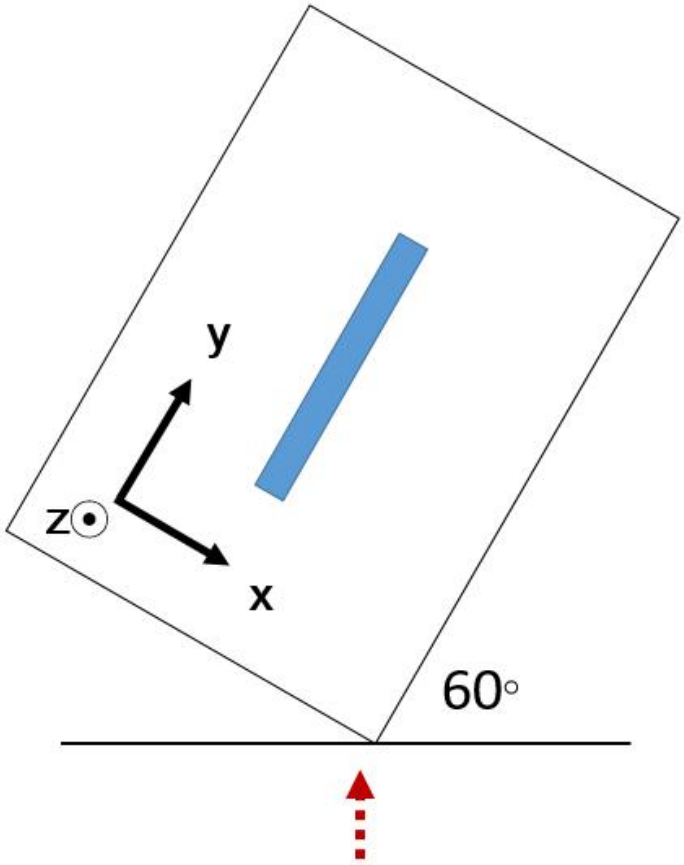

Figure 5.9: Schematic picture showing the angle between the line of sight and the longitudinal direction of the magnetic loop.

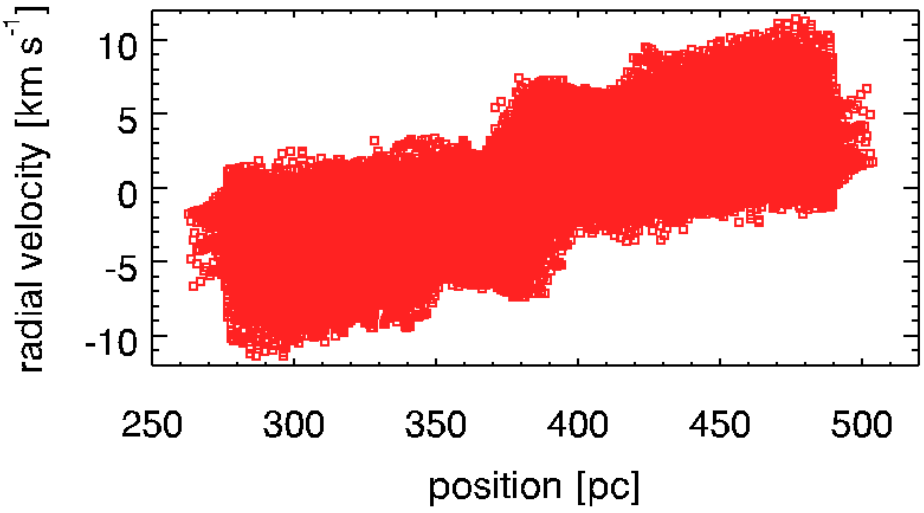

Figure 5.10: Position-velocity diagram obtained from the three-dimensional simulation ($R = 8.5$ kpc, $\Gamma = 10 \times 10^{-26}$ erg s^{-1}). The horizontal axis shows the position projected to the plane perpendicular to the line of sight. The vertical axis is the line of sight velocity. .

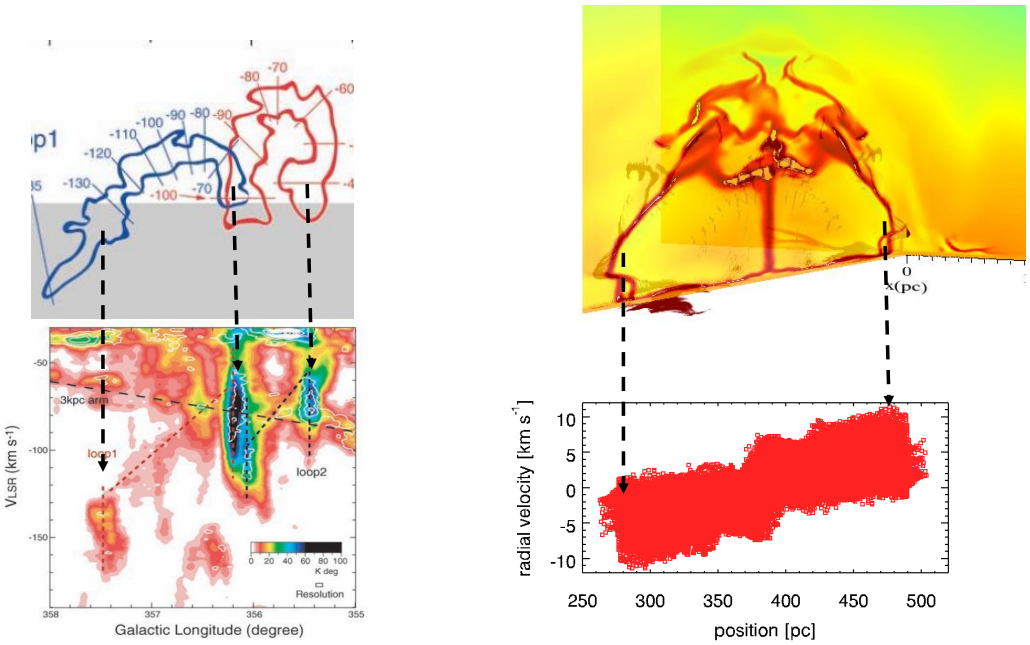

Figure 5.11: Position-velocity diagrams obtained byobservations of Galactic Center molecular loops (left) and by 3D simulation (right).

5.3 Numerical Results for $R = 1$ kpc

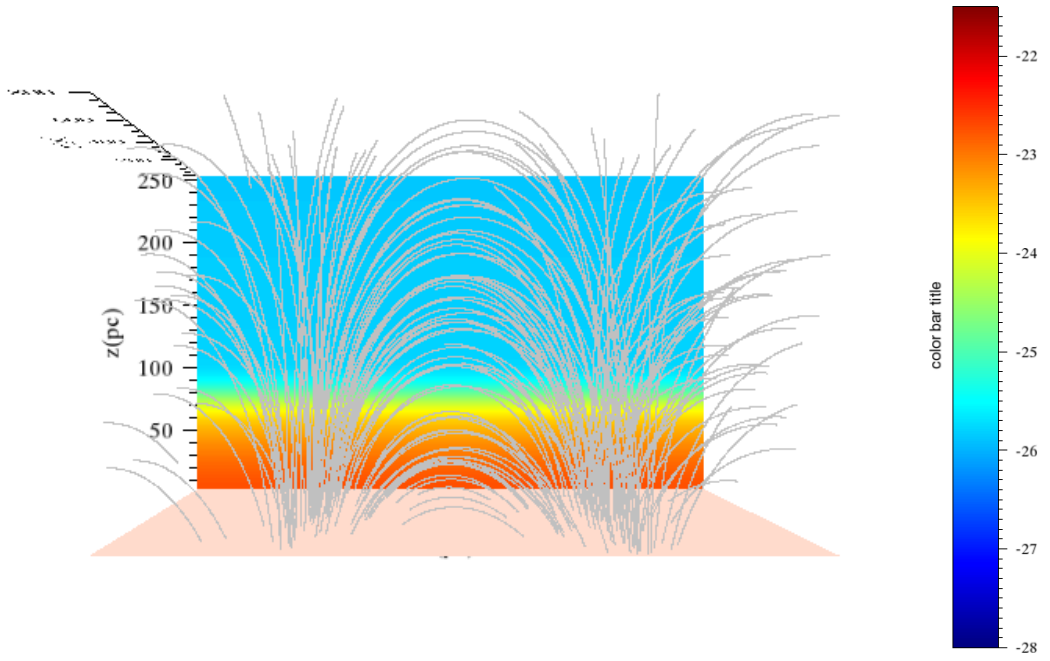

Figure 5.12: Density distribution (color) and magnetic field lines (solid curves) at the initial state of three-dimensional simulations.

In this section, we present the results of a three-dimensional simulation at $R = 1$ kpc. We consider a local part of the disk and take x, y coordinate as horizontal direction, and z-coordinate in vertical direction. Figure 5.12 shows the initial state. We set $\rho(z = 5$ pc$) = 1.8 \times 10^{-22}$ g/cm^3 and $P(z = 5$ pc$) = 9.3 \times 10^{-12}$ dyn/cm^2 ($T(z = 5$ pc$) \sim 6000$ K). Gravitational potential is the Miyamoto-Nagai potential modified by Sofue (1996). The initial state is a hydrostatic atmosphere with force free magnetic fields. They are expressed as follows:

$$B_x = -\left(\frac{2L_a}{\pi H_m}\right) B_a \cos\left(\frac{\pi}{2L_a}x\right) \exp\left(-\frac{z}{H_m}\right) \tag{5.10}$$

$$B_y = \sqrt{1 - \left(\frac{2L_a}{\pi H_m}\right)^2}\, B_a \cos\left(\frac{\pi}{2L_a}x\right) \exp\left(-\frac{z}{H_m}\right) \tag{5.11}$$

$$B_z = B_a \sin\left(\frac{\pi}{2L_a}x\right) \exp\left(-\frac{z}{H_m}\right) \tag{5.12}$$

Here $H_{\rm m} = 80$ pc is magnetic scale height, and $L_{\rm a} = 99$ pc is the half length of the magnetic arcade. The plasma β ($= P_{\rm gas}/P_{\rm mag}$) is assumed to be $\beta = 0.2$ at bottom of the simulation area ($B_a = 3.6$ x 10^{-5} G). The same cooling/heating rate is as section 5.1 is adopted. We adopt Cartesian box covering -198 pc $< x <$ 198 pc, 0 pc $< y <$ 800 pc

and 5 pc $< z <$ 1310 pc. In this three dimensional simulation, we assumed shear (v_y) motions depending on y. They are imposed at foot points of magnetic arch as follows :

$$v_y = \begin{cases} -v_0(y) \sin\left(\frac{\pi x}{L_a}\right) & |x| < L_a \\ 0 & \text{otherwise} \end{cases} \tag{5.13}$$

$$v_z = 0 \tag{5.14}$$

$$v_0(y) = \begin{cases} v_{00} - \frac{1}{3} v_{00} \cos\left(\frac{2\pi(y - 200\text{pc})}{400\text{pc}}\right) & 200 \text{ pc} < y < 600 \text{ pc} \\ \frac{2}{3} v_{00} & \text{otherwise} \end{cases} \tag{5.15}$$

Here v_{00} is 6 km/s. Boundary conditions in x-direction and z-direction are the same as two-dimensional simulation model GA in Chapter 4 and we applied periodic boundary condition in y-direction. The mesh size is $\Delta x = 1$ pc when $|x| < 10$ pc. When $|x| > 10$ pc, Δx increases by 5 % at each mesh point up to $\Delta x = 2$ pc. The mesh size is $\Delta z =$ 1 pc when $|z| < 400$ pc and gradually increases by 5 % at each mesh point up to $\Delta z =$ 4 pc when $z > 400$ pc. Uniform mesh with mesh size $\Delta y = 2$ pc is used for y-direction. We adopted the same numerical method as reported in section 5.1

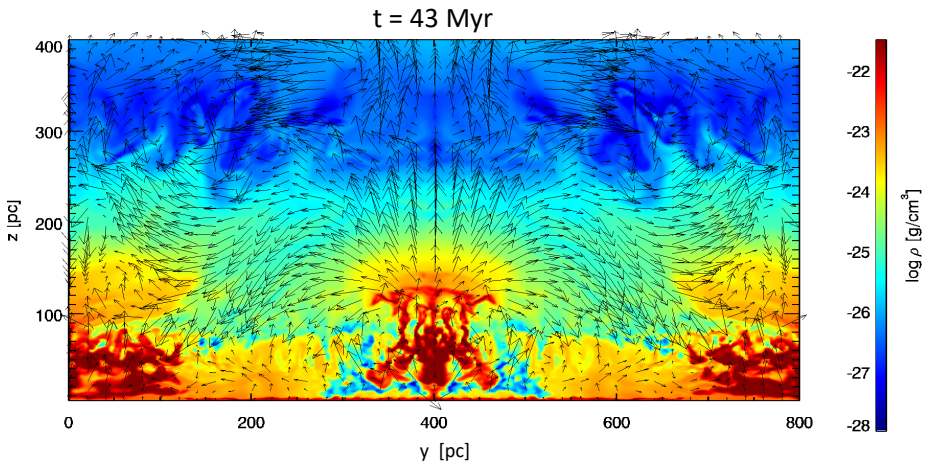

Figure 5.13: Density distribution (color) and velocity (vector) at $x = 0$ pc and $t = 43$ Myrs.

Figure 5.13 shows the density and velocity distribution in $y - z$ plane at $t = 43$ Myrs. In the regions 100 pc $< y <$ 300 pc, and 500 pc $< y <$ 700 pc, the material shows downflow with speed greater than 20 km s^{-1}. Since this speed exceeds the sound speed of the warm gas, shock waves are formed and gas accumulates at the footpoints. In

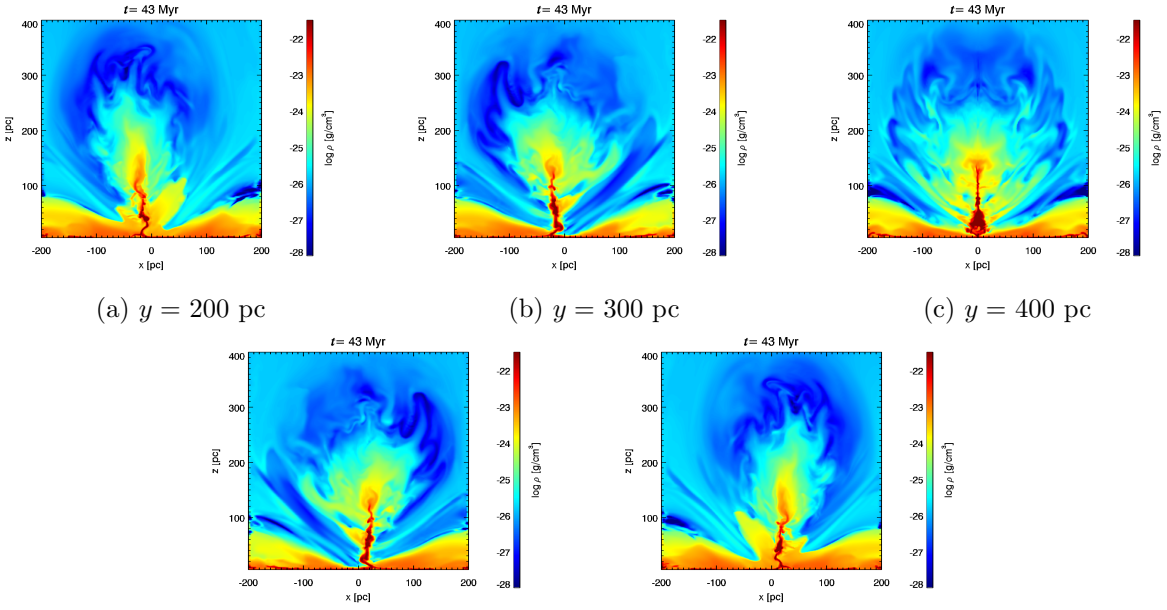

(a) $y = 200$ pc (b) $y = 300$ pc (c) $y = 400$ pc

(d) $y = 500$ pc (e) $y = 600$ pc

Figure 5.14: Density distribution (color) of $x - z$ plane at $y = 200$,300 ,400, 500, and 600 pc.

$y - z$ cross section at $x = 0$ pc, the heavy filament at 300 pc $< y <$ 500 pc seems to be truncated because the dense filament is twisted by Coriolis force. Figure 5.14 shows the density distributions in $x - z$ plane at different y positions. The dense filament is inclined from the $y - z$ plane at $x = 0$. Figure 5.15 and 5.16 shows the three-dimensional density distribution of dense gas at $t = 43$ Myr observed from different lines of sight. In figure 5.15, the magnetic field lines projected on the $x - z$ plane and the density distribution at $t = 43$ Myr are shown. A rope-like structure of magnetic field lines can be identified. Furthermore, dense gas accumulated in lower half of the flux rope around $x = 0$. Figure 5.16 shows that the dense region ($\rho > 10^{-22.5}$ g cm^{-3}) shown by red part shows loop-like structure.

Figure 5.17 shows the $p - v$ diagram plotted by using the line of sight velocity. The direction of line of sight is assumed the same as that in figure 5.9. The velocity dispersion of the dense filament denoted by red symbols is $\sim$ 30 km s^{-1}. The velocity gradient appears around the loop top (350 $< y <$ 450 pc) but it is not clear in other region. This is partly because the large v_x velocity partly cancels v_y when the loop is observed from this direction (see figures 5.18 and 5.19). However, figure 5.19 indicates that the velocity gradient along the dense loop is 20 km s^{-1} per 200 pc, which is twice as large as that for

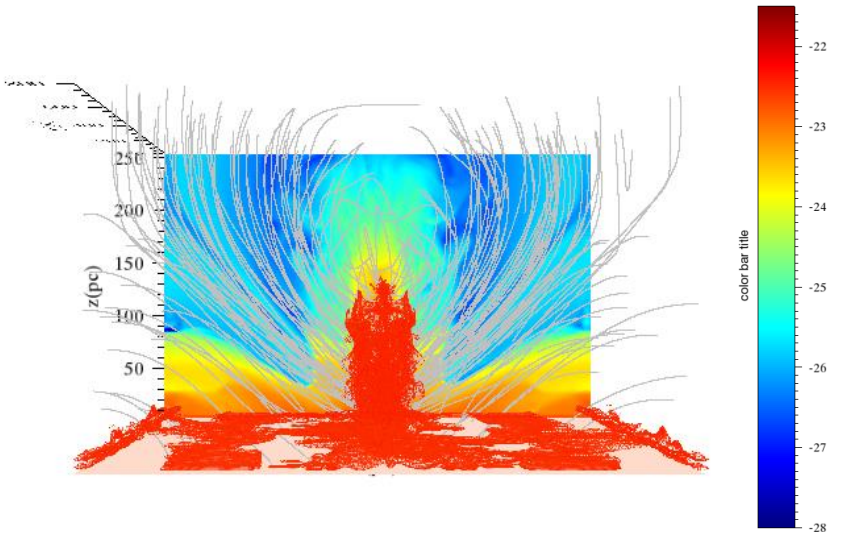

Figure 5.15: Density distribution (color) and magnetic field lines (solid curves) at $t = 43$ Myrs. Red region shows dense gas with $\rho > 10^{-22.5}$ g cm^{-3}.

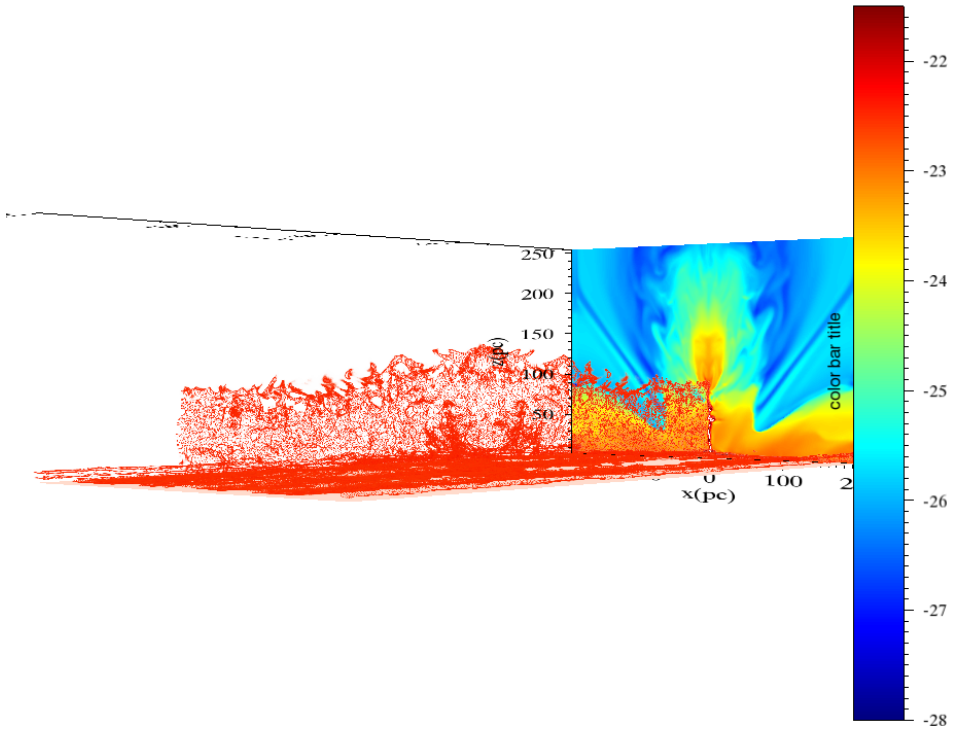

Figure 5.16: Density distribution (color) at $t = 43$ Myrs. Red region shows dense gas with $\rho > 10^{-22.5}$ g cm^{-3}.

a model at $R = 8.5$ kpc.

The total mass of the dense filament ($z > 50$ pc) obtained by three-dimensional

simulation is $\sim 5 \times 10^5$ solar mass, which is comparable to that of the total mass estimated by Torii et al. (2011) for loops 1 and 2.

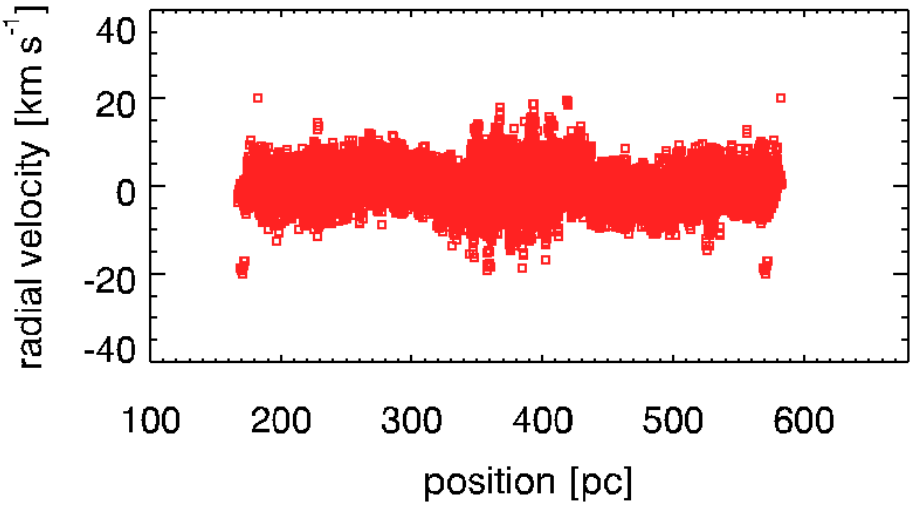

Figure 5.17: Position-velocity diagram obtained from the three-dimensional simulation ($R = 1$ kpc, $\Gamma = 10 \times 10^{-26}$ erg s^{-1}). The horizontal axis shows the position projected to the plane perpendicular to the line of sight. The vertical axis is the line of sight velocity. Red symbols show the position and velocity of the region where $\rho > 10^{-23.5}$ g cm^{-3} and $T < 500$ K at $z = 50$ - 200 pc.

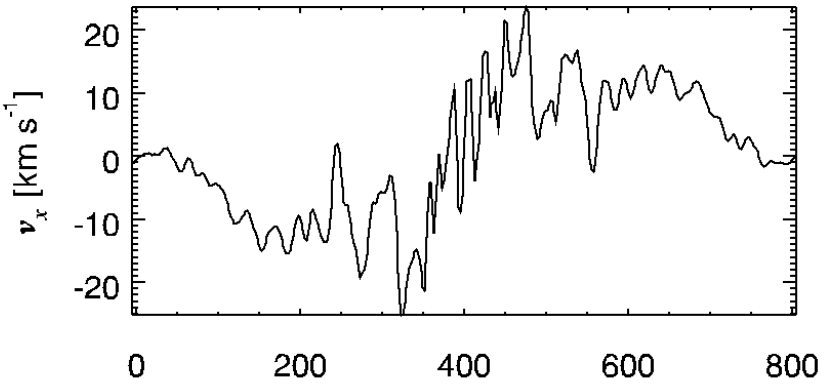

Figure 5.18: Distribution pf v_x at $x = 0$, $z = 100$ pc.

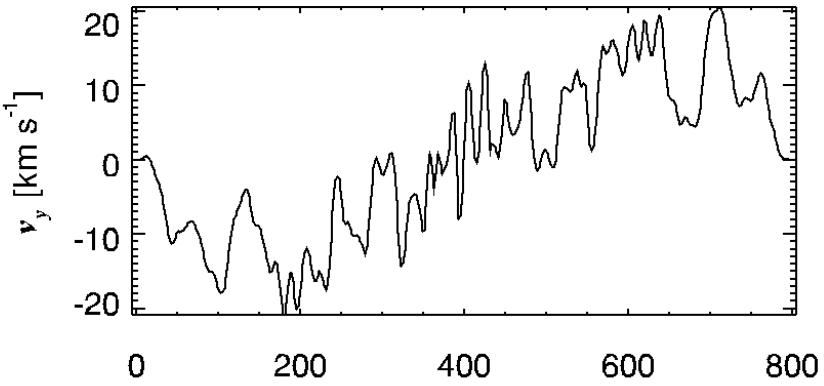

Figure 5.19: Distribution pf v_y at $x = 0$, $z = 100$ pc.

Chapter 6

Summary and Discussion

In this thesis, we have shown through two- and three-dimensional MHD simulations that dense, cold ($T < 500$ K) loop-like filaments (galactic prominences) can be formed at a height of $100 - 200$ pc above the galactic plane. These filaments are similar to solar prominences because a low temperature, dense gas is sustained against gravity in a warm interstellar medium whose temperature is $10 - 100$ times higher than that of the filament. Galactic prominences are distinct from high latitude molecular clouds because they are longer (> 200 pc), have a line of sight velocity gradient along the filament, and show large velocity dispersion around their footpoints. These observed features of galactic prominences are consistent with those of the molecular loops that were observed by surveys of the molecular gas in the galactic central region using the NANTEN telescope (Fukui et al. 2006).

We have conducted a series of numerical simulations starting with a plane-parallel, hydrostatic disk with force-free magnetic arcade. We have studied the evolution of these magnetic loops by imposing footpoint motions at the lower boundary, 5 pc above the galactic plane, to simulate magnetic turbulence in the disk driven by magneto-rotational instability (MRI). Based on these simulations, we have observed the following:

(1) When footpoints of magnetic loops move with a velocity of $4 - 8$ km s^{-1}, the loops are inflated by magnetic pressure and by forming current sheets around their midpoints. When the density of the warm interstellar gas that has accumulated in this region exceeds the threshold for the onset of the cooling instability, a cool, dense, vertical filament of the cold neutral medium (CNM) is formed. The converging flow toward this region triggers magnetic reconnection and the ejection of the flux rope. As the medium in the flux rope

falls down along the poloidal magnetic field lines, they accumulate around the bottom of the rope, where the warm medium is converted to the CNM by cooling. The mass of the dense filament increases with time and can exceed 10^5 $M_\odot$ when its length is 600 pc. These results have been published in the Astrophysical Journal (Peng et al. 2017).

(2) We have studied the effects of galactic rotation by conducting simulations in a frame that is co-rotated with the disk by taking the Coriolis force into account. Since the galactic rotation produces compressible motion along the inclined magnetic field lines due to shear motions at the footpoints of the magnetic loop and due to the accumulation of the warm medium around the loop's midpoint, the medium is converted to CNM by enhanced cooling. In a fiducial model with plasma $\beta = 0.2$, magnetic reconnection in the current sheet ejected the CNM that was formed along the current sheet due to the cooling instability. The rope's center was higher in this rotating disk model than that in the non-rotating model and was ejected more than 400 pc away from the galactic plane. The CNM that was ejected with the flux rope then falls down along the poloidal magnetic field lines and accumulates around the rope's bottom, forming a dense, cold ($T < 500$ K) filament. As the gas continues to fall, its mass eventually exceeds 10^5 $M_\odot$. The magnetic energy released by magnetic reconnection increases with the initial magnetic field strength and shear velocity. Thus, the maximum height of the filament ejected by magnetic reconnection increases with both initial field strength and shear speed.

(3) Our three-dimensional MHD simulations have revealed that dense, cold ($T < 500$ K) magnetic arcades are formed as CNM accumulates around the bottom of the magnetic flux rope that was formed by the reconnection-condensation mechanism. The CNM's line of sight speed shows a gradient along the loop and has large velocity dispersion. Since the magnetic field supports the dense filament against gravity, the interface between the warm gas and the CNM at the rope's bottom can be subjected to the Rayleigh-Taylor instability. Our numerical results indicate that the filament continues to be supported for 30-40 Myr.

The idea of "Galactic Prominence" was addressed by Morris (2006) and Torii et al. (2010b) to explain the formation of the molecular loops observed in the Galactic central region (Fukui et al. 2006). Fukui et al. explained the observed velocity gradients along these loop and the large velocity dispersion around their footpoint in terms of the

molecular gas sliding along the magnetic loops that were formed by the Parker instability.

We should note, however, that most of the molecular gas that rises with the buoyant magnetic loops then slides down along the loop in several Alfv̂en crossing time of one scale height (e.g., Matsumoto et al. 1988). Since the scale height of the HI disk in the Galactic central region is $\sim$ 15 pc, as indicated by the *Hi-GAL* survey using Herschel satellite, the region at the top of the loop will be evacuated over a time scale of mega-years when the Alfv̂en speed is 15 km s^{-1}. Meanwhile, the time required for the formation of magnetic loops with heights of 150 pc is more than 10 Myr. Therefore, we need to consider in-situ formation of dense, cold filaments.

One possible mechanism for the in-situ formation of molecular gas is the compression of the warm neutral medium by buoyant magnetic loops that are elevated due to Parker instability. However, MHD simulations by Takahashi et al. (2009) showed that the maximum density of the shells formed around the tops of the rising magnetic loops was too small to trigger the cooling instability. During the adiabatic stage of magnetic loop expansion, the maximum density at the loop top only increases by a factor of four when the specific heat ratio is γ =5/3. Since the density of the interstellar medium at a height of 100 pc above the galactic plane is far lower than the threshold for the onset of the cooling instability, cooling cannot form dense shells.

In this thesis, we have applied the in-situ solar prominences formation model of Kaneko & Yokoyama (2015) to the galactic gas disks and demonstrated that dense, cold filaments can be formed by the cooling instabilities. We have used three-dimensional simulations to show that the CNM in the filaments slides down along the longitudinal direction to form a dense loops, which are similar to the molecular loops in the Galactic Center.

Appendix A

Numerical Solver for MHD Equations

In this appendix, we outline the numerical scheme we adopted for simulations in this thesis. The basic equations (2.1)-(2.4) can be written as

$$\frac{\partial \boldsymbol{U}}{\partial t} + \nabla \cdot \boldsymbol{F} = \boldsymbol{S}, \tag{A.1}$$

where $\boldsymbol{U}$ is conserved variables, $\boldsymbol{F}$ is flux, and $\boldsymbol{S}$ is source term. We adopt the finite volume method, in which the conserved variables $\boldsymbol{U}$ at the cell center is updated by using the flux $\boldsymbol{F}$ at cell boundaries. We applied the HLLD scheme (Miyoshi & Kusano 2005) to approximately solve the Riemann problem at the cell surface.

Here we explain the HLLD scheme for one dimensional ideal MHD equations in conservation form

$$\frac{\partial \boldsymbol{U}}{\partial t} + \frac{\partial \boldsymbol{F}}{\partial x} = 0. \tag{A.2}$$

The conserved variables $\boldsymbol{U}$ and the flux $\boldsymbol{F}$ can be written as

$$\boldsymbol{U} = \begin{pmatrix} \rho \\ \rho u \\ \rho v \\ \rho w \\ B_y \\ B_z \\ e \end{pmatrix} \tag{A.3}$$

$$\boldsymbol{F} = \begin{pmatrix} \rho u \\ \rho u^2 + P_T - B_x^2 \\ \rho v u - B_x B_y \\ \rho w u - B_x B_y \\ B_y u - B_x v \\ B_z u - B_x w \\ (e + P_T)u - B_x(uB_x + vB_y + wB_z) \end{pmatrix} \tag{A.4}$$

where $P_T = P + \boldsymbol{B}^2/2$ is total pressure and $e = P/(\gamma - 1) + \rho \boldsymbol{v}^2/2 + \boldsymbol{B}^2/2$ is energy density. The solenoidal condition $\nabla \cdot \boldsymbol{B} = 0$ requires that B_x is constant. The time evolution of conservative variables $\boldsymbol{U}$ can be written as

$$\boldsymbol{U}_i^{n+1} = \boldsymbol{U}_i^n - \frac{\Delta t}{\Delta x}(\boldsymbol{F}_{i+1/2} - \boldsymbol{F}_{i-1/2}), \tag{A.5}$$

where i and n denote the cell number and the time step, respectively, and $\boldsymbol{F}_{i+1/2}$ and $\boldsymbol{F}_{i-1/2}$ are numerical flux at the cell surface. We compute $\boldsymbol{F}_{i+1/2}$ by HLLD method. By integrating equation (A.2) from x_i to $x_{i+1/2}$, we obtain

$$\boldsymbol{F}_{i+1/2} = \boldsymbol{F}_i - \frac{1}{\Delta t}\int_{x_i}^{x_{i+1/2}} \boldsymbol{R}(\frac{x - x_{i+1/2}}{\Delta t}; \boldsymbol{U}_L^n, \boldsymbol{U}_R^n)dx + \frac{x_{i+1/2} - x_i}{\Delta t}\boldsymbol{U}_i^n. \tag{A.6}$$

Here $\boldsymbol{R}$ indicates the approximate solution of the Riemann problem. In the HLLD scheme, fast waves, Alfvén waves and the entropy wave are considered. The Riemann problem at the cell surface is solved approximately by using the four states $\boldsymbol{U}_L^*$, $\boldsymbol{U}_L^{**}$,$\boldsymbol{U}_R^*$ and $\boldsymbol{U}_R^{**}$ of conservative variables (see figure A.1). Equations (A.6) can be rewritten as follows:

$$\boldsymbol{F}_{i+1/2} = \begin{cases} \boldsymbol{F}_L & S_L > 0 \\ \boldsymbol{F}_L + S_L(\boldsymbol{U}_L^* - \boldsymbol{U}_L) & S_L \le 0 \le S_L^* \\ \boldsymbol{F}_L + S_L(\boldsymbol{U}_L^* - \boldsymbol{U}_L) + S_L^*(\boldsymbol{U}_L^{**} - \boldsymbol{U}_L^*) & S_L^* \le 0 \le S_M \\ \boldsymbol{F}_R + S_R(\boldsymbol{U}_R^* - \boldsymbol{U}_L) + S_L^*(\boldsymbol{U}_L^{**} - \boldsymbol{U}_L^*) & S_M \le 0 \le S_R^* \\ \boldsymbol{F}_R + S_R(\boldsymbol{U}_R^* - \boldsymbol{U}_L) & S_R^* \le 0 \le S_R \\ \boldsymbol{F}_R & S_R < 0 \end{cases} \tag{A.7}$$

Here, S_L and S_R are speeds of fast waves, S_L^* and S_R^* are speeds of Alfvén waves and S_M is the speed of the entropy wave.

The cell surface values $\boldsymbol{U}_L^n$ and $\boldsymbol{U}_R^n$ are obtained by interpolation from the values at the cell center, and restricting them to satisfy the TVD condition. In the code we

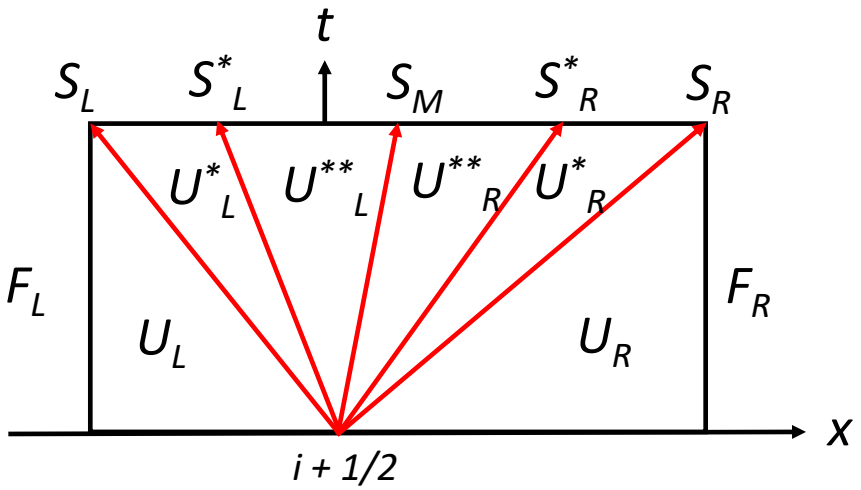

Figure A.1: Characteristics of the five waves used in the HLLD scheme to compute the numerical flux at the cell surface at $x = x_{i+1/2}$.

used in chapter 2, 3, and 5, we applied the MUSCL scheme (van Leer 1979) for the calculation of the cell surface values. In the CANS+ code used in simulations in chapter 4, MP5 scheme (Suresh & Huynh 1997) is applied to compute the cell surface values with 5th order spacial accuracy. The time integration is carried out by using the third order Runge-Kutta scheme e (Suresh & Huynh 1997; Gottlieb & Shu 1998). The source term is evaluated at each Runge-Kutta step. See Matsumoto et al. (2016) for details of the CANS+ code.

Appendix B

Propagation of MHD Waves in Rotating Disks

In this appendix, we derive the dispersion relations for MHD waves in rotating plasma and demonstrate that density enhancements can be produced by transverse motions at the footpoints of magnetic loops. We consider uniform plasma threaded by uniform magnetic field $\boldsymbol{B}_0$. We neglect gravity and assume uniform rotation with angular velocity $\boldsymbol{\Omega}$. At the unperturbed state, we assume uniform plasma with $\rho_0 = \text{const.}$, $P_0 = \text{const.}$, $\boldsymbol{B}_0 = B_0 \boldsymbol{e}_{\parallel}$, and $\boldsymbol{v}_0 = 0$

By applying perturbations $\rho = \rho_0 + \delta\rho$, $\boldsymbol{v} = 0 + \boldsymbol{v}$, $P = P_0 + \delta P$, $\boldsymbol{B} = \boldsymbol{B}_0 + \delta\boldsymbol{B}$ We linearlize the ideal MHD equations with Coriolis force and obtain

$$\frac{\partial \delta\rho}{\partial t} + \nabla \cdot (\rho_0 \boldsymbol{v}) = 0, \tag{B.1}$$

$$\rho_0 \frac{\partial \boldsymbol{v}}{\partial t} = -\nabla(\delta P + \frac{\boldsymbol{B}_0 \cdot \delta\boldsymbol{B}}{4\pi}) + \frac{1}{4\pi}(\boldsymbol{B}_0 \cdot \nabla)\delta\boldsymbol{B} + 2\rho_0 \boldsymbol{v} \times \boldsymbol{\Omega}, \tag{B.2}$$

$$\frac{\partial \delta B}{\partial t} = \nabla \times (\boldsymbol{v} \times \boldsymbol{B}_0). \tag{B.3}$$

Assuming adiabatic perturbation, δP is related to $\delta\rho$ as

$$\delta P = c_s^2 \delta\rho, \tag{B.4}$$

where c_s is sound speed.

By introducing a displacement vector $\boldsymbol{\xi}$ defined by $\boldsymbol{v} = \dfrac{\partial \boldsymbol{\xi}}{\partial t}$, the density perturbation can be expressed by using the equation of continuity as $\delta\rho = -\nabla \cdot (\rho_0 \boldsymbol{\xi})$.

The equation of motion can be written as

$$\rho_0 \frac{\partial^2 \boldsymbol{\xi}}{\partial t^2} = \nabla \left[c_s^2 \nabla \cdot (\rho_0 \boldsymbol{\xi}) \right] - \nabla \left(\frac{\boldsymbol{B}_0 \cdot \delta\boldsymbol{B}}{4\pi} \right) + \frac{1}{4\pi}(\boldsymbol{B}_0 \cdot \nabla)\delta\boldsymbol{B} + 2\rho_0 \frac{\partial \boldsymbol{\xi}}{\partial t} \times \boldsymbol{\Omega} \tag{B.5}$$

and the magnetic field perturbation $\delta\boldsymbol{B}$ can be obtained from the induction equation as

$$\delta\boldsymbol{B} = \nabla \times (\boldsymbol{\xi} \times \boldsymbol{B}_0) = (\boldsymbol{B}_0 \cdot \nabla)\boldsymbol{\xi} - \boldsymbol{B}_0(\nabla \cdot \boldsymbol{\xi}). \tag{B.6}$$

Assuming the plane wave perturbation $\boldsymbol{\xi} \propto \exp[i(\omega t - \boldsymbol{k} \cdot \boldsymbol{r})]$, we obtain

$$\delta\boldsymbol{B} = -(i\boldsymbol{k} \cdot \boldsymbol{B}_0)\boldsymbol{\xi} + \boldsymbol{B}_0(i\boldsymbol{k} \cdot \boldsymbol{\xi}) = -ik_\parallel B_0 \boldsymbol{\xi} + iB_0(\boldsymbol{k} \cdot \boldsymbol{\xi})\boldsymbol{e}_\parallel. \tag{B.7}$$

After some algebra, the equation of motion can be written as

$$\omega^2\boldsymbol{\xi} = c_s^2\boldsymbol{k}(\boldsymbol{k} \cdot \boldsymbol{\xi}) - v_A^2\boldsymbol{k}(k_\parallel\xi_\parallel - \boldsymbol{k} \cdot \boldsymbol{\xi}) + k_\parallel v_A^2\left[k_\parallel\boldsymbol{\xi} - (\boldsymbol{k} \cdot \boldsymbol{\xi})\boldsymbol{e}_\parallel\right] - 2i\omega\boldsymbol{\xi} \times \boldsymbol{\Omega} \tag{B.8}$$

where v_A is Alfvén speed.

We adopt a Cartesian coordinate in which the unit vectors are ($\boldsymbol{e}_\parallel$, $\boldsymbol{e}_y$, $\boldsymbol{e}_\perp$), where $\boldsymbol{e}_y$ is perpendicular to the plane containing $\boldsymbol{B}_0$ and Ω, and $\boldsymbol{e}_\perp = \boldsymbol{e}_\parallel \times \boldsymbol{e}_y$. In this coordinate, $\boldsymbol{\Omega} = \Omega_\parallel\boldsymbol{e}_\parallel + \Omega_\perp\boldsymbol{e}_\perp$.

When we consider waves propagating along unperturbed magnetic field lines, we can simplify the linearlized equations by setting $k_y = k_\perp = 0$. Since $\boldsymbol{k} \cdot \boldsymbol{\xi} = k_\parallel\xi_\parallel$, we obtain

$$\omega^2\boldsymbol{\xi} = c_s^2 k_\parallel\xi_\parallel\boldsymbol{k} + k_\parallel^2 v_A^2(\xi_y\boldsymbol{e}_y + \xi_\perp\boldsymbol{e}_\perp) - 2i\omega\boldsymbol{\xi} \times \boldsymbol{\Omega}. \tag{B.9}$$

The components are

$$\omega^2\xi_\parallel = c_s^2 k_\parallel^2\xi_\parallel - 2i\omega\xi_y\Omega_\perp, \tag{B.10}$$

$$\omega^2\xi_y = k_\parallel^2 v_A^2\xi_y - 2i\omega(\xi_\perp\Omega_\parallel - \xi_\parallel\Omega_\perp), \tag{B.11}$$

$$\omega^2\xi_\perp = k_\parallel^2 v_A^2\xi_\perp + 2i\omega\xi_y\Omega_\parallel. \tag{B.12}$$

These equations can be expressed in Matrix form as

$$\begin{pmatrix} \omega^2 - k_\parallel^2 c_s^2 & 2i\omega\Omega_\perp & 0 \\ -2i\omega\Omega_\perp & \omega^2 - k_\parallel^2 v_A^2 & 2i\omega\Omega_\parallel \\ 0 & -2i\omega\Omega_\parallel & \omega^2 - k_\parallel^2 v_A^2 \end{pmatrix} \begin{pmatrix} \xi_\parallel \\ \xi_y \\ \xi_\perp \end{pmatrix} = 0. \tag{B.13}$$

The dispersion relation can be obtained by the condition that the determinant of the matrix is zero as

$$(\omega^2 - k_\parallel^2 c_s^2)(\omega^2 - k_\parallel^2 v_A^2)^2 = 4\omega^2\left[\Omega_\parallel^2(\omega^2 - k_\parallel^2 c_s^2) + \Omega_\perp^2(\omega^2 - k_\parallel^2 v_A^2)\right]. \tag{B.14}$$

When the unperturbed magnetic field is parallel to the rotation axis (i.e., $\Omega_\perp = 0$), $(\omega^2 - k_\parallel^2 c_s^2)[(\omega^2 - k_\parallel^2 v_A^2)^2 - 4\omega^2\Omega_\parallel^2] = 0$. The Alfvén wave is modified by rotation but

the sound wave is not modified. When the unperturbed magnetic field is perpendicular to the rotation axis (i.e., $\Omega_{\parallel} = 0$), $(\omega^2 - k_{\parallel}^2 v_A^2)[(\omega^2 - k_{\parallel}^2 c_s^2)(\omega^2 - k_{\parallel}^2 v_A^2) - 4\omega^2 \Omega_{\perp}^2)] = 0$. Both slow wave and fast wave are modified by rotation. We also note that since $(\omega^2 - k_{\parallel}^2 c_s^2)\xi_{\parallel} + 2i\omega\Omega_{\perp}\xi_y = 0$, compressible motion $\xi_{\parallel} \neq 0$ can be produced from Alfvénic perturbation ξ_y when $\Omega_{\perp} \neq 0$.

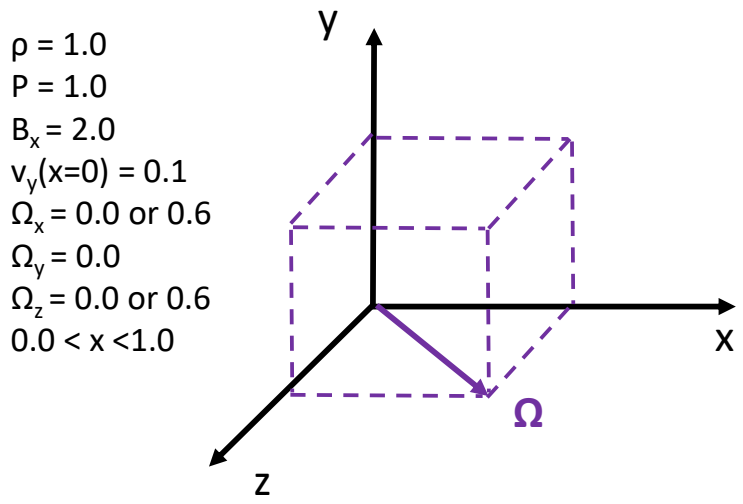

Figure B.1: Initial state and coordinates for one-dimensional MHD simulation of wave propagation in rotating disks.

We carried out one-dimensional simulation to study how the Coriolis force affects the wave propagation. Figure B.1 schematically shows the initial state and coordinate. We neglect gravity and assume uniform plasma at the unperturbed state. The initial magnetic field is assumed to be parallel to the x-axis and we simulate the propagation of waves in x-direction. The plasma is assumed to be rotating with angular speed Ω. We assume that the rotation axis is inclined from the x-axis. We excite an Alfvén wave by imposing the transverse velocity v_y at $x = 0$ perpendicular to the initial magnetic field line. The propagation of the wave is simulated by applying the MHD code based on the MP5 scheme. We used uniform grids with Δx =0.00195. Free boundary condition is applied at $x = 0$ except v_y which is fixed. The specific heat ratio is assumed to be $\gamma = 5/3$.

Figure B.2 shows the results of the simulation of the wave propagation with/without

the Coriolis force. The upper panels and the lower panels show the distribution of density and v_x, respectively, at $t = 0.4$. When $\Omega = 0$ the Alfvén wave produced by the finite amplitude transverse motion at x =0 excites a fast magnetosonic wave and a slow magnetosonic wave by nonlinear coupling. Since these magnetosonic waves are compressible, density is enhanced between these waves. Numerical results indicate that the density enhancement around the slow magnetosonic wave is larger for the model with Coriolis force. We also confirmed that the density enhancement is larger for a model in which the rotation axis is inclined from the direction of the initial magnetic field. This is consistent with the linear analysis that compressible motion is induced from ξ_y by $\Omega_\perp$.

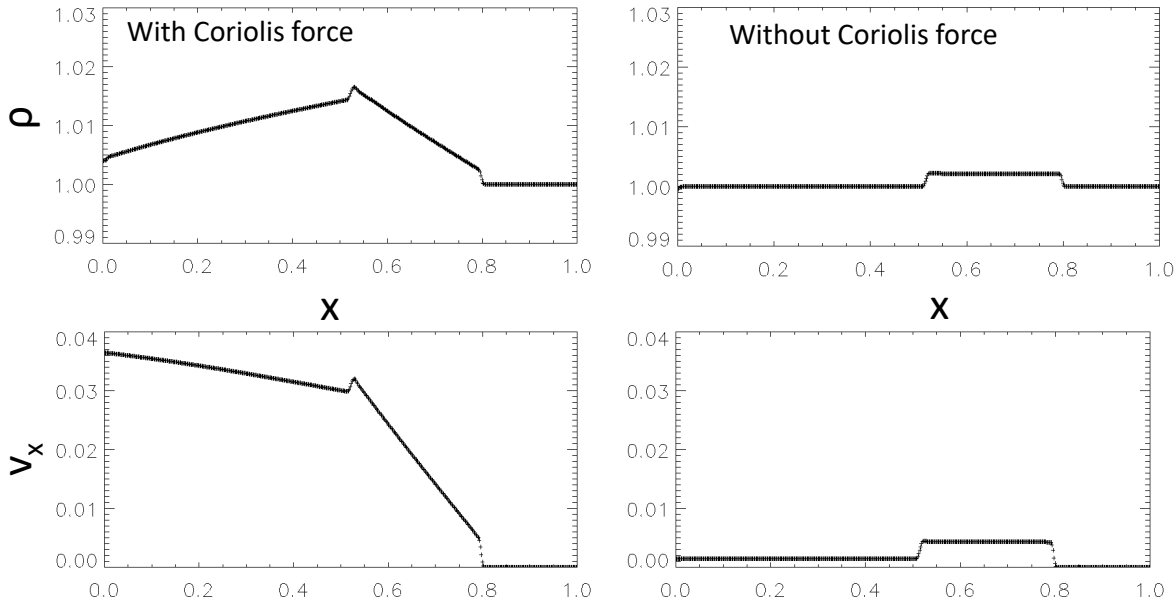

Figure B.2: Results of one-dimensional MHD simulation of wave progagation excited by the transverse motion v_y at $x = 0$. Top panels show the density distribution, and the bottom panels show the distribution of v_x at $t = 0.4$.

Appendix C

Stability of Dense Filaments

Figure C.1 shows the density distribution at $t = 150$ Myrs for Model A_c. Dense filament is formed around x=0 and 150 pc $< z <$ 250 pc. The thickness of the filament d is $d \sim$ 10 pc.

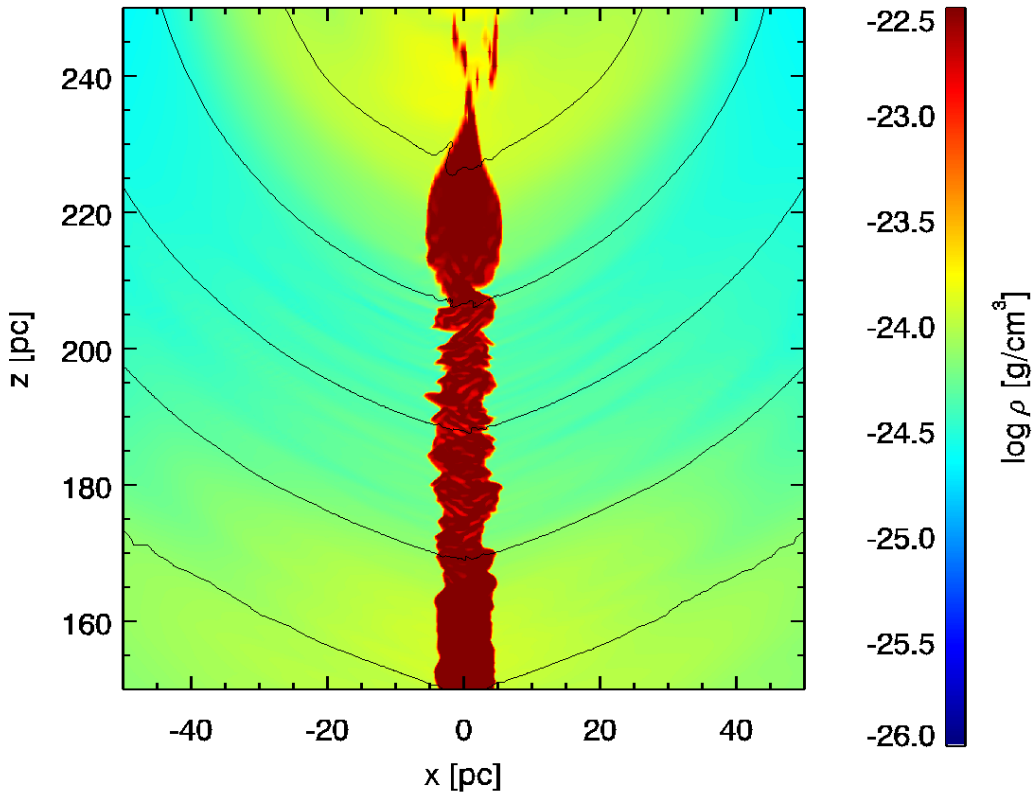

Figure C.1: Zoom in region of dense filament of model A_c.

Let us discuss the thickness and stability of the dense filament. When the filament is uniform with density ρ_f temperature T_f, and column density σ, and is in pressure

equilibrium with the ambient medium with pressure P_0, the thickness of the filament can be expressed as $d = \sigma/\rho_f \propto \sigma T_f/P_0$. When σ and P_0 are fixed, the thickness decreases as T_f decreases. When the cutoff temperature is lower, the filament can be thinner. Since the column density of the filament increases as the gas infalls along the closed magnetic loops in the flux rope, the thickness d increases with time.

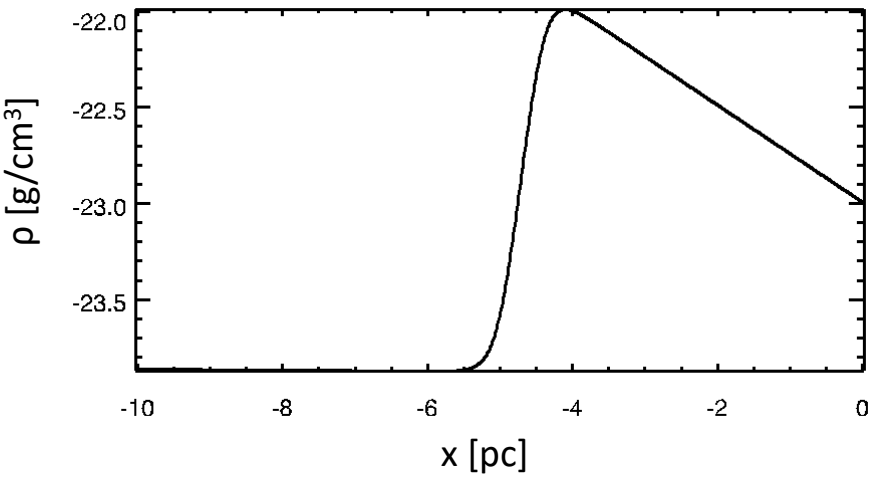

Figure C.2: Initial density distribution for test simulation of the formation of wiggled filaments due to initial v_y and Coriolis force .

When Coriolis force is taken into account, the dense filament can subject to the Rayleigh-Taylor instability when the interface between the filament and the ambient gas moves in y-direction. When the density is higher in $x > x_L$, and the gas has the velocity in $-y$ direction, the Coriolis force points toward the $-x$ direction. Since this force plays a role of gravity in $-x$ direction, it drives Rayleigh-Taylor instability. This can be the origin of the wiggles of the dense filament in Figure C.1 at $t = 150$ Myrs.

To demonstrate the growth of such wiggles, we carried out simulations of the nonlinear growth of the instability around the contact discontinuity in rotating fluids. Figure C.2 shows the initial density distribution. We neglect gravity in vertical direction. At the initial state we assume that v_y is uniform and in $-y$ direction. We assume that the rotation vector is in $z-$direction. By assuming hydrostatic balance in x-direction the pressure distribution is obtained by solving the hydrostatic equation (C1).

$$\frac{dP}{dx} = -2\rho v_y \Omega_z \tag{C.1}$$

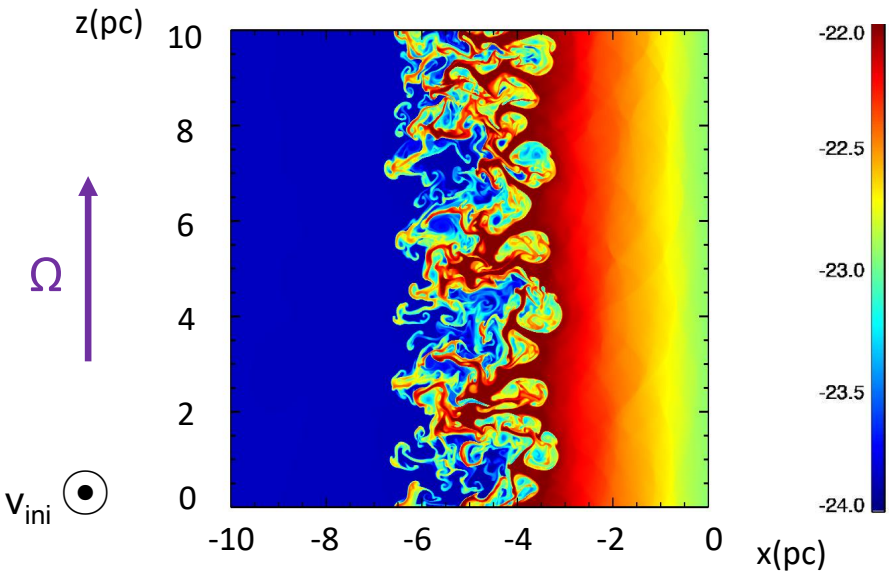

Figure C.3: Density distribution obtained by a two-dimensional simulation of the interface between the ambient medium and dense filament in the presence of initial v_y and Coriolis force .

To initiate the evolution, we imposed a random perturbation for v_z. Figure C.3 shows that the perturbation grows, and that turbulence is generated around the interface. It indicates that when the numerical resolution is sufficiently high, magnetic turbulence develops around the interface between the dense filament and ambient gas. Since the growth time scale of this instability is shorter than the formation time scale of prominence for shorter wavelength perturbation in $z-$direction (i.e., when k_z is large), the thickness of the filament can become larger by this instability.

Reference

[1] Asahina, Y., Ogawa, T., Kawashima, T., et al., 2014, ApJ, 789, 79

[2] Balbus, S. A., Hawley, J. F., 1991, ApJ, 376, 214

[3] Choe, G. S., Lee, L. C., 1996a, ApJ, 472, 360

[4] Choe, G. S., Lee, L. C., 1996b, ApJ, 472, 372

[5] Chou, W., Tajima, T., Matsumoto, R., Shibata, K., 1997 , PASJ, 49, 389

[6] Clemens, D. P., 1985, ApJ, 295, 422

[7] Dedner, A., Kemm, F., Kröner, D., et al., 2002, JCoPh, 175, 645

[8] Field, G. B., Goldsmith, D. W., Habing, H. J., 1969, ApJ, 155, L149

[9] Fujishita, M., Torii, K., Kudo, N., et al., 2009, PASJ, 61, 1039

[10] Fukui, Y., Hayakawa, T., Inoue, T. et al., 2017, arXiv:1701.07129

[11] Fukui, Y., Yamamoto, H., Fujishita, M., et al., 2006, Sci, 314, 106

[12] Gottlieb, S. & Shu, C.-W., 1998, Math. Comput. Am. Math. Soc., 67, 73

[13] Hanasz, M., Otmianowska-Mazur, K., Lesch, H., 2002, A&A, 386, 347

[14] Hawley, J. F.; Gammie, C. F.; Balbus, S. A., 1995, ApJ, 440, 742

[15] Inoue, T., Inutsuka, S., Koyama, H., 2006, ApJ, 652, 1331

[16] Inoue, T., Inutsuka, S., Koyama, H., 2007, ApJL, 658, 99

[17] Inoue, T., Yamazaki, R., Inutsuka, S., 2009, ApJ, 695, 825

[18] Kakiuchi, K., Suzuki, T. K., Fukui, Y. et al., 2017, arXiv:1712.04209

[19] Kassim, Namir. E., Larosa, T. N., Lazio, T. Joseph. W., Hyman, S. D., 1999, The Central Parsecs of the Galaxy, ASP Conference Series, 186, 403

[20] Kaneko, T., Yokoyama, T., 2015, ApJ, 806, 115

[21] Kaneko, T., Yokoyama, T., 2017, ApJ, 845, 12

[22] Karpen, J. T., Antiochos, S. K., Klimchuk, J. A., 2006, ApJ, 637, 531

[23] Kato, Y., Mineshige, S., Shibata, K., 2004, ApJ, 605, 307

[24] Kippenhahn, R., Schlüter, A., 1957, ZAp,43, 36

[25] Koyama, H., Inutsuka, S., 2000, ApJ, 532, 980

[26] Koyama, H., Inutsuka, S., 2002, ApJL, 564, 97

[27] Kudo N., Torii, K., Machida, M., et al., 2011, PASJ, 63, 171

[28] Kudoh Y. 2017, PhD Thesis "Magneto Cosmic-Ray Instability in Weakly Magnetized Galactic Disk"

[29] Kuperus, M., Raadu, M. A., 1974, A&A, 31, 189

[30] LaRosa, T. N., Kassim, Namir E., Lazio, T. Joseph W., Hyman, S. D., 2000, AJ, 119, 207

[31] Machida, M. N., Kokubo, E., Inutsuka, S., Matsumoto, T., 2008, ApJ, 685, 1220

[32] Machida, M., Matsumoto, R., Nozawak, S. et al., 2009, PASJ, 61, 411

[33] Machida, M., Nakamura, K. E., Kudoh, T. et al., 2013, ApJ, 764, 81

[34] Masuda, S., Kosugi, T., Hara, H. et al., 1995, PASJ, 47, 677

[35] Matsumoto, R., Hanawa, T., Shibata, K., Horiuchi, T., 1990, ApJ, 356, 259

[36] Matsumoto, R., Horiuchi, T., Shibata, K., Hanawa, T., 1988, PASJ, 40, 171

[37] Matsumoto, Y., Asahina, Y., Kudoh, Y. et al., 2016, arXiv:1611.01775

[38] Miyoshi, T., Kusano, K., 2005, JCoPh, 208, 315

[39] Molinari, S., Bally, J., Noriega-Crespo, A. et al., 2011, ApJL, 735, 33

[40] Morris, M., Serabyn, E. 1996, ARA&A, 34, 645

[41] Morris, M., 2006, Sci, 314, 70

[42] Mouschovias, Telemachos Ch., Kunz, Matthew W., Christie, Duncan A., 2009, MNRAS, 397, 14

[43] Nishikori, H., Machida, M., Matsumoto, R., 2006, ApJ, 641, 862

[44] Parker, E. N., 1953, ApJ, 117, 431

[45] Parker, E. N., 1966, ApJ, 145, 811

[46] Parker, E. N., 1966, ApJ, 162, 665

[47] Peng, C.-H., Matsumoto, R., 2017, ApJ, 836, 149

[48] Riquelme, D., Bronfman, L., Mauersberger, R. et al., 2010, A&A, 523, 45

[49] Riquelme, D., Amo-Baladron, A., Martin-Pintado, J. et al., 2017, A&A (Accepted)

[50] Schmieder, B., Chandra, R., Berlicki, A., Mein, P., 2010, A&A, 514, 68

[51] Schödel, R., Ott, T., Genzel, R. et al., 2002, Nature, 419, 694

[52] Shibata, K., Masuda, S., Shimojo, M., Hara, H., Yokoyama, T., Tsuneta, S., Kosugi, T., Ogawara, Y. 1995, ApJL, 451, 83

[53] Shibata, K., Matsumoto, R., 1991, Nature, 353, 633

[54] Sofue, Y., Nakanishi, H., 2016, PASJ, 68, 63

[55] Suresh, A., Huynh, H. T., 1997, JCoPh, 136, 83

[56] Suzuki, T. K., Fukui, Y., Torii, K. et al., 2015, MNRAS, 454, 3049

[57] Takahashi, K., Nozawa, S., Matsumoto, R., et al., 2009, PASJ, 61, 957

[58] Torii, K., Fujishita, M., Kudo, N., Fukui Y., 2007, The Astronomical Herald, 100, 11, 581

[59] Torii, K., Kudo, N., Fujishita, M. et al., 2010a, PASJ, 62, 675

[60] Torii, K., Kudo, N., Fujishita, M. et al., 2010b, PASJ, 62, 1307

[61] Tsuneta, S., Hara, H., Shimizu, T. et al., 1992, PASJ, 44, 63

[62] Uehara, K., Tsuboi, M., Kitamura, Y., 2017, IAUS, 322,162

[63] van Ballegooijen, A. A., Martens, P. C. H., 1989, ApJ, 343, 971

[64] van Leer, B., 1979, JCoPh, 32, 101

[65] Wolfire, M. G., Hollenbach, D., McKee, C. F., Tielens, A. G. G. M., Bakes, E. L. O., 1995, ApJ, 443, 152

[66] Wolfire, M. G., McKee, C. F., Hollenbach, D., Tielens, A. G. G. M., 2003, ApJ, 587, 278

[67] Xia, C., Chen, P. F., Keppens, R., 2012, ApJL, 748, 26

[68] Xia, C., Keppens, R., Antolin, P., Porth, O., 2014, ApJL, 792, 38